Master's thesis

NTNU
Norwegian University of Science and Technology
Faculty of Natural Sciences
Department of Materials Science and Engineering

Ulrik Ofstad Skjevik

Thermal Decomposition Magnetic Nanoparticles for Improvement of Selective Hyperthermia in Cancer Cells

Master's thesis in MSCHEM
Supervisor: Julian Walker & Sulalit Bandyopadhyay
Co-supervisor: Nesrine Bali
August 2023

NTNU
Norwegian University of Science and Technology

Ulrik Ofstad Skjevik

Thermal Decomposition Magnetic Nanoparticles for Improvement of Selective Hyperthermia in Cancer Cells

Master's thesis in MSCHEM
Supervisor: Julian Walker & Sulalit Bandyopadhyay
Co-supervisor: Nesrine Bali
August 2023

Norwegian University of Science and Technology
Faculty of Natural Sciences
Department of Materials Science and Engineering

NTNU
Norwegian University of
Science and Technology

Abstract

Cancer is one of the leading causes of death in society today and as a result, cancer treatment is a large field for research. Many current cancer treatments attack cancer cells but are also harmful to healthy cells in the body. Therefore, there is a great desire to develop treatments that can be administered locally at the site of the cancer and minimize negative effects on the surrounding healthy cells. Superparamagnetic iron oxide nanoparticles, which generate heat when exposed to alternating magnetic field, are being explored as an option for local cancer treatments. The heat generated by the nanoparticles can be used to activate local drug release, or to produce local temperature changes resulting in local hyperthermia. Polymeric coatings around the nanoparticles are also necessary to enhance biocompatibility and act as a drug carrier. This work focused on optimizing synthesis of iron oxide nanoparticles with polymeric polydopamine and poly-lactic-co-glycoic acid coatings. The aim was to develop methods to optimize size and maximize magnetic properties of the nanoparticles. The next aim was coating the particles to optimize sizes, enhance the biocompatibility and minimize the magnetic loss of the particles.

First the method of separating nanoparticles from the solutions in which they are grown or dispersed can significantly impact their magnetic properties. Thus, magnetic separation and centrifugation were compared. The washing volume of ethyl acetate was also varied to observe possible trends within the particles. Next the synthesis parameters, mass of iron precursor iron acetyl acetonate, volume of stabilizer triethylene glycol and anti-solvent volume were varied between different batches of spherical particles where the effects on particle size and magnetic properties were studied. In order to increase the magnitude of the magnetic response, the effect of particle morphology through single nanospheres versus clusters of nanospheres in terms of saturation magnetization, size and specific absorption rate was studied. Finally clusters of nanoparticles were coated with polydopamine and PLGA, and the thickness of the coatings in terms of particle size and magnetic loss was studied. No significant trend was observed in particle size or magnetic properties as a function of separation method and washing volumes. When moving on to the synthesis parameter variations it was observed little to no trend. Sizes of particles ranged from 5-14 nm. The particles saturation magnetization ranged from 45-54 emu/g with no apparent trend within the particles compared to sizes, although batches with highest ratios between added iron precursor and reaction solvent seemed to possess higher saturation magnetization based on size, but more batches needs to be researched to compare. It was also observed that nanospheres possessed specific absorption rate of 0-80 W/g. Compared to the nanospheres, the clusters displayed sizes of 12-26 nm with a significantly higher saturation magnetization of 72 emu/g. The clustersalso had a significantly higher specific absorption rate at 303 W/g. These properties could also be possessed by spheres if nanospheres were at the same size, but more work will need to be done to prove it. It was found that polydopamine coating thickness could be controlled and that it was grown on the clusters changing the hydrodynamic size from 120 to 768 nm over 24 hours which indicated an hourly growth of 27 nm. The PLGA coating proved to work and gave particle sizes of 300-900 nm. The magnetic loss due to coating was found to be 54.5%, but the final coated particle still possessed a higher saturation magnetization than bare nanospheres with a specific absorption rate of 165 W/g. Lastly the drug was introduced and interacted in a way that seemed like adsorption on the particles.

Contents

1 Introduction

1.1 Motivation

Cancer is one of the diseases in the world with the highest mortality rate. World Health Organisation (WHO) reports that almost 10 million deaths were caused by cancer throughout 2020. From these, the highest mortality rate was in lung cancer [1]. The most common type of cancer was found to be breast cancer [1]. Based on data calculated from 2015-2017, it will affect approximately 39.5% of men and women throughout their life [2]. To reduce these numbers one must focus on the prevention, treatment and the proper diagnostics of cancer and then implement the countermeasures into our society. The common risk of getting the disease in one form or another is also why cancer research is one of the biggest current research areas inside the biomedical field.

Advanced research is already being conducted on how to prevent cancer or how to reduce the risk of getting it. The information on a typical surface level today is that promoting healthier nutrition, increasing physical activity levels and quitting bad habits like drinking and smoking will reduce the risk of getting cancer [3]. If cancer already has occurred despite being healthy and making healthy life choices, one must undergo a specific treatment of the cancer. There are several drugs and gene therapy methods for treating cancer today. Several alpha and beta radiation using different isotopes have been introduced for different kinds of cancers. The part which has proven difficult is to get especially biological drugs to target a specific area and avoid collateral damage from radiation, which is very important when it comes to curing cancer properly. Other proved challenges of cancer treatment are physico-chemical challenges like drug release kinetics and biological barriers [4].

This thesis will focus mostly on how to target cancer using magnetic nanoparticles which can induce local hyperthermia. since cancer-cells have less heat tolerance than healthy cells they will deteriorate faster [5]. The goal is to make superparamagnetic iron oxide nano particles and apply an alternating magnetic field(AMF) at a specific area where the cancer is located. The particles will respond to the magnetic field and create heat which can terminate the cancer cells while reducing or removing collateral damage [6]. Different morphologies and sizes as well as monodispersity of iron oxide nanoparticles have been studied varying different parameters. There have been studies conducted with cubical nanoparticles [7], with different nanoclusters and with spherical particles. Needless to say, all the different sizes and morphologies have had their benefits as well as challenges. Challenges including satisfactory magnetic properties, sizes and bio-compatibility are common problems met in the literature.

For this thesis, the goal will be to optimize the iron oxide nanoparticles for the application of hyperthermia and potentially drug delivery. The particles will be coated with a certain coating to try to keep the treatment as biocompatible as possible and still maintain most of their magnetic properties. The particles will then be attempted drug-loaded to see if they can carry a drug. In this case the tested drug would have to be anti-carcinogenic. A typical drug used for treating cancer is salisylic acid, which possesses anti-carcinogenic properties against melanoma. This was presented in a study by Ausina. P et al. [8]. The goal of the work in the thesis is therefore to engineer particles that would finally be

applicable *in vivo* to terminate cancer cells with minimal collateral damage.

1.1.1 Aims and objectives

The first objective of the thesis work is to engineer a particle with sufficient magnetic properties to be applied inside hyperthermia and drug delivery. The next objective will be to coat said particle with a polymer that can help improve both selectivity and biocompatibility for the hyperthermia and drug delivery. The last objective is to analyze and compare magnetic properties pre- and post-coating as well as attempting to load a drug for the particles applicability inside drug delivery.

1.2 Outline of the thesis

The thesis consists of 7 chapters including the introduction. These 6 chapters are divided into an introduction , a theory part, a literature review, materials and methods, results and discussion, conclusion and an appendix. The introduction will introduce what the thesis will contain and the motivation for the research that is being done. The theory is there for readers to understand the fundamentals of how particles can be made, how they can be modified, different properties possessed by different particles and why they can become applicable inside their area of application. The literature review will give a wider understanding of what has been done until now in this area of research. The literature review will also show the recent work that has been done and where the starting points of the thesis will be. The results will show the data which has been obtained by characterizing the engineered particles. It will give an overview of the properties of the particles and a detailed explanation on how the data can be interpreted, discussions on why the data is how it is. The results will also be mirrored back to the literature review and theory to show that the data can be compared and that the methods followed have worked. The final remarks chapter will give a thorough conclusion of the results and asses the applicability of the final particle. It will also suggest some further research and optimization work to reach the goal of the final engineered particle. The appendix will finally present some experiments done with the wrong chemicals and some other possible synthesis parameters to be used on the particles.

2 Theory

To acquire the iron oxide nanoparticles, one must understand the fundamentals of creating a nanoparticle and how to modify their chemical and physical properties. For the particles to become applicable towards hyperthermia and drug delivery, they should have a certain size and extent of magnetic properties.

2.1 Crystallization theory

Nucleation and growth are the two main processes when synthesizing nanoparticles. Before the particles can grow, they have to nucleate. Supersaturation which is the difference between the activity and the critical activity of a media [9]. To understand how both processes are connected, one should have a look at the respective processes in depth.

2.1.1 Nucleation

Nucleation is the principle of forming new nuclei that can grow into nanoparticles through sufficient supersaturation. For nuclei to be formed there must be a driving force. This driving force is based on chemical potential. When crystallization occurs in solution the basic principle is that the driving force is the difference between chemical potential in the solution and of the nucleating spheres [9]. This is displayed by this equation:

$$\Delta\mu = \mu_1 - \mu_2 \tag{2.1}$$

where μ_1 is the chemical activity of nucleation and μ_2 is the activity of the solution. Chemical potential can be derived from standard potential and chemical activity by implementing the specific activity of one of the two phases in the nucleation process. The chemical activity for one specific phase will therefore be:

$$\mu = \mu_0 + RTln(a) \tag{2.2}$$

where T is the temperature, R is the gas constant μ_0 is the standard potential and a is the concentration (C) times the the activity coefficient γ. Knowing now that the respective phase chemical potential is written as μ_1 one can combine formula 2.1 and 2.2 to create the final chemical potential difference $\Delta\mu$ in detail to describe the total chemical potential difference. The final equation for the crystallization driving force formula will therefore be:

$$\mu = RTln(\frac{a}{a*}) \tag{2.3}$$

Through this formula one can derive the supersaturation which is based on the activity difference of the solute in an arbitrary state and the equilibrium activity of the same solute [9]. The activities as mentioned is based on concentration and the activity coefficient. Finally the Supersaturation for solution crystallization is defined as:

$$S = \frac{a}{a*} = \frac{(C\gamma)}{(C\gamma)*} \tag{2.4}$$

Primary and secondary nucleation are the two standard types of nucleation in classical nucleation theory[10]. The difference between these two is that primary nucleation occurs from a singular phase as it grows from for instance gas or liquids, while secondary nucleation occurs and grows from an already existing crystal[11]. Primary nucleation has two subcategories called homogenous and heterogenous nucleation. Homogenous nucleation requires a higher starting energy than heterogenous nucleation. Homogenous nucleation occurs in a lone phase, while heterogenous nucleation occurs at a surface. These two types of nucleation can be separated by a common formula, however one must first see the energy barrier required for stable nuclei to be formed in homogenous nucleation from primary nucleation. The first factor to look at is the total free energy which is stated as:

$$\Delta G = 4\pi r^2 \Gamma + \frac{4}{3}\pi r^3 \Delta G_v \tag{2.5}$$

Where Γ is the surface energy and ΔG_v is the crystal free energy. The critical free radius r^* required for a nuclei to form in homogenous nucleation without being redissolved is also dependant of the ΔG Gibbs free energy[12]. The critical radius and the free energy are both dependant on the crystal free energy ΔG_v[12]. The crystal free energy is defined as:

$$\Delta G_v = \frac{-k_B T ln(S)}{v} \tag{2.6}$$

where k_B is the Boltzmann constant, T is the temperature, v is the molar volume and S is the supersaturation. After the crystal free energy is determined, the Gibbs total free energy as well as the critical radius can now be determined knowing the surface energy of the particle. Because the formation of nuclei depends on a the critical radius as well one must redefine the total free Gibbs energy into a formula which is fit for the critical Gibbs free energy. First one can have a look at how the critical radius is derived which is as follows[12]:

$$r^* = \frac{-2\gamma}{\Delta G_v} = \frac{2\gamma v}{k_B T ln(S)} \tag{2.7}$$

When knowing how to define the critical radius it can be input into equation 2.5. The equation is then differentiated to find the critical free energy $\Delta G*$. This equation depends purely on the critical radius as well as the general formula of the volume of a sphere. The equation for determining the critical Gibbs free energy in homogenous nucleation is therefore[12]:

$$\Delta G^* = \frac{4}{3}\pi\gamma(r^*)^2 = \Delta G^*(hom) \tag{2.8}$$

For heterogenous nucleation it is a bit different as it requires a factor dependant of a contact angle θ. This factor is stated as ϕ and is the only difference between homogenous and heterogenous nucleation based on critical Gibbs free energy. The relation between homogenous and heterogenous nucleation can be written like this[13]:

$$\phi \Delta G^*(hom) = \Delta G^*(het) \tag{2.9}$$

where:

$$\phi = \frac{(2 + cos\theta)(1 - cos\theta)^2}{4} \tag{2.10}$$

The relation between the two modes of primary nucleation is displayed in the figure below proving that heterogenous nucleation requires less energy to occur than homogenous nucleation. This can also be seen looking at equation 2.9. To visualize this theory one can have a look at figure 2.1 to show the difference in energy between the nucleation modes in primary nucleation.

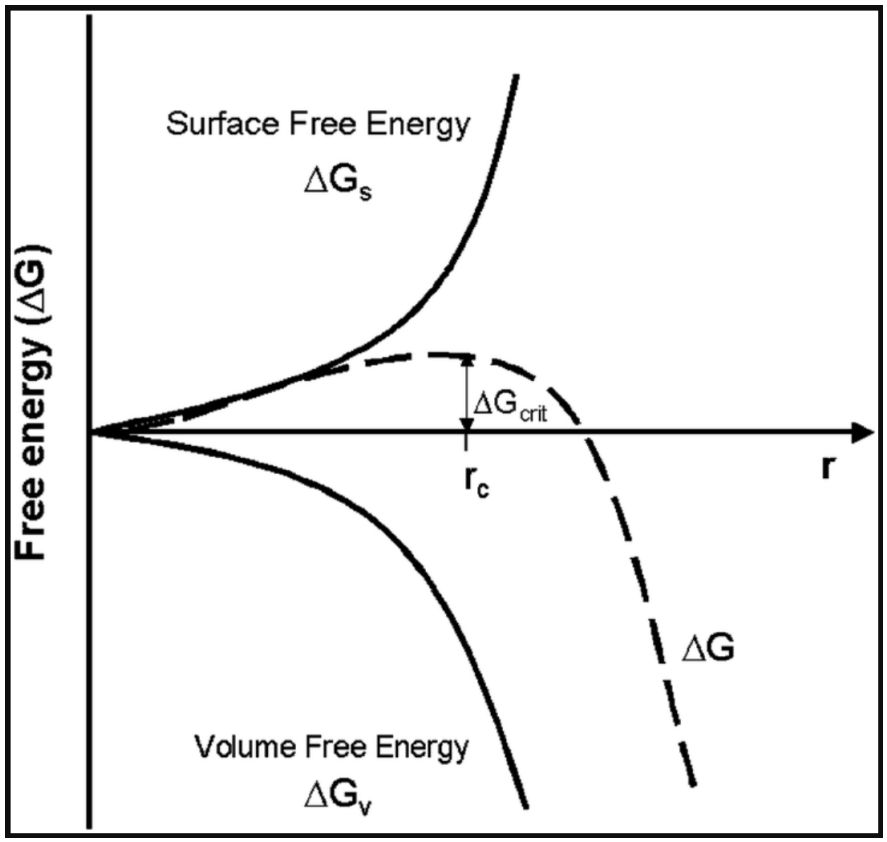

Figure 2.1: Classical nucleation theory principles relying on the relation between Gibbs surface and volume free as well as the critical free energy and critical radius of nuclei made by Ren-Bin Zhou et al.[14].

Unlike primary nucleation, secondary nucleation is the growth of crystals by already exisiting crystals in the solution. The nucleation occurs from interactions between particles

in the solute or within the existing particle[15]. This will not be informed in depth as it is not as relevant as the primary nucleation in this thesis.

To see how fast nucleation occurs one can look into the kinetics of the nucleation. The rate of nucleation is based on the critical Gibbs free energy and temperature. The rate of nucleation is given as[9]:

$$J = A^{(-\frac{\Delta G^*}{k_B T})} \tag{2.11}$$

Where A is a pre-exponential factor, T is temperature, ΔG^* is the critical Gibbs free energy and k_B is the Boltzmann constant. Before nucleation occurs, an interesting factor known as induction time can be observed. This is the time it takes for the first nuclei to form. Equation 2.12 shows the time for the first stable nuclei to form[9]:

$$t_{ind} = \frac{N}{JV} \tag{2.12}$$

From the former nucleation theory, one can understand how it is possible to manipulate the particle properties. The first thing to look at is the main driving factor of nucleation which relies on the supersaturation. The supersaturation is derived from chemical activity between solution and the solid nuclei formed. What can be observed is that by applying higher temperatures and minimizing the critical Gibbs free energy, the more rapid the nucleation rate becomes and the faster the nuclei are formed. The critical radius size and critical Gibbs free energy are decreased by introducing a higher degree of supersaturation. This is observed in the equations by introducing a need for smaller critical radius size of the nuclei to form. It is also shown in the critical Gibbs free energy by the energy decrease by the supersaturation increase. The particle sizes will hence decrease with higher degree of supersaturation as the critical nuclei size decreases. Due to smaller sizes, the particle size distribution will prove to be monodisperse. When nucleating iron oxide nanoparticles, it is therefore important to understand that parameters like temperature, ionic strength and concentration of for instance an iron precursor is important to engineer the particle into satisfactory particles. The next step of the particle is the growth from nuclei into the desired size and/or morphology which is important for the iron oxide as it should posses magnetic properties.

2.1.2 Growth

After the nuclei is formed in the synthesis they will start to enlarge in size as shown in figure 2.2. The figure also describes some of the factors that must be respectively satisfied for the desired growth.

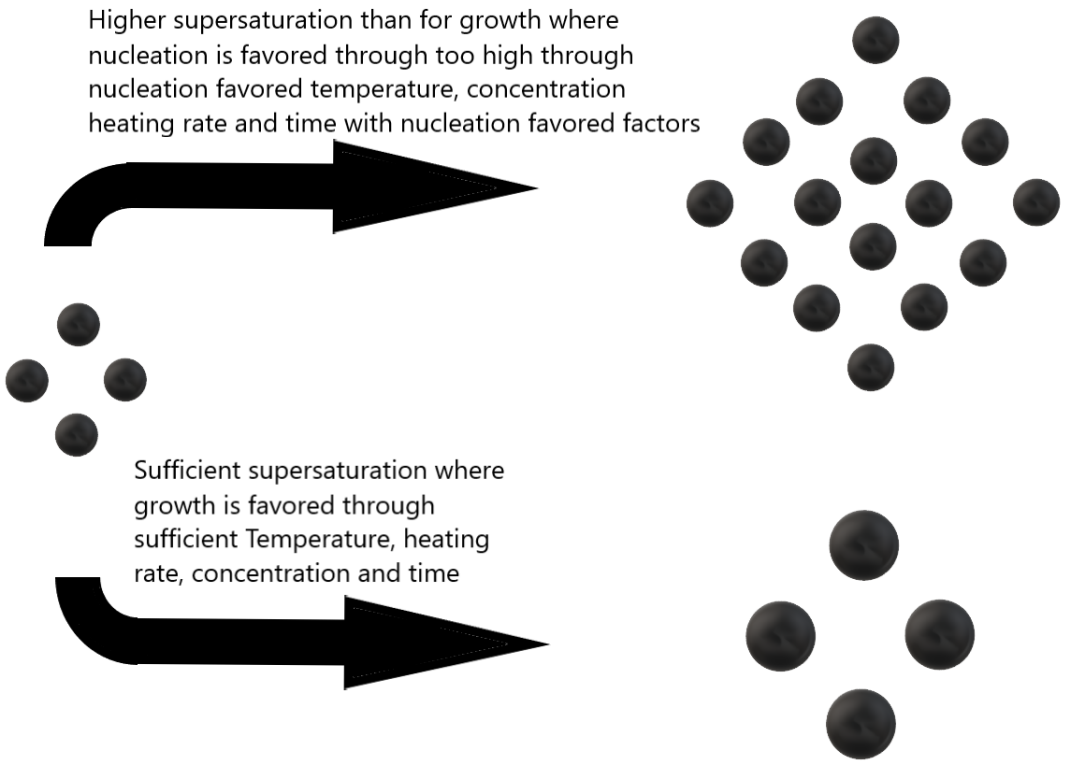

Figure 2.2: A schematic showing factors determining if particles grow or continue to favor nucleation.

The growth of particles is directly connected to degree of supersaturation and a growth constant k_g. There are different types of growth that might occur for different particles depending on the degree of supersaturation. some factors that will induce differences in growth of the particles are internal and external factors. These can for instance be the crystals own intrinsic growth abilities from its desired faceted structure and anisotropic bonding or it can be external factors like supersaturation and temperature[9]. The apparent growth order g determines which growth the particles are going through and is dependant on the supersaturation value. The three growth modes of the particles are diffusion limited growth, spiral growth and surface limited growth in an increasing matter of apparent growth order[9]. Diffusion limited growth occurs when the supersaturation is very high, so the growth of the particles is diffusion based, while surface limited growth occurs with lower degree of supersaturation. The growth rate equation based on supersaturation and kinetics is given as:

$$G = k_g(S-1)^g \tag{2.13}$$

Where k_g is the growth rate constant, S is supersaturation and g is the apparent growth order. If the growth rate is measured one can now find out the growth order from this

equation. This growth rate equation is more specific for crystals grown with more complex structures. For spheres which is more relevant in this thesis, the growth rate can be found looking at the difference in dimension L over time[9].The equation then becomes:

$$G = \frac{dL}{dt} \tag{2.14}$$

This equation shows that the difference in L dimension over time displays the growth rate of spherical particles. An important thing to notice is that in general for nanoparticles there are some mechanisms that might occur under growth of the particles. This can for instance be Ostwald ripening which is the growth of one bigger particle at the expense of a smaller particle in for instance droplets, but also in solids when sufficient surface energy is present[13]. Other mechanisms like sintering might occur when the particles are at high temperatures and is basically the fusion of two or more particles into one big particle. Both of these mechanisms occur due to big surface energies in nanoparticles. A particle in general will always try to stay at the least reuired energy state. In faceted crystals this is called the Wulff construction and is the equilibrium state of a crystal which minimizes the surface energy in faceted crystals[13]. In terms of equilibrium shape, the morphology with least surface area is the sphere and this is the reason why non-faceted particles tend to become spheres when they reach their equilibrium shape.

Another factor that may impact the growth of the nanoparticles is a capping agent. A capping agent‘s objective can be to limit the growth of the particles or help them agglomerate by interacting with the surface charge of the particle. They can also reduce aggregation and stabilize the interface of the particle to reduce or avoid reaction with the mediums the particles are grown in[16]. Capping agents can be for instance citric acid, polysaccharides and polymers to make sure the particles do not grow out of dimension or to control the aspect ratio of the growth. In some cases the capping agent can act both as a stabilizing ligand and a growth-limiting agent. A typical capping agent like this is CTAB in the synthesis of gold nanoparticles[9] that also works as a reducing agent. Capping agents can also contribute to controlling well grown faceted crystals. The function of a capping agent can be visualized in figure 2.3 explaining its function for nanoparticles.

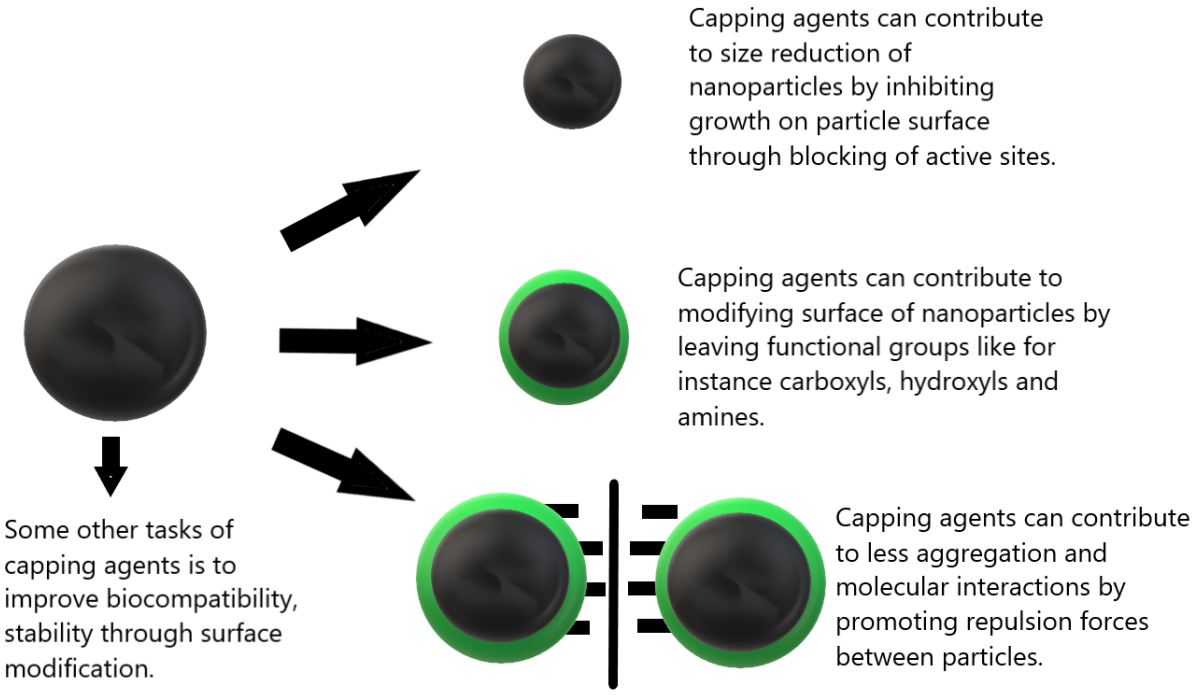

Figure 2.3: Different properties of a capping agent when used in a nanoparticle synthesis.

After looking at how the particles growth can be modified, one can look at the morphology of the particles which becomes very important in the application field of the synthesized particles in the end. For biomedical application it is very important that the shape of the particles are well suited for it‘s purpose. It is proven that even faceted crystals can turn into certain crystals known as Hopper crystals. This is through dendritical growth of the faceted crystals. This process happens with higher supersaturation. However, if the supersaturation is further increased the so-called spherulitical growth occurs which turns the well faceted crystal into a polycrystalline nearly spherical particle[9]. The difference between a well faceted crystal and a dendritical and/or a spherulitical particle is that the growth mode of a well-faceted crystal is considered as smooth grown compared to the polycrystalline particles in which follow a rough growth with higher driving force through higher supersaturation.

This information is critical when proving that supersaturation at higher levels in general end up turning the particle into its least energy surfaced shape, the sphere. Another important detail is the cooling rate which also determines the morphology of the particle. Through rapid cooling there might be more interparticle interractions which may cause the particles to aggregate and have non-uniform morphologies. If the cooling is done slower however, the particles may become well-faceted or less aggreagated. In short the rapidly cooled particles become more amorphous while the slow cooled ones become more crystalline[17].

From this growth theory one can now understand how the particles will grow. It is proven that by introducing a higher degree of supersaturation, the particle will always try to reach its minimal surface energy. When having a rapid growth one would also typically expect

less monodisperse particles as the supersaturation does not grow uniformly. This will result in a wider particle size distribution. This will be relevant when producing the iron oxide as the particles growth will be determined by both the faceted desired structure of the particle, the supersaturation and the temperature. It can also be interesting to see if the solution media will act as a certain type of capping agent. There are several factors that will impact the growth mode and supersaturation when the particles are growing. In terms of iron oxide nanoparticles it is however important that the particles lie within 3-50 nanometers to get the desired properties from the particles.

2.1.3 The correlation between nucleation and growth

The nucleation and growth will now be put together to show how they impact each other and why it is important towards different particle properties that the particles are made with a set of parameters.

When given sufficient supersaturation, activity in solution start to nucleate and grow depending on the degree of supersaturation. To easier understand this a graph of La Mer and Dinegar has been shown to display the relation between the nucleation and growth depending on supersaturation vs time. A graph like this was displayed in a study by Bahrig. L et al.[18] and is shown in figure 2.4.

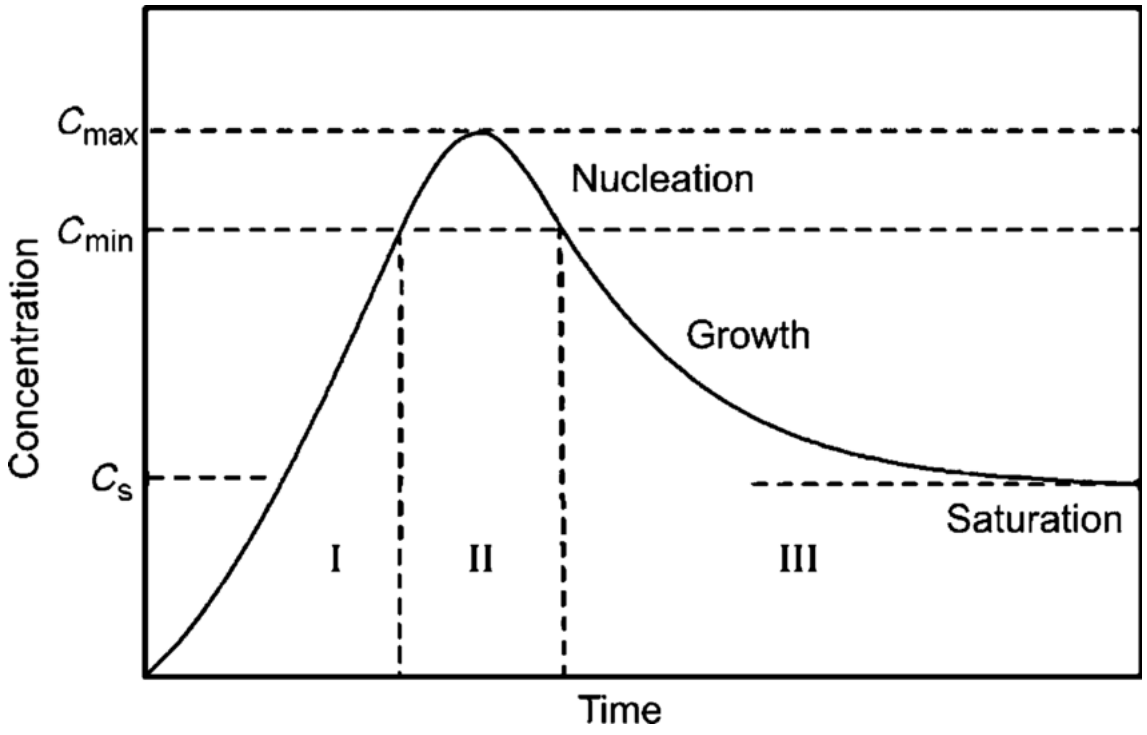

Figure 2.4: Relation between nucleation and growth in different concentrations which correlates to the degree of supersaturation shown by La Mer and Dinegar[18].

Figure 2.4 shows that when applying a high degree of supersaturation, particles will start to nucleate. When keeping the supersaturation at this level, the crystals will prefer to nucleate over growing. If the degree of supersaturation is decreased, the crystals will prefer to start their growth instead of continuing to nucleate. The downwards growth

curve is shown in step three of the figure.

The nucleation and growth has now theoretically been proven to have a big impact on the final particle. From the stage of nucleation to grown particles there are several factors impacting the properties from nuclei to particle. The first important part is the chemical activity coefficient which gives rise to the supersaturation principle. From interfacial energy, Temperature and supersaturation one can manipulate the critical nuclei radius r^* by reducing or increasing the critical Gibbs free energy ΔG^*. The nuclei sizes can then be formed at smaller sizes by introducing a higher degree of supersaturation or increasing temperature. These two factors do also control the rate of nucleation which also decreases by minimizing ΔG^*. When starting with smaller nuclei, their surface area is bigger and hence it is harder to control their sizes during growth. When starting with bigger nuclei, the size may be easier to control. It might however be harder to control their aspect ratio and morphology during the growth stage as they are harder to manipulate due to their lesser surface energy. It is also known that when introducing higher temperature and supersaturation in the growth stage it will promote rough growth which gives rise to the uncontrollable growth. The particles are therefore possible to control to some extent when it comes to the particle size distribution and their sizes, but there are limitations for both smaller and bigger nuclei from the starting point of formed nuclei. Nucleation and growth are dependant of each other when reaching the final particle and it is therefore important to try to control these processes as best as possible.

2.2 Iron oxide nanoparticles and their magnetic properties

The iron oxide nanoparticle is a particle consisting of many different phases which has the chemical formula Fe_3O_4. This thesis will present mostly the morphology known as magnetite. The reason why these particles are so relevant in terms of biomedical applications is that they have the property better known as superparamagnetism. Superparamagnetism is a phenomenon in ferrimagnetic and ferromagnetic particles that depends on the Neel relaxation rate. Particles can flip their magnetic direction when being in nanoscale[19]. The Neel relaxation time is the time between the magnetic direction flips of the particles in the nanoscale. Superparamagnetism occurs when the time used to measure the particle‘s magnetic properties without a magnetic field surpasses the Neel relaxation time in smaller single domain particles that are 3-50 nm[19]. The reason however that the magnetite particles are superparamagnetic is that when applying a magnetic field, one can return the magnetic abilities of the particles[19]. The reason superparamagnetic particles are different from paramagnetic ones, is that they are more susceptible towards a magnet than the paramagnetic particles[20]. The superparamagnetic principle is displayed in figure 2.5.

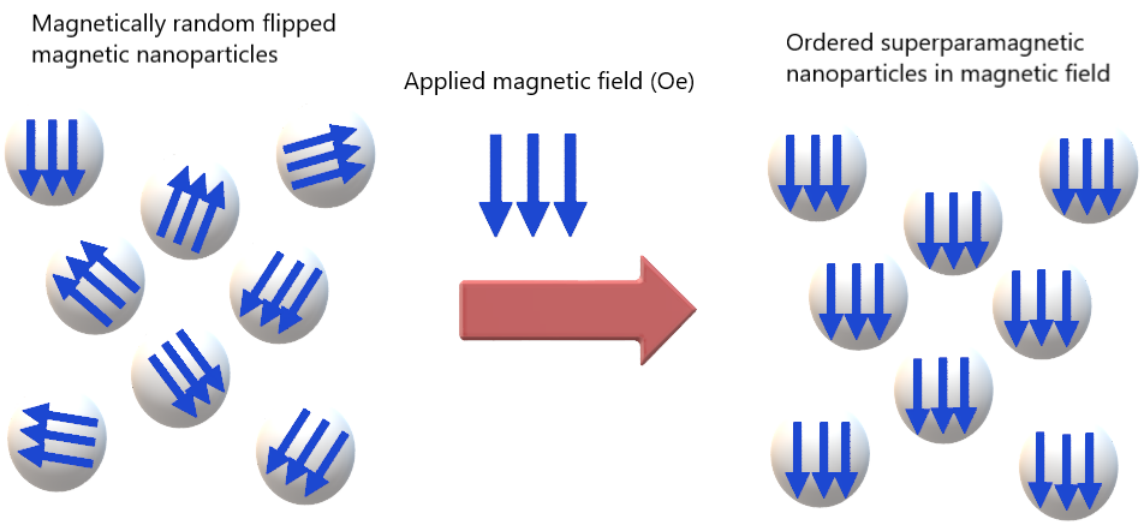

Figure 2.5: Magnetic allignment of superparamagnetic nanoparticles by applying a magnetic field.

Figure 2.5 shows how particles are arranged at random until a magnetic field is approaching them. The particles are then turning towards the magnet with a higher magnetic susceptibility than paramagnetic particles. This is also the reason the IONPs are used in biomedical application as one can control when the particles will remain inert and when they will display magnetic properites. This effect will also come in very handy when working with the objective of this thesis which is the improvement of hyperthermia.

The magnetic properties of Magnetite specifically are also size and phase dependant, Maghemite posses less magnetic strength than magnetite and is therefore also less desirable[21]. The size of the particles also matters, as bigger particles are usually more magnetic than smaller ones. This was shown by Hel. X et al.[22] who saw that magnetic nanoparticles increase their saturation magnetisation and Curie temperature, but decrease coercivity with increase in particle size. The reason for this is that its easier to break down the particles if they are smaller, and heavy metals can pose a threat towards the liver tissue when being broken down. This means that the particles should be in the superparamagnetic range of 3-50 nm. This also makes them more suited for the biomedical applications. They should be big enough to avoid being filtrated before being applied, but also small enough to avoid organ damage and being able to exit the body[23]. These particles can be synthesized by a method called thermal decomposition, where high temperature forms particles from nuclei.

2.3 Thermal decomposition

Thermal decomposition synthesis of iron oxide nanoparticles is based on heating up a solution together with usually a metal precursor salt or solution. The principle of the decomposition itself is that by applying heat the iron precursor will decompose and react with the growth/capping agent to produce particles. What is good with this method is that it is said to produce monodisperse small particles which is necessary in biomedical application[24]. The reason for this is that the temperature is at the degree where spherical particles are formed from nuclei. This is also shown in different iron oxide thermal

decomposition reactions done by Hufschmid. R et al.[25] at 280-320 ℃where the particles also become spherical. This might however not always occur, as some reactions depending on concentration, reaction solvents and ionic strength can create other morphologies like for instance in Maity. D et al.2011[26] where they have produced nanoclusters at nearly the same temperature as used in Hufschmid. R et al.[25] In the different synthesis methods of thermal decomposition, there is usually some sort of surface modifying agent which can be used to stable interactions between particles, as well as a decomposable metal precursor which in this case should lead to magnetic nanoparticles. This makes the particles grow in a more uniform rate and makes sure the particles will remain monodisperse[25]. Another advantage of this synthesis method is that all the particles will not need a phase transfer process, which is a step that may be crucial in determining the particles final properties. To create the most suited particles, there are some parameters that will need optimization. Factors like cordination of ligands, Temperature, pressure and nature of the metallic ion are some of the factors that may impact the property of the thermal decomposition iron oxide particle[27]. Through this thesis the main focus will be on the so-called TREG particles which is a combination of the iron precursor $Fe(acac)_3$ and triethylene glycol.

2.3.1 $(TREG)$triethylene glycol and ($Fe(acac)_3$) iron acetylacetonate as precursor

This synthesis is based on that acetyl acetonate will decompose its organic residues and react with the TREG molecules to form the iron oxide particles. The iron precursor and the TREG are shown in Figure 2.6.

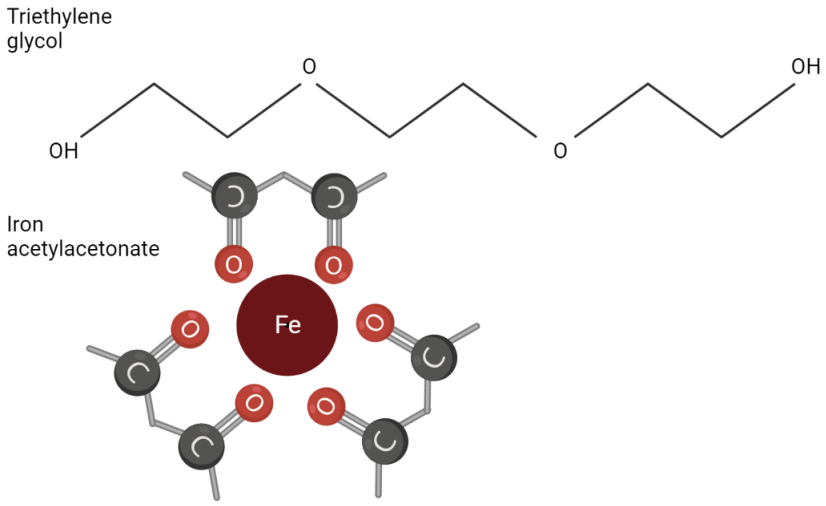

Figure 2.6: Reactants used within the TREG thermal decomposition synthesis method of iron oxide nanoparticles.

Since TREG is one of the reactants in the solution, the particles will be presented as TREG particles as they have the outer surface of a typical TREG branch. A depiction of this can be seen in figure 2.7.

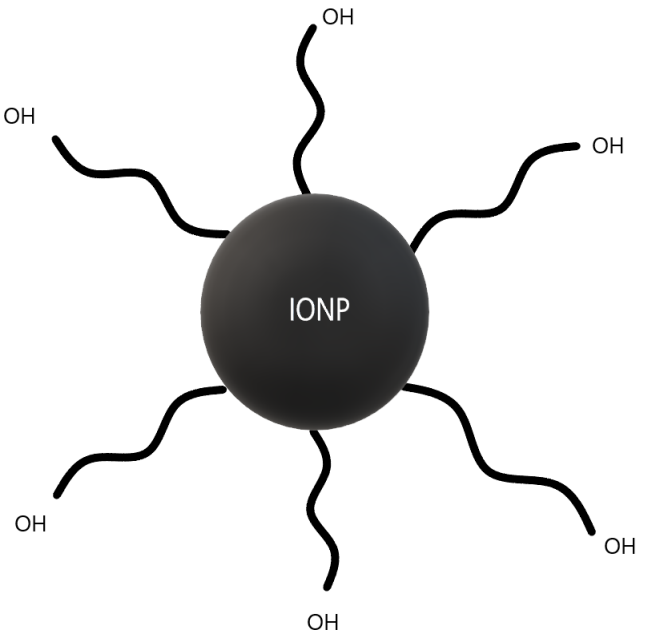

Figure 2.7: The assumed typical iron oxide nanoparticle retrieved from the TREG synthesis.

Figure 2.7 displays briefly out of scale how the IONPs in TREG look like. These are functionalized by hydroxyl groups on the surface, while other synthesis methods may have other surface ligands. One important feature of the TREG synthesis is that one can avoid an extra step towards the final product. This step is the phase transfer. The phase transfer tends to change the sizes of the particles when transferring them from hydrophobic to hydrophillic. Some research also reports different morphologies and stabilization properties after phase transfer[28]. There are other methods in thermal decomposition that needs the phase transfer step. Thermal decomposition methods using iron oleate and iron pentacarbonyl needs this extra phase transfer step to become hydrophillic[29]. Hydrophillic particles are mostly used in biomedical application. The reason why they must be hydrophillic is that the particles will go through the blood flow. Hydrophobic compounds like for instance hexane would be toxic when introducing it through the blood.[30]. Since TREG particles are stored in MQ water and are hydrophillic directly from synthesis, they do not need to be phase transferred, hence less steps and less possibilities of impacting the particles properties through phase transfer[31]. The TREG particles are also known for being small sized (SPIONs) superparamagnetic iron oxide particles which are monodisperse. This makes the TREG particles viable for *in vivo* studies as well as *in vitro*.

2.4 Hyperthermia

Hyperthermia as a medical term is defined as abnormally high body temperature. This problem arises when the body cannot dissipate the heat absorbed and the body temperature increases[32]. Hyperthermia at a certain temperature can start deteriorating cells. This means the principle of hyperthermia can be used in biomedical treatment to for instance kill cancerous cells in the tissue and preventing the cancer to spread. However, when applying this heat to the cells it is very important that the hyperthermia phe-

nomenon happens in a controlled area. The reason for this is that by preventing an open hyperthermia, one can prevent the creation of secondary cancer cells or in general unnecessary surrounding tissue damage. This becomes explicitly fatal if the hyperthermia occurs in essential organs[23]. The highest temperature the healthy cells in the human body can sustain is 40 °C[32]. Superparamagnetic iron oxide nanoparticles(SPIONPs) can induce magnetic hyperthermia effect.

2.4.1 Superparamagnetic properties importance in hyperthermia

The superparamagnetic properties of the iron oxide nanoparticles make it possible to use an AMF to create oscillations within the particles that eventually produce heat. The frequent movements of the IONPs create vibrations and hence energy from friction which turns into heat. This heat can be localized and become potent towards a specific area. In the application of magnetic hyperthermia towards cancer cells the local heat becomes perhaps the most important role due to probability of other damaged tissue, which can lead to for instance permanent organ damage[23]. The way the SPIONPs spin and oscillate is displayed below in figure 2.8.

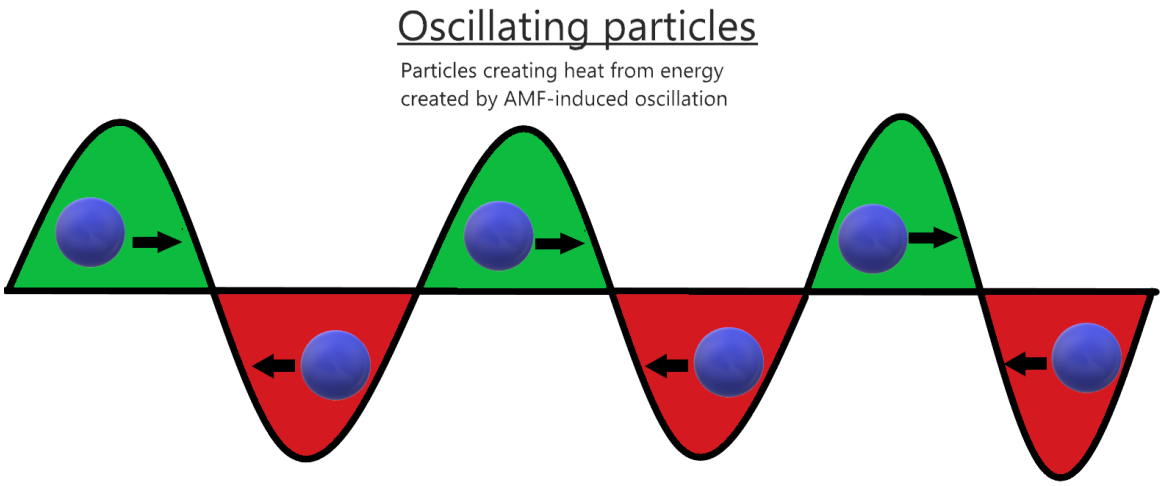

Figure 2.8: Oscillation of iron oxide nanoparticles when applying an alternating magnetic field causing friction that leads to particles heating up.

Figure 2.8 shows how the particles are oscillating back and forth to create energy through friction that turns into heat. The particles are moving in specific frequencies depending on how the AMF is adjusted. This can be controlled by using specific equipment that produces different frequencies through varying the field and resistance in the AMF instrument[33].

2.4.2 Specific absorbtion rate and saturation magnetization

Specific absorption rate known as SAR inside of biomedical application is the energy deposited as heat from an AMF through pulses into body tissue[34]. Higher SAR-values indicate more rapid temperature increase. The energy output is measured in watts per gram. Higher temperature in localized area per time as well as the ability to stop when

pulling away the magnetic field correlates to better control in the hyperthermia application. The equation to measure SAR in magnetic hyperthermia is given in 2.15 as[35]:

$$SAR = C\frac{\Delta T}{\Delta t}\frac{1}{m_{MNPs}} \tag{2.15}$$

where C is the specific heat of the fluid, ΔT is the change in temperature, Δt is the change in time and m_{MNPs} is the mass of the particles measured[36]. This means that the more mass is measured, the higher the temperature needs to go to maintain its SAR value. The heat evolution is directly correlated to the mass of particles[36]. Specific absorption rate may also increase by another factor which is not shown in the equation above. This factor is the magnetic field strength applied in the AMF. When increasing the field strength of the magnetic field, one also increases the oscillation of the magnetic nanoparticles due to higher frequencies of oscillation which creates a more rapid heating and hence a higher energy deposited through heat into tissue[37].

Saturation magnetization M_s is the maximum magnetic moment a material can reach per untit volume before flatting out its potential[38]. Saturation magnetization also has a correlation towards the specific absorption rate. When the saturation increases, the SAR values usually also increase. Saturation magnetization can be found through making a magnetic hysteresis loop. Saturation magnetization from hysteresis loops can be calculated using the following equation 2.16 shown below.

$$M_s = b - \frac{\Delta b}{\Delta h}h \tag{2.16}$$

Where M_s is the saturation magnetization, b is the apparent flux density measured from the B-coil in the instrument which is one of two coils used for the measurement when creating a magnetic hysteresis loop, the $\frac{\Delta b}{\Delta h}$ is the incremental permeability and finally h is the magnetic field measured by the second coil called the H-coil in the instrument. The saturation magnetization is then found at the maximum of what is measured through the B and H-coil and input into the formula[39]. The instrumets creating the hysteresis loops through measuring the magnetic samples are called vibrating sample magnetometers. The magnetic field applied when the sample is vibrating, measures the magnetic properties of the sample and gives the data creating the loop before one then can calculate the total saturation magnetization.

2.4.3 Thermal shock of cells and cell viability

After stating some relevant theory for particle nucleation and growth, some processes and magnetic theory one can now move on to the application of the magnetic particles. To further understand what happens *in vivo* when the application is utilized one must have a look at how the SPIONPs surround the cells and how they terminate them. The principle of magnetic hyperthermia *in vivo* is that the cells in a local area are terminated by the induction of higher temperatures over a short period of time[26]. This is known as a thermal shock and makes the cells deteriorate as the proteins in the cells denatures at a certain temperature. Cancer cells have lower heat toleration than healthy cells which

makes the application a good alternative for cancer cell termination if one can make the process more selective. When the treatment is optimized one can ensure that only cancer cells are terminated in the process, and not damage nearby cells. The process of magnetic hyperthermia is shown in Figure 2.9.

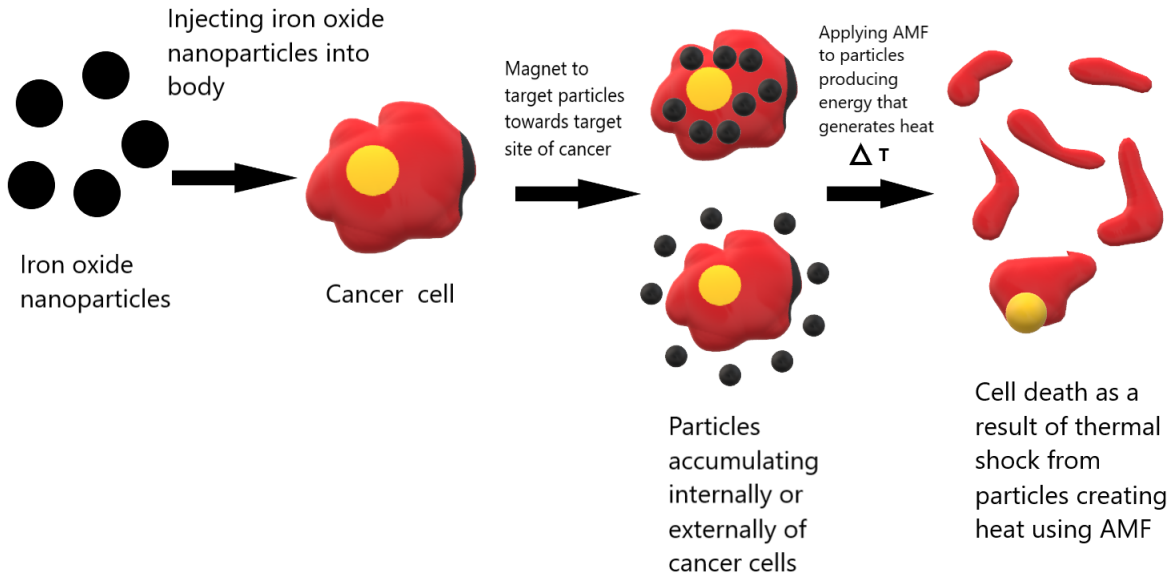

Figure 2.9: General depiction of how a typical targeted *in vivo* Hyperthermia process would be likely occur.

2.5 Coating particles

Particle coating is a process to modify the surface of a particle by introducing new functional groups. These groups can be for instance hydroxyls, amines and carboxyls. Amines and carboxyls are known for increasing biocompatibility and are hence used extensively as surface functionalized groups inside the field of biomedical research [40]. The reason for coating the particles is to improve their biocompatibility and penetration potential through cells. Amines can for instance be more viable to initiate grafting polymerizations [41]. In general the coatings are either organic in terms of polymers or inorganic like for instance gold or other metals that create usually a core-shell structure particle. There are several ways to coat a particle. Varying parameters like temperature, pH or pressure can be used like in Graf. C et al. [42] where they use a higher pH to coat silica with polyvinyl pyrrolidone (PVP), while others can operate through normal conditions as in Mrówczyński. R et al. [43] where they coat polydopamine on top of different metal nanoparticles. The most relevant theory for the coating of particles in this thesis will be the polymeric processes of coating particles.

2.5.1 Polymer chemistry and Polymerization techniques

Polymerization is the chemical process where monomers of the same and/or different structures are put together through different surface interactions. The two main types of polymerization are addition polymerisation and condensation polymerization [44]. Dif-

ferent under-categories of polymerizations are for instance atom transfer radical polymerization (ATRP), reversible addition fragmentation chain transfer (RAFT) radical ring opening polymerization (rROP) among others[45]. Polymerization occurs in different steps. The starting step is the intiation process. It then moves into the propagation process. Some polymerizations also have an elongation process. The third/fourth final step is the termination process[46]. For different kinds of polymerization there are different initiators used in the initiation process. These are usually there to make sure that the polymerization process will start[47]. The focus for this thesis will be mostly in the rROP where one can open ring structures by introducing an initiator for the polymerization of ring structured monomers. An example of a ring opening polymerization is the ring opening polymerization of poly-lactic-co-glycolic acid (PLGA) which will be used in coming experiments. What is importnat to notice is that this is also a polycondensation polymerization. The reason PLGA will be focused is that it can penetrate cells with its ability to stay inert, but also be diffused into cell systems as a drug delivery agent[48]. This keeps the particles safe and inert when travelling to their target destination. A proposed reaction mechanism by Hu. Y et al.[49] of a ring opening poly-condensation polymerization of PLA with the initiator is shown in figure 2.10. PLGA ring-opening would also likely occur the exact same way as the only difference between lactide and glycolide is that lactide is methylated.

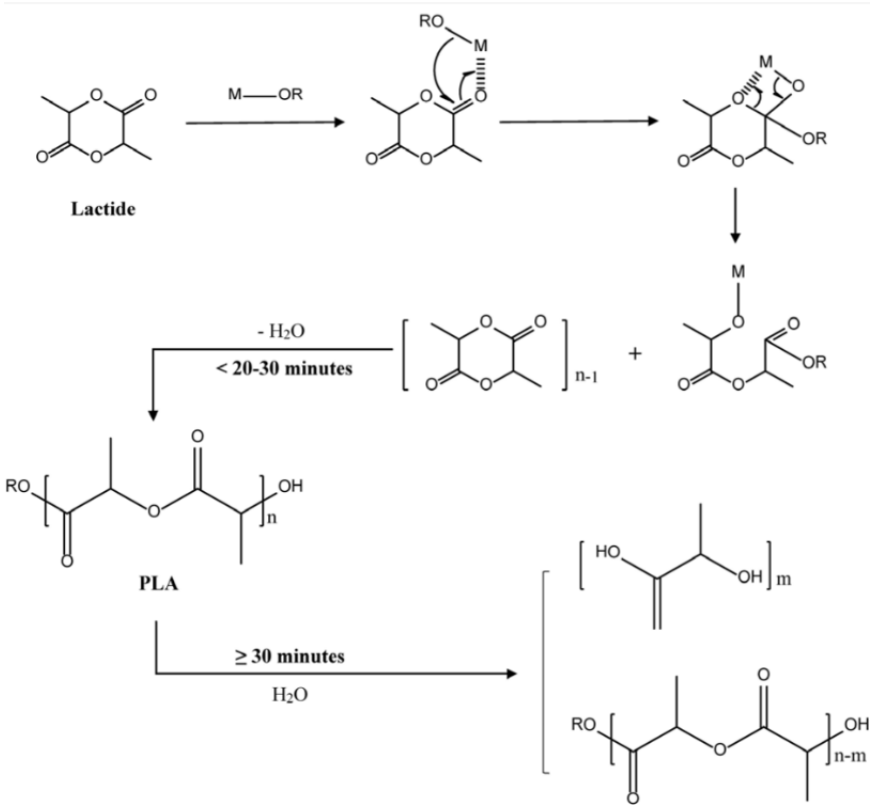

Figure 2.10: Ring opening radical polymerization of PLA proposed by Hu. Y et al.[49] through the use of a metallic initiator, typically stannous octoate ($Sn(Oct)_2$.

Figure 2.10 shows that the initiator interacts with the ring of L-lactide and breaks it up with a nucleophillic attack at a higher temperature which is usually 130-200 °C[49]. The

split ring is then bonded with the initiator after the organic nucleophilic group has stolen a bond from the oxygen. The monomer with the OR group then attacks the next ring and creates an oligomer which is a connection of few monomers[46]. This process continues until the termination process is done and the polymer is formed through polycondensation shown in the picture. In the end, the chains are terminated and the synthesis of PLA is done. The polymer after being synthesized can then for instance be grafted through a surface grafting interaction between the hydroxyl group and another group. This requires that the surface the polymer should be grafted onto is compatible. This means that groups like amines, carboxyls or other hydroxyls must be present to make sure the coating works. This is shown by Lin. L et al.[50] where the oxidative polymerization of polydopamine could occur at a hydroxyl surface.

3 Literature review

3.1 Thermal decomposition

There exists several methods of synthesizing thermal decomposition iron oxide nanoparticles. A study conducted by Hufschmid. R et al.[29] reported synthesis methods using iron pentacarbonyl and iron oleate together with oleic acid to create monodsiperse hydrophobic iron oxide nanoparticles coated with oleic acid. The particle sizes ranged from 5-24 nm. Other iron oxide nanoparticles similar to these were reported in a study by Yu. W et al.[51] who used carboxylate salts together with oleic acid to form monodisperse IONPs in the range of 6-30 nm. The challenges of these synthesized particles is that they would usually require a phase transfer due to their hydrophobic surface. One would usually desire hydrophillic IONPs in the biomedical field. This means that one would typically desire a particle that would not have aliphatic long chains as the oleic acid coated IONPs, but reactive groups like for instance carboxyls, amines or hydroxyls. For these particles, one would need a typical organic iron precursor as before. A decomposable precursor is always needed in the thermal decomposition method where most of these are organic[51] [26] [52] [53].

Maity. D et al.2007[53] did a study where it was attempted to create iron oxide nanoparticles through the use of different polyols. In this case they researched Diethylene glycol (DEG), triethylene glycol (TREG), tetraethylene glycol (TEG) and polyethylene glycol (PEG). It was concluded that the DEG and TREG particles were the most water dispersible in their size range, most monodisperse, least aggregated and had the highest saturation magnetization in smaller size ranges.

3.2 TREG-synthesis of iron oxide nanospheres

After deciding to pursue the most efficient particles from the previous polyol study, the TREG synthesis was pursued to see if one would be able to optimize this synthesis. A method derived from a study done by Maity. D et al. 2009[52] was followed. The study suggested using a synthesis where 2 mmol of iron acetyl acetonate was mixed with TREG and stirred under 120 ℃for 1 hour at 400 rpm. The temperature was then increased to 280 ℃and left stirring for 2 hours. The particles were then left to cool down before they were washed with ethyl acetate, centrifugated, separated and re-dispersed in ethanol multiple times before finally being dispersed in MQ-water. The ratio of EtAc to ethanol was 2:1.

The particles were found to be monodisperse with a size measured in "dry size" to 11 nm in S(T)EM and hydrodynamic size in DLS to 13 nm. The peaks in XRD indicated magnetite/maghemite and the saturation magnetization was found to be 65 emu/g. The zeta potential was found to be +40 mV. Magnetic hyperthermia studies were also done in this research. It was observed that by inducing a magnetic field of 20 MHz at 1 mg/ml and 0.5 mg/ml respectively gave SAR-values of 885 and 539 w/g. To give a proper analysis and possible optimization of the synthesis, this wwas the first article pursued in the thesis work. A paper which was later pursued was another paper by Maity. D et al.2011[26] where they had also researched iron oxide nanoclusters and their possible hyperthermia application.

3.3 TREG/TREA synthesis of iron oxide nanoclusters

It was decided to research more around different morphologies of the iron oxide nanoparticles. Another morphology proven to give high saturation magnetization was therefore pursued as the next step. In the synthesis method by Maity. D et al.2011[26] to produce iron oxide nanoclusters, a combination of triethylene glycol (TREG) and triethanolamine (TREA) as solvents with different ratios dpending on the batch produced ranging from 4:1 TREG to TREA to 1:4 TREG to TREA was used. Pure TREG and TREA was also attempted. The same mass of iron acetylacetonate of 2 mmol or 0.71 g was utilized. The particles were then washed at the same procedure using centrifugation. From this research the focus on the work in the thesis was on the 1:4 TREG:TREA ratio called the MNC-14 clusters, due to them being the particles that formed the most visible clusters.

The saturation magnetization was found to be 75 emu/g. The peaks of the XRD proved again to show peaks of magnetite and maghemite. The hydrodynamic size of the clusters was found to be 187 nm at first and 182 nm after a day. The sizes from S(T)EM were measured to around 44 nm for the MNC-14 clusters. The hyperthermia studies showed SAR-values of 500 at 240 KHz at 89 kA m^{-1}. this method was pursued to see if one would be able to achieve the same efficiency for self-made clusters or even optimize the efficiency for the hyperthermia application.

3.4 Intermediate coating of polydopamine on iron oxide nanospheres

The next goal was to create a higher biocompatibility by coating the particles. In a study done by Mrówczyński. R et al.[43] polydopamine was coated on top of different nano-metal oxides including iron oxide. the study showed that it was possible to control the coating thickness of polydopamine coating to some extent. It was therefore interesting to test if this method would work on the optimized particles. For the coating, they used 10 µM tris buffer and added dopamine hydrochloride before leaving it stirring for 24 hours in open air which created an oxidizing polymerization atmosphere. The resulting particles were washed with methanol, ethyl acetate and (MQ)-water and separated through the use of a magnet. The particles were then dried before characterization.

The FTIR analysis showed a typical fingerprint area of the polydopamine in region 1250-1650 cm^{-1} as well as the iron oxide peak at 500-600 cm^{-1}. In the study they also succeeded coating the polydopamine coated particles with poly-lactic acid (PLA) through the use of Dimethylaminopyridine (DMAP) which is a ring opening initiator.

A study done by Singh. N et al.[54] also reported some data regarding polydopamine coated iron oxide nanoparticles. It was observed that the UV-vis absorption had a higher peak for the polydopamine coated iron oxide nanoparticles than that of the bare ones. It was also conducted a stability test through the measurement of a zeta curve that proved the typical PZC of IONPs would be around pH 8.7 and that the polydopamine coated IONPs would have a PZC in a pH of about 4.7. Due to amines possessing good initiation surface for polymerization, the polydopamine was pursued as an intermediate coating[41].

Cheng. C et al.[55] conducted a study where a polyethersulfone (PES) surface was coated with polydopamine and retracted through different time points of respectively 2 hours, 8 hours and 24 hours with a Phosphate-buffered saline (PBS) buffer at pH 8.5. The PD

coated particles coating thickness on top of the PES surfaces at the different polydopamine coating retraction times was then measured. After 8 hours the coating thickness in FE-SEM was found to be 85 nm. The full coating thickness after 24 hours was found to be 185 nm. It was also found that by using AFM, the sizes were measured differently and the coating from the different retraction times was found to range from 20-500 nm.

A study of PD-thickness was also performed by Lin. L et al.[50] where Carboxyl functionalized iron oxide were coated with polydopamine. The following shell thickness after 4 H of polymerization was 4 nm found by DLS. The retraction time study with polydopamine would therefore be done to see if one could control the thickness of the polydopamine coating and hence retrieve small IONCs coated with polydopamine.

3.5 Coating of PLGA on nitrogen dyes and iron oxide nanoparticles

As polydopamine was supposed to be an intermediate coating used for easier initiation using an amine surface, the next step would be to polymerize PLGA on top of the polydopamine coated particles. A study done by Yousif. M et al.[56] was conducted by coating PLGA on different dyes with amine functionalized surfaces. A solvent free method was utilized where monomer salts were melted at 130 ℃before being introduced to the dyes and initiated with stannous octoate under inert atmosphere of nitrogen. The reaction was then run for 3 hours under nitrogen atmosphere at 130 ℃. The resulting yield was then dissolved in acetone and precipitated out with methanol four times before being set to dry under reduced pressure. The resulting coated dyes were then measured in DLS finding a zeta potential of around (-40) - (-50) mV for the coated dyes. The hydrodynamic sizes of the coated dyes ranged from 98 $\pm$ 5 nm - 120 $\pm$ 2 nm. Due to the study showing satisfactory sizes this method was pursued, to try to create nanosized PLGA coated PDCIONCs (PLGA@PDCIONCs). A study done by Zhang. X et al.[57] presented sizes of PLGA coated iron oxide nanoparticles at 300 nm. A zeta curve of PLGA at magnetite was produced in a study done by Okassa. L et al.[58] where the PZC of PLGA on top of iron oxide nanospheres was found at around pH 3.

3.6 Drug loading of Curcumin in amine-functionalized magnetite nanoparticles

After coating the particles with both polydopamine and PLGA, the particles were attempted loaded with a drug. In a study done by Sundar. S et al.[59] a co-precipitation method was utilized to create iron oxide nanoparticles before coating the particles with silica. The anti-carcinogenic drug curcumin was then attempted loaded into the amine functionalized iron oxide nanoparticles. 10 mg of APTES coated iron oxide nanoparticles was mixed together with 0.1% curcumin dissolved in ethanol before leaving it stirring for 3 hours. The particles were then magnetically separated and washed before being used for drug delivery. A few changes had to be made to load the PLGA@PDCIONCs with a drug. curcumin was therefore swapped with salisylic acid which is a smaller molecule and hence theoretically more easily loaded inside the particles. The salisylic acid was in this case dissolved in water instead of ethanol.

4 Materials and methods

4.1 Materials

4.1.1 Chemicals for Thermal decomposition of iron oxide nanospheres and nanoclusters

For the ironoxide nanospheres and nanoclusters, Triethylene glycol (TREG) 99%, Iron(III) acetyl acetonate($Fe(acac)_3$) 97% and triethanolamine (TREA) 98% and absolute ethanol were purchased from Merck. Ethyl acetate (EtAc) >99.5% was purchased from Merck and Vwr. Local argon gas 99.99% was utilized to keep the reaction atmosphere inert.

4.1.2 Glassware and setups for synthesis of iron oxide nanospheres and clusters

The following parts were utilized in the thermal decomposition method:

- A heating mantle with an in-built stirrer
- A heat controller for controlling the heating rate and temperature of the reaction
- A condenser for water inlet and cooling
- A gas inlet for the argon to enter
- A three-necked flask as a reactor
- A needle to purge the reaction beforehand
- A balloon with Argon gas to make sure the atmosphere stayed inert foe nanospheres
- A recycling water cooler to flow cool water into the condenser
- A lab-jack to more easily remove the three-necked flask from the heating mantle after end of reaction
- A Temperature glass probe for the heat controller to control the heat inside the reaction flask
- Magnet and beakers for the washing steps

4.1.3 Chemicals for Poly-dopamine and PLGA coating on iron oxide nanoclusters

For the poly-dopamine polymerization, Dopamine hydrochloride (BP) ref was bought from Merck. Tris-buffer pH 8.5 was created from tris-salt, MQ-water and modifying the pH using hydrochloric acid. The tris buffer concentration was 10 µM as stated in the study of Mrówczyński. R et al.[43]. For the PLGA coating, the monomers L-glycolide and RON-lactide were bought from Merck. The ring opening initiator stannous octoate was also bought from Merck. Nitrogen gas was utilized to create an inert atmosphere. Acetone was used to dissolve the finished polymerized product, while MQ-water was utilized in the washing steps.

4.1.4 Glassware and setups for polymerization of poly-dopamine and PLGA on IONCs

The following parts were utilized in the polymerization of polydopamine and PLGA:

- 100 mL Beaker with magnet for oxidation polymerization of poly-dopamine on IONCs
- 10 mL measuring cylinders for washing steps of poly-dopamine coated particles
- Magnetic stirrer for the polymerization of poly-dopamine
- Magnetic stirrer with in-built heater for PLGA coating
- Two-necked flask for polymerization of PLGA on poly-dopamine coated IONCs
- Nitrogen gas inlet for PLGA polymerization
- Needle for purging the PLGA polymerization beforehand
- Magnet and beakers for washing steps

4.2 Methods

4.2.1 Thermal decomposition synthesis of nanospheres

For the Separation optimization of the TREG particles, thermal decomposition of TREG nanospheres was conducted in regards to a study by Maity. D et al.2009[52] where 2 mmol of iron acetyl acetonate ($Fe(acac)_3$) was mixed together with 20 mL of triethylene glycol ($TREG$). The particles were heated with a heating rate of 20 ℃ per minute up to 120 ℃ and then dehydrated at this temperature for 1 hour before the heat was increased to 280 ℃ for the nucleation and growth stage of the synthesis. The solution was left stirring at this temperature for 2 hours. The particles were then washed in a mix of the anti-solvent ethyl acetate (EtAc) at volume of 20 mL and the solvent ethanol at volume of 10 mL. Both magnetic separation and centrifugation separation was utilized to separate the particles after addition of the anti-solvent EtAc. The centrifugation was done in a Multifuge where the particles were centrifugated at 14500 rpm for 10 minutes and the supernatant was retracted between with a pipette. After being washed and re-dispersed 3 times respectively for both separation methods, the particles were finally dispersed in MQ-water before being stored in a fridge at 4 ℃. The setup for the typical TREG synthesis is shown in Figure 4.1.

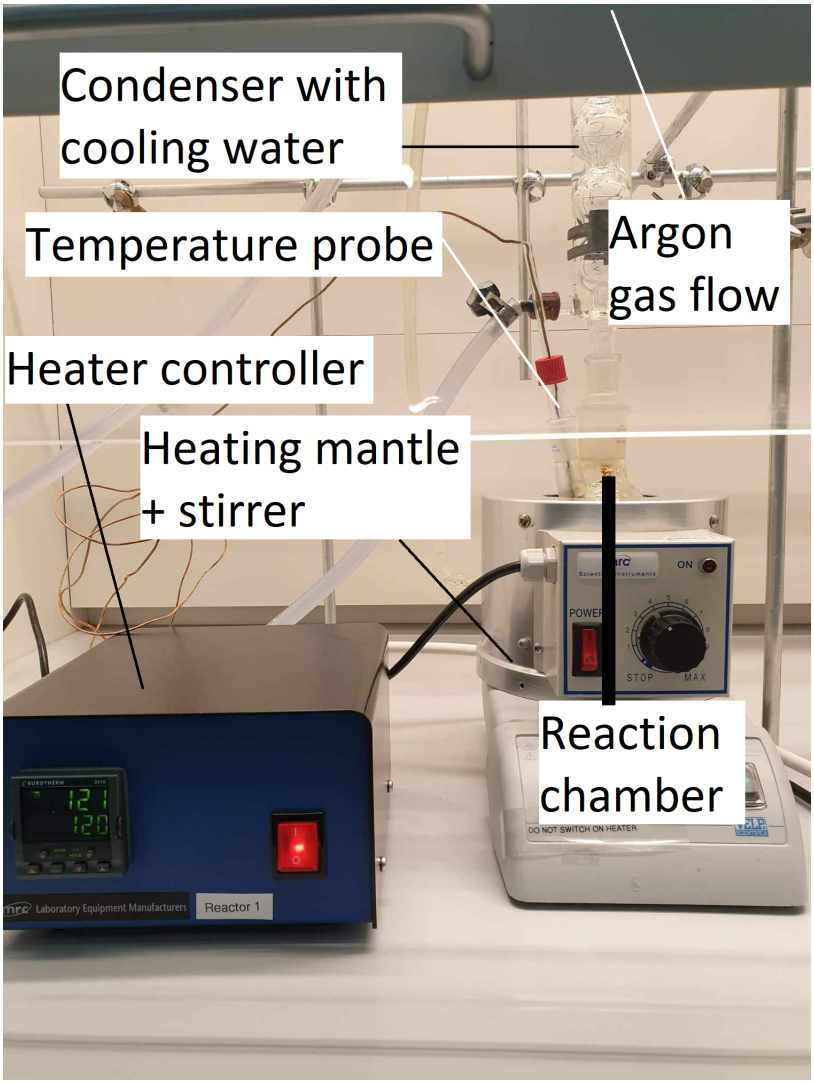

Figure 4.1: Setup of iron oxide nanospheres synthesis in separation optimization

To optimize the process which in this thesis was referred to as the TREG optimization some chemical parameters were changed. In the TREG optimization, varying masses of iron precursor $Fe(acac)_3$ which ranged from 1-3 mmol or 0.35-1.07 g was mixed with 20-30 mL of TREG under inert atmosphere of argon. The solution was also left under constant stirring at 400 rpm and cooling of 15 ℃. A balloon was applied to capture any residual pressure due to some pressure difficulties in the early work of the separation optimization. The system was then heated to 120 ℃ for 1 hour with a heating rate of 20 ℃ per minute. After 1 hour of the solution being dehydrated at 120 ℃, the temperature was increased to 280 ℃ again with the heating rate of 20 ℃ per minute. The solution was then left at this temperature for 2 hours before getting cooled down to room temperature for 30 minutes. The particles were then washed as stated in the separation optimization, but separated using only magnetic separation. The setup for the optimization TREG synthesis is shown in Figure 4.2.

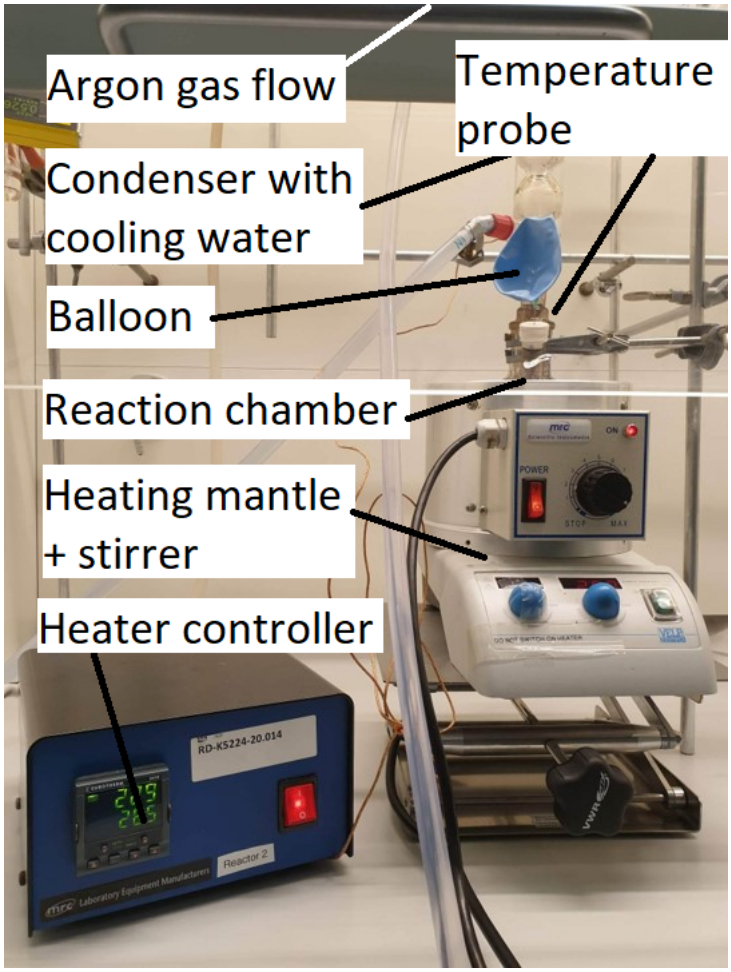

Figure 4.2: Setup of iron oxide nanospheres synthesis in TREG optimization

To give a more thorough understanding of how the washing procedure was conducted, a schematic for the washing procedure of the particles are shown in Figure 4.3.

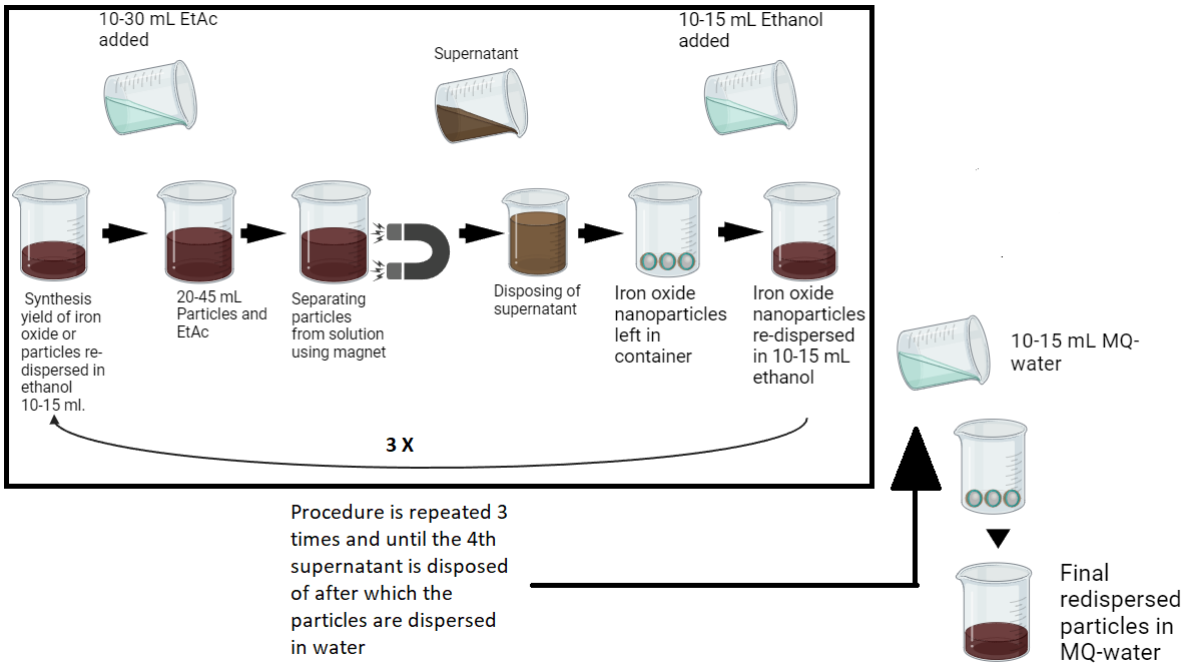

Figure 4.3: Schematic showing washing procedure of iron oxide nanospheres and iron oxide nanoclusters

After the washing steps the particles were re-dispersed in 10-15 mL MQ-water depending on the batch which is shown in the last stage of the figure, and then stored in a fridge at 4℃.

4.2.2 Thermal decomposition synthesis of nanoclusters

Iron oxide nanoclusters were synthesized with TREA(Triethanolamine) at a volume of 16 mL combined with 4 mL of TREG as derived from one of the syntheses conducted by Maity. D et al.2011 [26]. The respective experiment is referred to as the 4:1 TREA:TREG synthesis in their study. For this synthesis, the solution was again dehydrated by increasing the temperature to 120 ℃ and leaving it for 1 hour. The temperature was then increased to 260 ℃ before being left to stir at 300 rpm for 1 hour. The reaction was run with a cooling water temperature of 4 ℃. The washing and re-dispersion steps remained the same as for the nanospheres as shown in figure 4.3. The only separation technique used for the clusters was magnetic separation. A depiction of the thermal decomposition setup for iron oxide nanoclusters is shown in Figure 4.4.

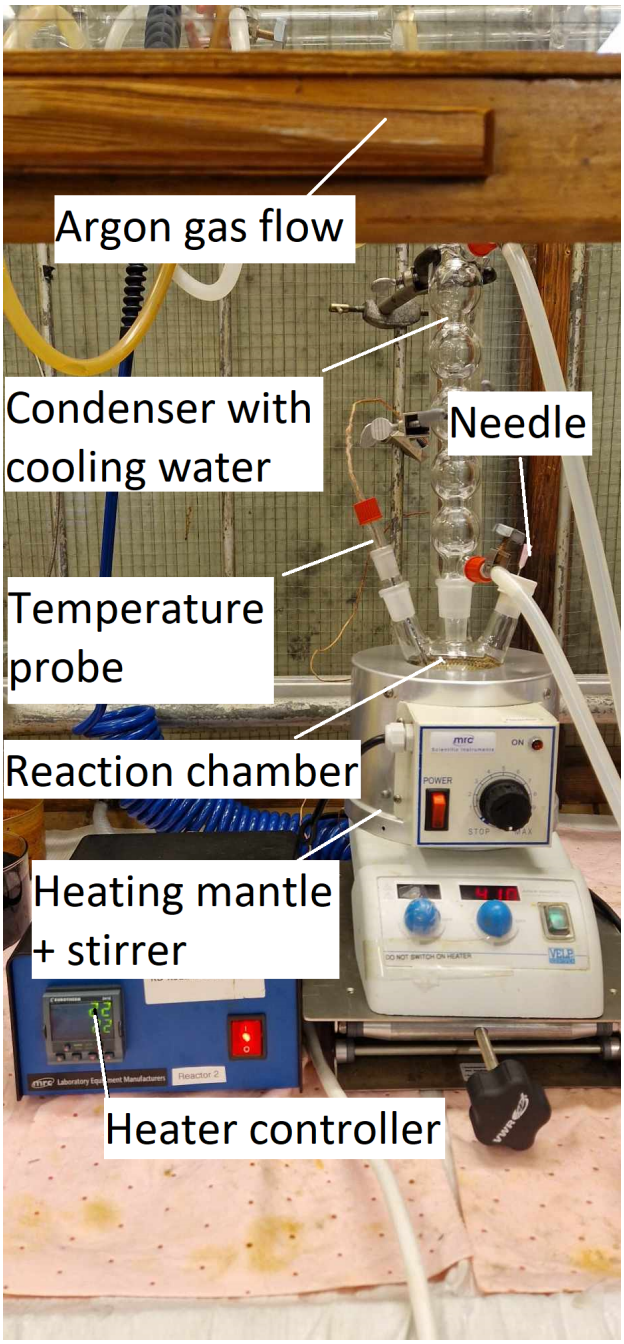

Figure 4.4: Setup of iron oxide nanoclusters synthesis

4.3 Preparation of Polydopamine coated nanoclusters

When polymerizing the polydopamine on top of the IONCs the method used was derived from Mrówczyński. R et al. 2014[43]. Due to higher quantities of powders, the polymerization was scaled down. Typically 6 mg of iron oxide nanoclusters(IONCs) depending on set of experiment were dispersed in 30 mL of tris-buffer at concentration of µM was prepared to stabilize at pH 8.5. together with 6 mg of dopamine hydrochloride (DHCl) again depending on set of experiments. The IONCs were left for respectively 2, 4, 8 and 24 hours to react with the DHCl in normal conditions through the use of an oxidation mechanism where the dopamine hydrochloride is oxidized on the surface of the clusters to create polydopamine. After polymerizing for 2-24 hours, the particles were retracted at different retraction times of 2, 4, 8 and 24 hours and washed 3 times with MQ-water to get rid of excess dopamine hydrochloride in the solution. Some particles were then dried while others were characterized using different techniques before the final coating step of PLGA. The preparation route for the polydopamine surface functionalization is shown in Figure 4.5.

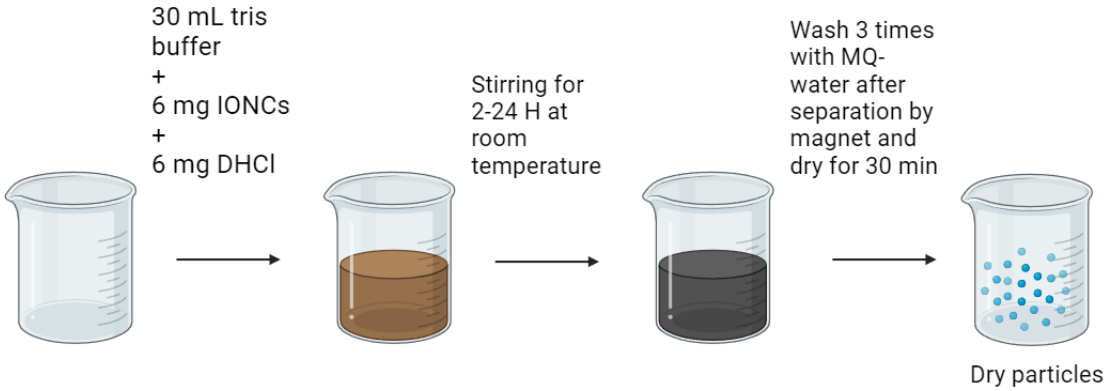

Figure 4.5: Visual representation showing oxidative polymerization of polydopamine (PD) on top of IONCs

4.4 Polymerization of PLGA on polydopmaine coated nanoclusters

The procedure of coating the PDCIONCs with PLGA was derived from Al-Natour. M et al.[60] Again the quantity of the reactants used were scaled down before conducting the polymerization. For the polymerization, 460 mg gyloclide and 900 mg lactide in a respective ratio of about 35:65 were melted. Stannous octoate was added to the mixture in the ratio of 0,5 wt/wt% of the total mass of the monomers lactide and glycolide. This corresponds to 6µL. 6 mg dry polydopamine coated nanoclusters depending on the experiment were then added to the mixture. The reaction was purged for 30 minutes after which the polymerization was run for 3 hours. The particles were then dissolved in acetone and washed 3 times with MQ-water to hydrolyze and remove the excess PLGA and remove the unreacted monomers. The preparation route for the PLGA surface modification on top of the PDCIONCs is shown in Figure 4.6.

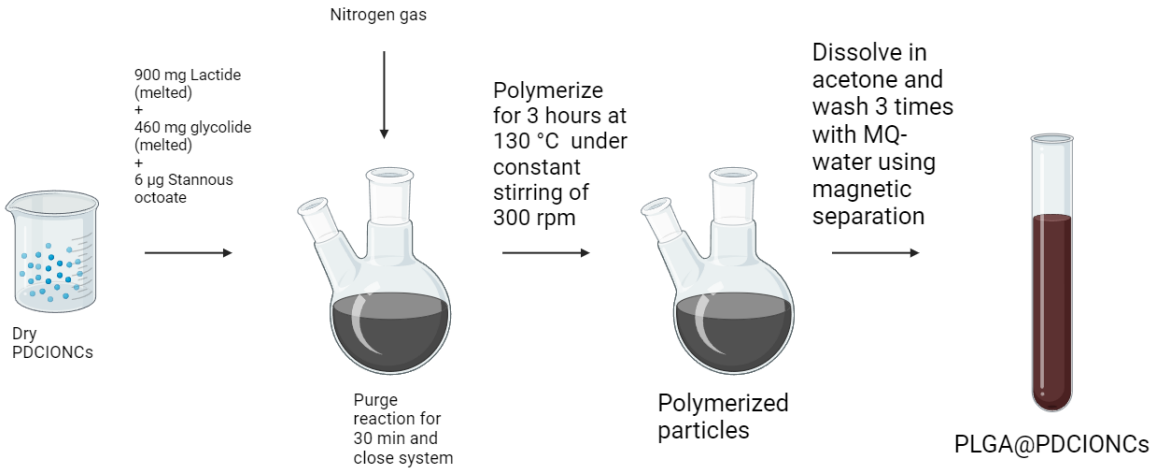

Figure 4.6: Visual representation showing Solvent-free polymerization of PLGA on top of PDCIONCs

4.5 Stability studies

Stability studies were conducted for all kinds of bare and coated nanoclusters to see how the particle charge would behave in different environments. The stability is based on the zeta potential change in different pH. The goal was to see if there are any significant differences in stability between the coated and non-coated particles that proves or indicates the presence of the coating. The zeta curve was made by dispersing particles in vials of MQ-water. 0.1 M sodium hydroxide or 0.1 M hydrochloric acid were respectively added to the vials to either increase or decrease the pH of the solution where the particles were dispersed. Since the charge of the particles are pH responsive one would expect to get different zeta potentials. The different zeta potentials measured would then create the zeta curve. The particles were measured in the pH range of 3-11. The point of zero charge could also be found using this method and make the method comparable with the literature. The practical reason for measuring the stability is to see how the particles would behave *in vivo* with the reactive sites in the human body and how the kinetics could be considered when knowing the behaviour in the different environment. It would also be informative to see which pH the particles should be delivered within as when they are injected to perhaps release a drug or to have them as stable as possible. The typical stability area of the particles were presented by Sing. N et al. where everything above +20 mV and below -20 mV is considered stable [54]. A typical change in the surface charge of a particle at different pH is shown in figure 4.7.

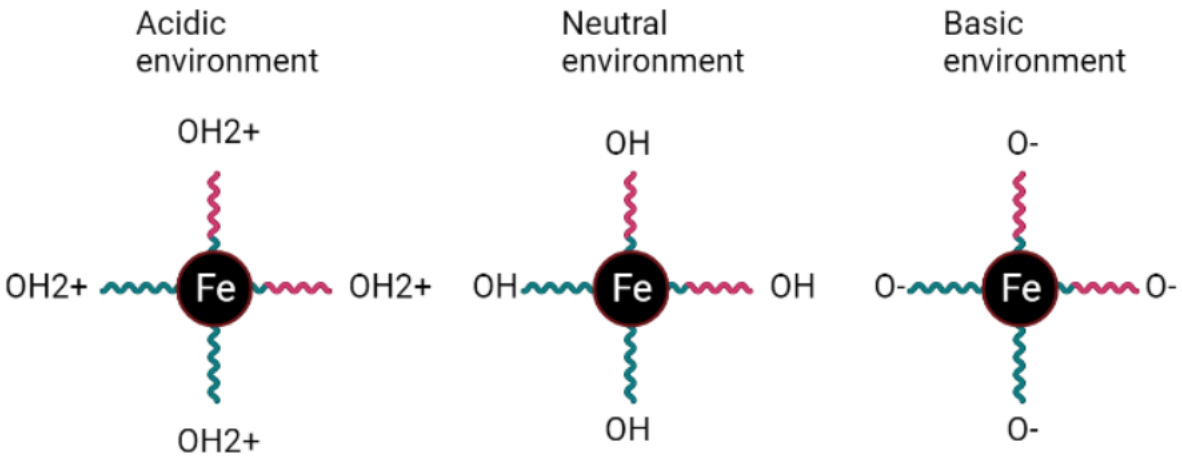

Figure 4.7: Particles changing surface charge behaviour at different pH-based environments.

Figure 4.7 shows that when having different environments depending on pH one would get changes in the groups of the particles. The acidic environment tends to protonate in this case the hydroxyl groups of the particles while in neutral pH the charge tends to be neutral. The basic environment tends to deprotonate the hydroxyl groups on the particles as can also be seen in the figure. The pH dependence of the charge in the particles are therefore crucial to observe when introducing drug delivery agents or site targeted particles. The charges of the particles could typically change at different pH‘s depending on the chemical composition of the particle, which means that the respective surface group of a particle would have different points of zero charge and different stability pattern. Due to zeta potential being decided by amounts of particles being positively, neutrally or negatively charged, one could see where most particles would be within the desired application area and hence control the pH before applying it to the desired application area.

4.6 Drug loading of salisylic acid into PLGA@PDCIONCs

The PLGA@PDCIONCs where attempted drug loaded by using salisylic acid (SA). The method used was almost the same as used in Sundar. S et al.[59] where they attempted to load the anti-cancer drug curcumin into amine-functionalized iron oxide nanoparticles. Salisylic acid was used instead due to its smaller molecular structure. The method was also scaled down a bit to use the yield from the PLGA@PDCIONCs. The way the loading was conducted was by adding 10 mL of MQ- water to 3 separate vials and 5 mg SA was added to the aqueous solution. The pH was then stabilized using sodium hydroxide to respectively pH 4, 7 and 10. The solutions were then measured in the UV-vis before 3 mg of PLGA@PDCIONCs were added to every solution. The solutions with the dispersed particles were left stirring for 3 hours. 2 mL of each solution were then washed once with MQ-water while 2 mL of each solution were left unwashed. The washed and unwashed particles were measured using the pure PLGA as a reference point of absorption in the

UV-vis before retrieving the data from the UV-vis. The particles were finally measured using light scattering to see if there would be any indication of interaction between the PLGA@PDCIONCs and the salisylic acid.

4.7 Characterization techniques

4.7.1 Dynamic light scattering *DLS*

The particles hydrodynamic size and zeta potential was measured using an Anton Paar Litesizer 500 instrument. All particles except the PLGA@PDCIONCs were diluted with a dilution factor of 1:50. The PLGA@PDCIONCs were diluted 1:10. The particles were measured using intensity weighted measurements. The way the particles were measured is that different particles scatter light at different intensities. This means that when the particles are exposed to the light inside the Litesizer, they would scatter light at different intensities. Since this is happening directly on the surface of the particles, one could typically expect different hydrodynamic size after coating the particles. This means that any organic layer on top of the particles as well as aggregates can impact the hydrodynamic sizes of the particles. The particles were measured through 3 main measurements done with 100 runs each that measured different angles of the particles from auto adjustment. The measurement principle of hydrodynamic size is based on the Brownian motion of the particles. The hydrodynamic sizes are derived from the Stokes-Einstein equation which is displayed in equation 4.1.

$$D = \frac{k_B T}{6\eta\pi R_H} \tag{4.1}$$

where D is the diffusion coefficient, K_B is the Boltzmann constant, R_H is the hydrodynamic radius, η is the viscosity and T is the temperature[61]. The iron oxide nanoparticles were measured at 40-60% transmittance due to signal to noise ratio, which makes that area the most representable.

4.7.2 Scanning transmission electron microscopy *S(T)EM*

The scanning transmission electron microscopy (S(T)EM) was utilized to measure the "dry size" of the particles. The particle measurements were conducted in a Hitachi SU9000. The particles were mostly measured using bright field S(T)EM mode due to the settings being the most suited for the iron oxide nanoparticles. Some particles were also depicted in the secondary electron mode. The measuring principle of S(T)EM is based on an electron beam targeting each particle through a scan mode that gives resonance back and depicts the particles in the software. The particle pictures taken in the instrument were transferred as a picture files and then transferred to the ImageJ software to be measured by scaling each pixel to a certain nanometer range. Up to 500 particles were measured for each sample through circling or using a cross-section measurement method on the particles. The circular particle diameter was then found by deriving the size from the area of the pixels in the sphere. The clusters and bigger particles were measured at the average of the two cross-sections to find the particle diameter. Instead of selectively picking uniform particles only, the particles were randomly chosen to give a representative

size of the total particle suspension. The way the polydispersity in S(T)EM was calculated is shown in equation 4.2 and was retracted from Raval. N et al[62].

$$PDI = (\frac{\sigma}{d_N})^2 \tag{4.2}$$

where σ is the standard deviation of the particles and d_N is the mean particle size.

4.7.3 Vibrating sample magnetometer *VSM*

The vibrating sample magnetometer (*VSM*)

The particles of IONPs and IONCs were measured in a Princeton MicroMag VSM. The field strength was set to 10 kOe which is nearly the max of the instrument to see clearly the magnetic properties of the nanoparticles. The measurements of the samples were done to find the saturation magnetization M_s of the particles through hysteresis loops. Saturation magnetization values were given in emu/g. The hysteresis loops were normalized by mass to see how much the particles would differ in terms of emu/g. Paramagnetic adjustment was neglected as most of the particles seemed to possess nearly perfect superparamagnetic activity. If they however did possess a lot of ferromagnetic activity one should have adjusted the data as they are two different properties[63]. The way the particles were prepared was by dispensing 3-5 mL of dispersed particles in a glass vial. The particles were then dried for 2 days in an oven with 65 ℃ before being transferred into the weighed tubes. The samples were preferred to have a mass of 5 mg or above to give a more indicative result of the saturation magnetization. This was not necessarily the case for all the samples as the yield of particles in their final tubes could vary a lot. The VSM principle is based upon Faraday‘s law of induction which is displayed in 4.3[64].

$$\epsilon = -N\frac{\Delta\phi}{\Delta t} \tag{4.3}$$

where ϵ is the induced voltage, N is the number of loops, $\Delta\phi$ is the change in magnetic flux over Δt time.

4.7.4 Magnetherm

The particles of IONPs, IONCs and PLGA@PDCIONCs were measured in a Nanotherics Magnetherm to see how well the particles would oscillate and create heat when applying an external alternating magnetic field (AMF). The instrument measures the heating rate of particles when applying an AMF over time and shows the increase of degrees in ℃ each second or however one wishes to adjust it. The field strength was attempted maximized at 18x the Brezovich factor which is set to $4.5*10^8$ A/ms, but also set at 5x the Brezovich factor which is within the new suggested limits in the literature. The measurements used were the ones of the 5x Brezovich limit. From this method, one could calculate the heating rate per minute and see how well different kinds of particles perform at the different limits of the AMF. There were lots of options which were both within and outside of the Brezovich limit. Another important value derived from the magnetherm measurements were the specific absorption rate known as the SAR value which is measured in W/g. The

way the SAR values are derived can be found in the theory chapter in equation 2.15. The better the particle heating rate performs, the higher the SAR values become since they are directly correlated. The particles were prepared for the magnethemr measurements by diluting the particles to a concentration of 0.5 mg/mL before inserting them into the instrument. A cooler made sure that one would start the measurement at about 25 ℃ for every measurement. The particles were then exposed to the AMF and their temperature started to increase. After the measurement was done, the SAR could be retracted as data and the heating rate per minute could be calculated.

4.7.5 X-ray diffraction *XRD*

The crystallographic structure measurements of all the particles were conducted in a Bruker Da Vinci XRD instrument. The particles were measured by X-rays that strike out different diffraction angles of the particles and how they spread. The graphs were displayed in peak intensity vs 2Θ The measurements were done in 5-70 degree angles and the analysis was done for 2 hours at a slit of 0.2. The diffraction shown by the particles give different peak signals at a given range depending on the phase or species of particles. These ranges can be matched with for instance in this scenario bulk magnetite Fe_3O_4. The peaks would then perhaps also match other substances like maghemite Fe_2O_3 which would indicate that both phases would be present in the measured powder. The samples were prepared using a special holder called a kapton holder. The surface used was a flat silica wafer. A droplet of the dispersed particles were dispensed on top of the silica wafer before drying for at least 1 hour. The dried sample was then coated by a kapton film to make sure dry nanoparticles did not float in the air when handling the particles. The sample was then set to be measured in the Da Vinci instrument before getting the different lattice peaks of the measured particles. These peaks were then measured to if there would be any correlation to the target materials. The general equation used when measuring XRD peaks and particle sizes in the instrument is called the Debye-Scherrer equation. The equation is shown in equation 4.4[65].

$$D = \frac{K\lambda}{\beta \cos\theta} \tag{4.4}$$

where D is the particle size, K is the Scherrer constant, λ is the wavelength of the X-ray, β is the width of the diffraction peak and θ is the Bragg angle[65]. The crystallite size of the particle can also be derived from the equation.

4.7.6 Fourier-transform infrared spectroscopy *FTIR*

FTIR measurements were done in a Bruker Vertex 80v to identify the presence organic functional groups as well as the iron oxide bond. To measure particles in the FTIR one has to up-concentrate a sample. The sample was then dispensed on top of a diamond crystal on an Attenuated total reflection (ATR) plate. The sample was then dried using a heat gun at 100 ℃for a couple of minutes or until the water was visibly gone to measure only dry sample of the bare and coated particles. This is to reduce the potential harm of the instrument when water interacts with vacuum. In a typical analysis using FTIR, an ATR with a dried sample was measured in vacuum or in normal conditions, measured through

100 runs and retracted. The bare and coated particles were compared to literature spectra as well as reaction solvents and monomers for the respective syntheses. The analysis of solvents and monomers were done in the presence of CO_2 at normal conditions.

4.7.7 Ultra violet visible light absorption *UV-vis*

The particles were measured in an Agilent Cary 60 UV-vis to see if there would be any difference between the particle's peaks before and after coating. UV-vis is a measuring method were particles are exposed to light in the visible range. For these measurements the typical range was from 300-900 nm and the particles that are irradiated in the measuring range give off local surface plasmon resonance peaks better known as LSPR peaks from oscillation depending on how the particles behave in the specific region of absorption[66]. The particles were prepared by setting the concentration of the sample, before inserting it into the instrument. The particles were then irradiated and data comes out at different light irradiation ranges. When measuring the UV-absorption in the instrument it uses an equation. This equation is known as Bouguer-Beer-Lambert law which is shown by Dr. Thomas. G et al.[67] in equation 4.5.

$$log_{10}\frac{I_0}{I} = A = \epsilon * c * d \tag{4.5}$$

where I_0 is the initial intensity, I is the intensity, A is the absorbance, ϵ is the molar absorption coefficient, c is the concentration and d is the layer thickness or length of the light path[67].

This formula gives rise to each absorbance measurement and can finally show the difference between the peaks after irradiating light at the wavelengths of 300-900 nm on the nanoparticles. The final result is a graph of the absorbance that can be characterized and helps differentiate between different kinds of particles. The particles were prepared by diluting them to 0.5 mg/mL. They were then put into the instrument and scanned by using a blank as a starting reference. The bare IONCs, PDCIONCs, PLGA@PDCIONCs, washed and unwashed drug loaded PLGA@PDCIONCs were measured in the UV-vis using this method.

5 Results and discussion

This chapter will present the results from experiments done towards iron oxide nanoparticles with different sizes, morphology, stability and magnetic properties. The chapter will also include modification of surface properties in these particles by coating them with different surface modifications, where amines and carboxylic groups will be the main surface modifications. Different characterization techniques of surface modified and bare particles will be presented and discussed. Characterization data includes hydrodynamic size, Zeta potential, "dry size", UV absorption, chemical bond identification, magnetisation saturation, specific absorption rate, crystalline intensity and monodispersity of particles. To better understand and engineer a good particle towards hyperthermia and drug delivery, all of these parameters should be investigated. To create a more effective hyperthermia, every data characterized counts towards the final product and makes the results and discussion section the most important part within a project. Other non-relevant data from experiments conducted towards the thesis can be found in appendix.

5.1 Optimization of separation techniques and washing steps

Thermal decomposition synthesis was used to produce iron oxide nanoparticles following the synthesis procedure conducted in a study by Maity. D et al.2009 [52]. Separation techniques were then attempted optimized by comparing particles separated using magnetic separation and centrifugation separation through different characterization techniques. The most suited separation technique would later be utilized in the later studies of the thesis. It was also attempted to optimize the washing process by varying volume of the anti-solvent *Ethylacetate* and see it's impact on the the final particle properties.

Figure 4.3 in the Methods section shows how the magnet was utilized as a separation tool. Centrifugation was done before and between separating the particles from the supernatant. The reason for trying to optimize the particles towards either centrifugation or magnetic separation was to see if the particles in terms of magnetic properties and size would be affected for the respective separation method.

A hypothesis would be that the magnetic separated particles would prove more suitable as they are separated using a magnet, which means that only the most magnetic particles would be present after washing. Another hypothesis would be that the amount of anti-solvent would impact the sizes of the particles as well as magnetic properties.

The particles synthesized in the separation optimization study, referred to now as The "separation optimization particles" were synthesized using 2 mmol of iron acetyl acetonate and 20 mL triethylene glycol. The resulting particles were then split into 4 different tubes of 5 mL NP-solution in each. The varying set of parameters are shown in Table 5.1 where M stands for magnetically separated particles and C stands for centrifugation separated particles. Different volumes of washing anti-solvent EtAc represents the different numbers on the respective batches, where 5 is 5 mL addition of EtAc and 10 is 10 mL addition of EtAc. The molecular weight of iron acetyl acetonate is 353.17 g/mol which means 0.71 g was used for these batches.

Table 5.1: Table showing the different batches of centrifugation separated and magnetically separated particles with different washing ratios of ethyl acetate.

Batch	$Fe(acac)_3$ in millimoles (mM)	Volume of TREG in mL	Ratio of EtAc to ethanol
M 5	2	20	1:1
M 10	2	20	2:1
C 5	2	20	1:1
C 10	2	20	2:1

The four tubes of 5 mL synthesis product were respectively washed with the presented volumes of the *EtAc*. The particles showed some difficulties in magnetic separation. The separation times were different for each washing step. A table displaying time of magnetic separation is shown in Table 5.2

Table 5.2: Table showing batches respectively synthesized in the separation optimization and the different separation times for the respective batches synthesized in minutes and seconds.

Batch	1st sep time	2nd sep time	3rd sep time	4th sep time
M 5	5 m	4 m	3 m	3 m 30 s
M 10	1 m 20 s	50 s	1 m 30 s	2 m

Table 5.2 shows that the particles were separated faster using a 2:1 ratio of *EtAc*:ethanol. The higher volume addition of the anti-solvent did also however seem to have some interaction with the particle surface as one would not typically predict that the separation times would increase after decreasing. What was common for both magnetic separation batches was that they both stopped separating after a certain time leaving a slurry supernatant behind. The typical slurry solution can be seen in Figure 5.1.

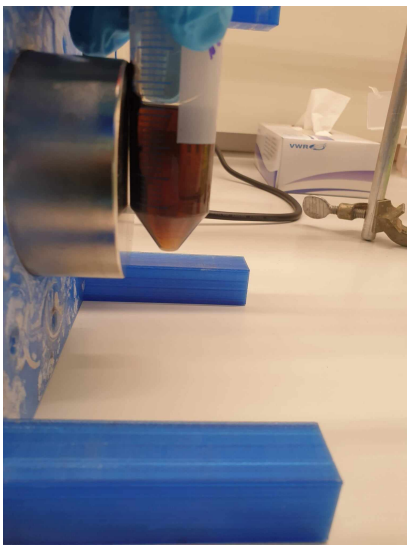

Figure 5.1: Magnetic separation of iron oxide nanospheres in solution

This could indicate that particles that were not magnetic enough to be retracted or

particles that are not within the superparamagnetic range as stated in the theory section were left in the supernatant.

Centrifugation separated particles left behind a close to clear supernatant between each separation. This also became more and more clear after each separation step indicating that it could be only the absolute smallest particles that were disposed of in the supernatant. Since the separation proved to give a clear supernatant between each step one could also predict that there would be a wider size range in the centrifugation separated particles. The particles concentration were found to be around 5 mg/mL.

5.1.1 Suggestion of reaction mechanism in synthesis of SPIONPs

A reaction mechanism of the TREG synthesis of iron oxide nanospheres was derived from a study done by Ambrozic. G et al. 2011 [68]. The study suggested a reaction mechanism forming zinc oxide nanoparticles through microwave assisted decomposition of zinc acetyl acetonate in 1-butanol.

The study suggested a pathway where 1-butanol which is similar to TREG conducts a nucleophilic attack on the acetyl acetonate of the zinc precursor. The study suggested that resulting water from the nucleophilic attack would hydrolyze the carboxyl group formed by the attack and remove it. In the next step it was suggested that the water being attracted to the zinc would retract the remaining ketone group before finally creating a zinc hydroxide monomer. The zinc hydroxide molecules would in the end poly-condensate to create the zinc oxide structure. Since magnetite is a bit different, the following suggested synthesis pathway might differ a bit from the synthesis of the zinc oxide. TREG is also known to form a layer to stabilize the particles as shown in a study by Günay. M et al. [69] where they stabilize $MnFe_2O_4$ nanoparticles with TREG. The theory also states that capping agents often work as surface modifying agents. This was also taken into action in the suggestion. The suggested reaction mechanism of iron oxide nanospheres synthesized in TREG is shown in Figure 5.2.

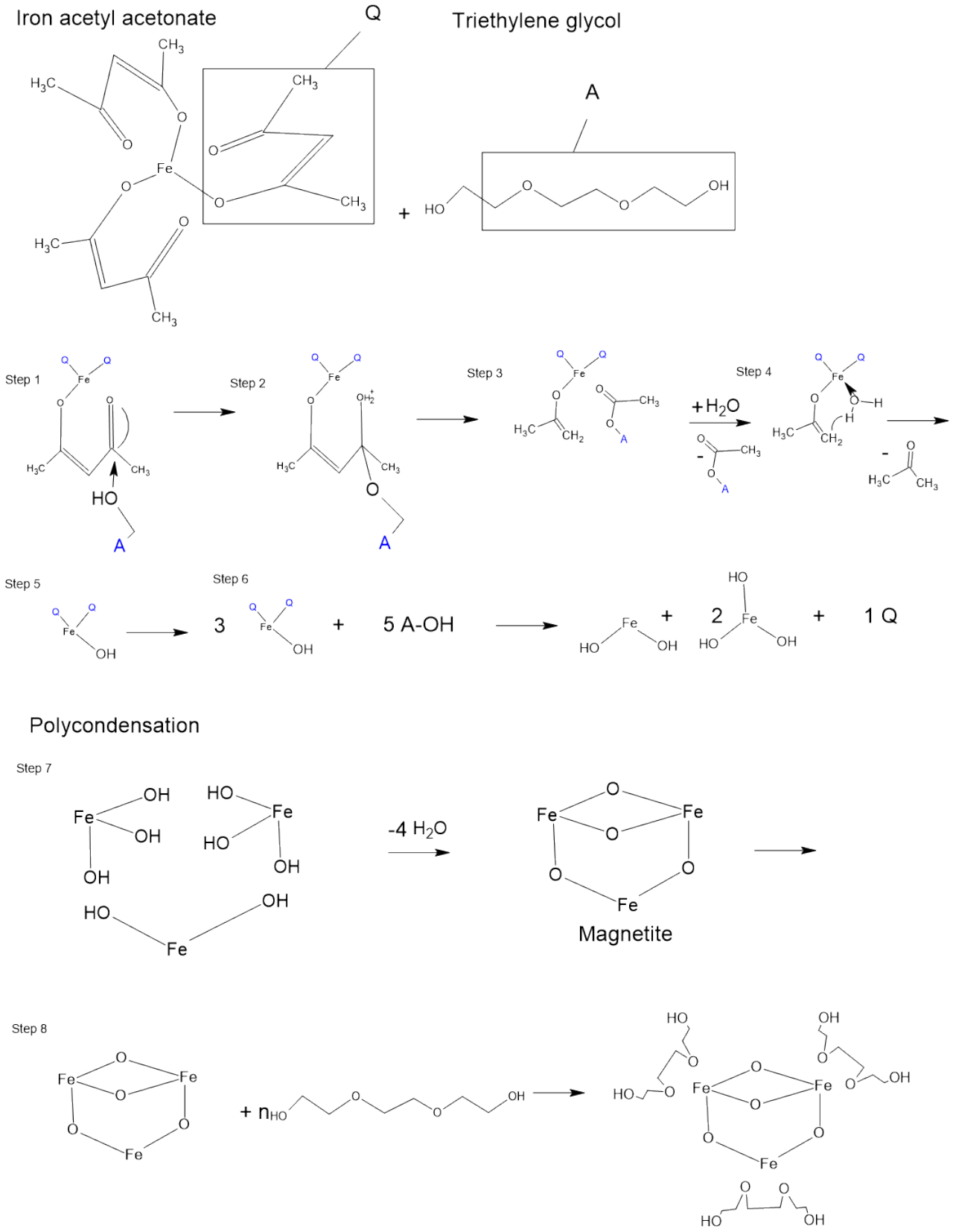

Figure 5.2: Suggested reaction mechanism of iron oxide nanospheres from the TREG synthesis using iron acetyl acetonate and triethylene glycol as reactants.

Figure 5.2 shows how the potential formation of magnetite occurs as well as the coating of the stabilizing agent TREG. What is important to notice is that this suggestion is based on a singular molecule of magnetite. Maghemite might also exist among the synthesized particles. The particles is also possibly made up by several magnetite and maghemite molecules forming a different lattices. A way to prove how many molecules are within each particle would be to quantify iron and hydroxyl groups in the particles to find the ratio. With the ratio one could predict or approximate how many magnetite or maghemite molecules there would be vs the hydroxyls in the possible TREG layer. Another important detail is that microwave decomposition can act differently than thermal decomposition and hence create a bit of a different reaction mechanism than what was suggested by the study by Ambrozic. G et al. 2011[68].

5.1.2 Hydrodynamic size from Dynamic light scattering *DLS* and zeta potential of separation optimization IONPs

The hydrodynamic sizes of the centrifuged and magnetically separated particles with different washing volumes were measured and are shown in Table 5.3

Table 5.3: Table showing separation optimization iron oxide nanospheres respectively measured in terms of hydrodynamic size, poydispersity index and zeta potential.

Batch	Hydrodynamic size in nm	poydispersity index in %	Zeta potential in mV
M 5	166 ± 3	25 ± 1	28 ± 1
M 10	167 ± 2	20 ± 3	27 ± 1
C 5	124 ± 1	20 ± 1	30 ± 1
C 10	142 ± 2	22 ± 2	28 ± 1

Table 5.3 shows that hydrodynamic size was different between the centrifugation separated particles and magnetically separated particles. A reason for this could be that the TREG layer is less likely to be impacted when magnetically separating the nanoparticles due to less force on the bonds/interactions between the particles. When using centrifugation separation, the TREG layer could potentially be deformed or changed due to strong centrifugal forces. To prove this, more batches should be prepared as there are too few batches to predict a certain trend. When compared to the literature, the hydrodynamic size of the iron oxide nanoparticles did not correspond well to the study by Maity. D et al. 2009[52] where the hydrodynamic size of the particles was found to be 13 nm, but this could also be due centrifugation separation done several more times than 3. The zeta potential proved to be similar for the four batches, but lower than what was reported by Maity. D et al. which was +40 mV. To see the difference in poydispersity between the batches more easily, the intensity weighted particle size distribution is shown in Figure 5.3.

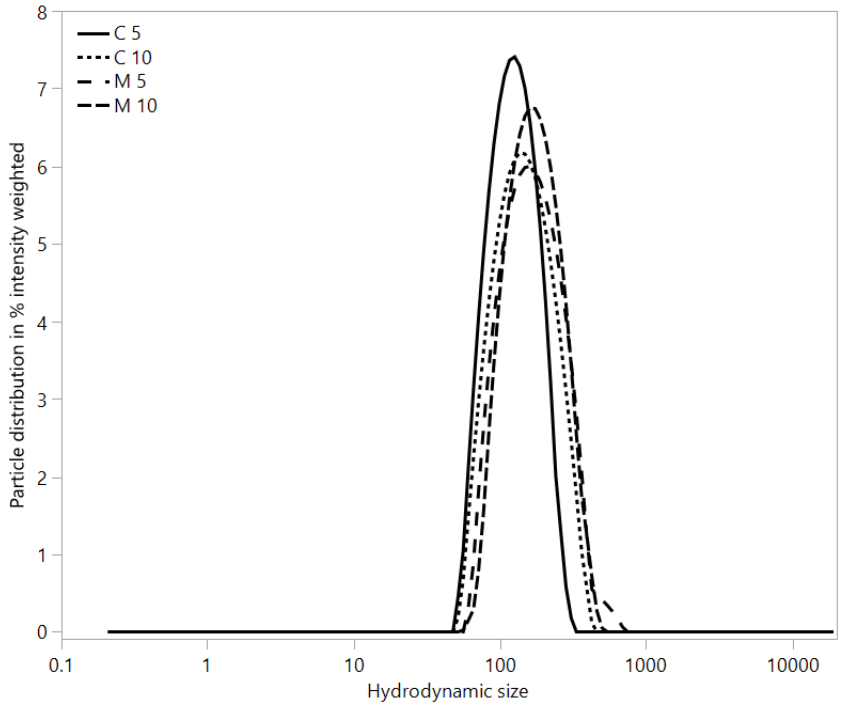

Figure 5.3: Hydrodynamic particle size distribution in % intensity weighted of separation optimization iron oxide nanospheres.

Figure 5.3 shows that the peaks between the different batches produced seemed to be well correlated with small differences. Since the peaks are this similar, it seems like there were no apparent trend between the particles in terms of the poydispersity. The study done by Maity. D et al 2009[52] shows a similar peak when it comes to the poydispersity, but at around 13 nm instead of around 100 nm which was the case for the separation optimization particles. The particles in Maity. D et al. could also have been measured at number weighted measurements, which was observed to give lower sizes throughout the thesis work. This measuring method was not utilized as it would not typically include larger particles and focus on smaller ones[61].

5.1.3 Scanning transmission electron microscopy *S(T)EM* of separation optimization IONPs

"Dry sizes" in S(T)EM were measured to see if there was any significant difference between the two separation methods in the particle size. For this shorter study, 100 particles were measured for each batch. The sizes from the S(T)EM imaging are shown in Table 5.4 with belonging standard deviations and poydispersity.

Table 5.4: Table showing sizes and poydispersity derived from S(T)EM for separation optimization iron oxide nanospheres.

Batch	poydispersity in %	S(T)EM diameter in nm
C 5	5.6	9 ± 2
C 10	3.0	6 ± 1
M 5	2.9	8 ± 1
M 10	1.9	7 ± 1

Table 5.4 shows the different sizes and poydispersity in %. The particles showed no apparent trend other than a possible difference from the C 5 batch which seems to have produced bigger sizes of particles than the average of the others. To prove this properly, more particles should have been counted as it could give a larger variation of particles within all the respective batches. Since all batches were produced using the same synthesis parameters, it would be difficult to argue that the sizes are different as the washing and separation should not impact the synthesis of the particles. If particle sizes are dependent on the TREG layer, the higher volume addition of the anti-solvent could be an indication of reducing the particle size. This would need more research to be proven. Maity. D et al. 2009[52] achieved sizes in S(T)EM of around 11 nm. For the separation optimization particles, most sizes measured in S(T)EM seemed to be smaller except C 5 with a standard deviation lying within the range of what was reported.

To give a better visual of the poydispersity within the particle batches, an example of how the particle size distribution was measured. A visual representation of the particle size distribution in numbers of Batch M 10 is shown in Figure 5.4.

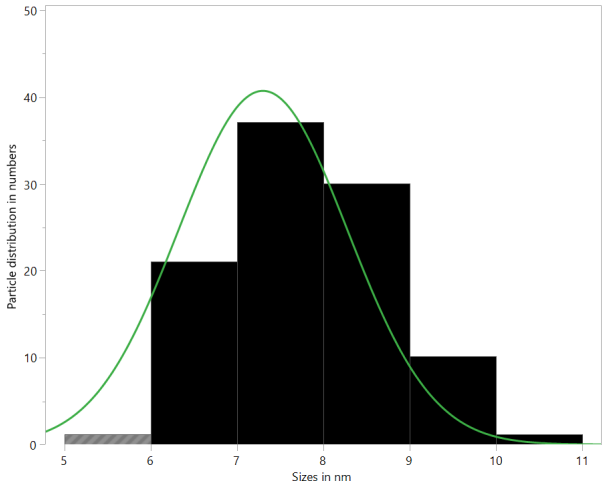

Figure 5.4: Particle size distribution in numbers of separation optimization batch M 10.

All particles were then depicted to see if there are any trends within the different separation optimization iron oxide nanoparticles. All the particle size distributions in numbers are shown in Figure 5.5.

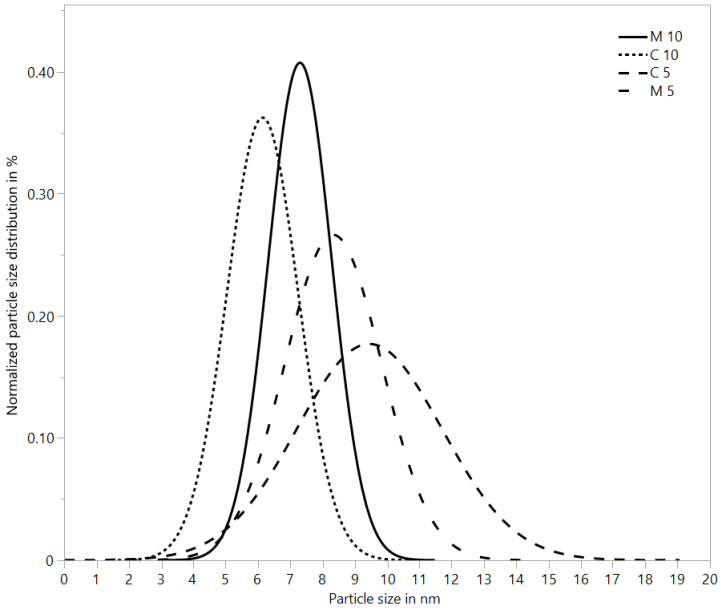

Figure 5.5: Particle size distribution of separation optimization iron oxide nanospheres in S(T)EM normalized by % where 1.0 = 100%.

Figure 5.5 shows the different particle size distribution in % of all the separation optimization batches. It was observed that the particles washed with the higher volume of *EtAc* seemed to give a narrower particle size distribution, but lacking numbers of particles counted and too few samples to compare it would not be possible to conclude the trend. The study done by Maity. D et al.2009[52] did not mention any particle size distribution other than that the dry sizes of the particles were around 11 nm.

5.1.4 Vibrating sample magnetometer *VSM* of separation optimization IONPs

The results of the saturation magnetization values and it's belonging mass were displayed in Table 5.5.

Table 5.5: Table showing mass of particles measured from respective batches and saturation magnetization retrieved from measurements done in the VSM for the separation optimization.

Batch	mass of particles in mg	Saturation magnetization M_s in emu/g
C 5	8	49
C 10	12	53
M 5	10	51
M 10	21	49

Table 5.5 shows that the saturation magnetization is similar for all the batches. It was proven that the particle's saturation magnetization was far from the bulk magnetite which has a M_s value of 92 emu/g[52]. This could indicate that the particle size could decrease the value, or the layer of non-magnetic TREG on top of the particles. The saturation magnetization found in the study by Maity. D et al.2009[52] was found to be 65 emu/g and hence higher than particles synthesized in the separation optimization batches. This could be due to the extensive centrifugation done in that study which was not done in the thesis. That could lead to a diminishing TREG-layer and hence better saturation magnetization from the particles. Another noticeable difference is that the particles in the separation optimization batches were smaller than for the study by Maity. D et al. which could also give different results. It could be argued that different masses impacted the measurements to some extent, but due to the VSM normalization option it did not seem likely.

To get a better visualization on how superparamagnetic the particles were, the hysteresis loops are shown for the respective separation optimization batches in Figure 5.6.

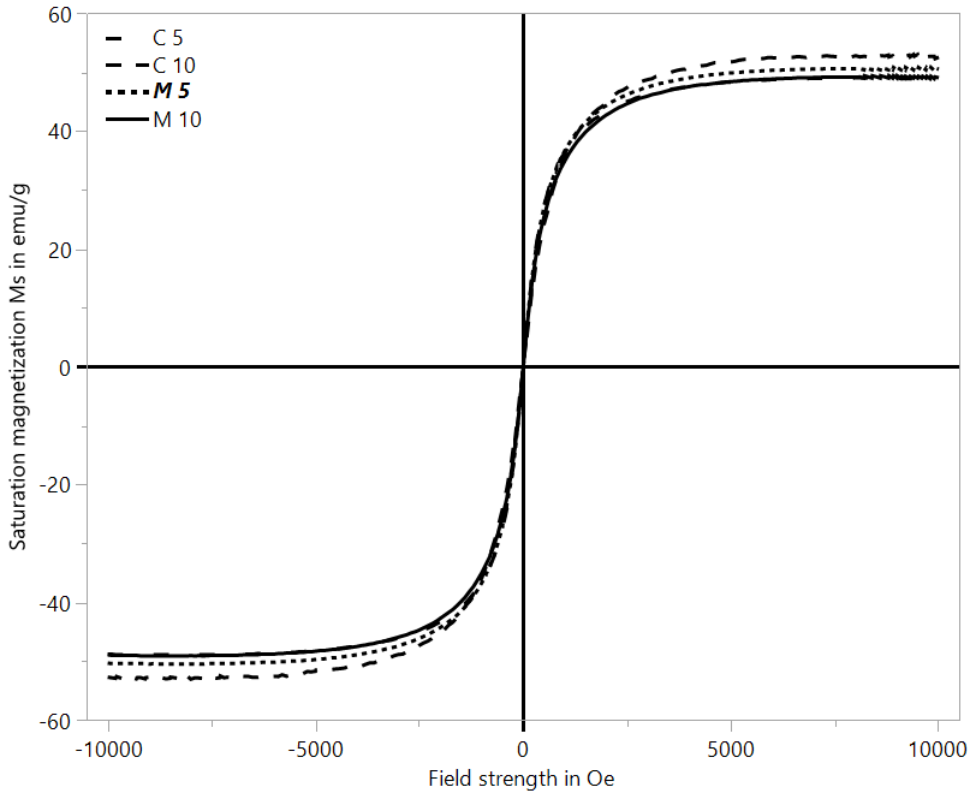

Figure 5.6: Hysteresis loops measured in VSM of iron oxide nanoparticles synthesized in the separation optimization visualizing degree of superparamagnetism.

The hysteresis loops in Figure 5.6 proved that the particles are superparamagnetic by observing no coercivity nor remanence in the curve. This was also observed for the particles synthesized in the study by Maity. D et al.2009[52]. The Figure showed all the respective batches and their hysteresis loops. It was proven that regardless of separation method, the particles seemed to possess superparamagnetic properties.

5.1.5 Summary of Separation technique optimization

Separation studies were conducted with thermal decomposition to find the optimal separation technique. Hydrodynamic sizes gave no apparent trend other than possibly creating smaller sizes in centrifugation due to more removal of TREG layer. The S(T)EM sizes did neither give an apparent trend. It did however indicate that less addition of the anti-solvent *EtAc* would lead to wider particle size distribution, but more batches are needed to prove this trend. For the VSM it was found that all particles displayed superparamagnetic behaviour, but with less saturation magnetization than what is reported in the literature and that of bulk magnetite.

Centrifugation separated particles did not show any observable better particle properties except a small indication of lower hydrodynamic size which is not too important for the following studies. Due to faster separation of particles, magnetic separation was utilized in the remaining work done in the thesis.

5.2 TREG synthesis spherical particles optimization

To further work towards a hyperthermia suited spherical iron oxide nanoparticle, some batch experiments were set up. To attempt to optimize the spheres the following parameters were varied: mass of iron acetylacetonate, volume of TREG and volume ratio of anti-solvent *EtAc* to ethanol. The washing optimization was continued to see if there would be any clear trends when increasing the number of batches. The chemical parameters were varied to observe any possible changes in sizes, saturation magnetization values or specific absorption rate (SAR). As SAR values are correlated towards rapid temperature increase through applying a magnetic field [52] [26] this would prove to be the most important factor towards magnetic hyperthermia.

The different batches followed the study of Maity. D et al.2009 [52], but with magnetic separation instead of centrifugation separation. The starting point was therefore the batch referred to as 2.20 2 in the following TREG optimization study. The batches of the TREG optimization with variations of chemical parameters are shown in Table 5.6.

Table 5.6: Table showing batches respectively synthesized in the TREG optimization by varying the iron acetyl acetonate mass, volume of TREG and washing ratios using EtAc and ethanol.

Batch	Millimoles of iron precursor	Volume of TREG in mL	EtAc:Ethanol ratio
1 (1.20 1)	1 mmol	20	1:1
2 (1.20 2)	1 mmol	20	2:1
3 (2.20 1)	2 mmol	20	1:1
4 (2.20 2)	2 mmol	20	2:1
5 (3.20 1)	3 mmol	20	1:1
6 (3.20 2)	3 mmol	20	2:1
7 (1.30 1)	1 mmol	30	1:1
8 (1.30 2)	1 mmol	30	2:1

Each batch was washed using the same procedure as shown in Figure 4.3 in Methods. The batches were re-dispersed in the same respective volumes of ethanol as the synthesis yield volume for all the 3 washing steps, which means that since synthesis product was always put into two different tubes, the volumes of ethanol would be 10 mL as a constant for all the batches except the 1.30 batch where 15 mL was used. It also means that the washing volume of the respective batches would be 10, 15, 20 and 30 mL of *EtAc* for the 2:1 and 1:1 ratio of anti-solvent to synthesis yield.

When washing the particles, the same problems occurred for the TREG optimization as for the separation optimization. The particles separated leaving a slurry supernatant. The yield was therefore again decreased for each step as the supernatant was disposed of after each washing step.

A possible hypothesis for the TREG optimization particles would be that the particles in batches 1.30 1 and 2 would be larger than the particles of 3.20 1 and 2. The reason for this hypothesis would be that with higher mass of iron precursor one could potentially achieve more nucleation with sufficient supersaturation as stated in the Theory chapter

and hence less growth for each particle, while lower mass would lead to less nucleation and hence more growth. The particles concentration were found to be around 5 mg/mL.

5.2.1 *XRD* of TREG optimization IONPs

The TREG optimization iron oxide nanoparticles were measured in powder x-ray diffraction. The diffraction peaks of batch 2.20 2 (5.16b) which was the starting point and the two extremes 1.30 2 (5.7a), and 3.20 2 (5.7c) are shown in Figure 5.7 .

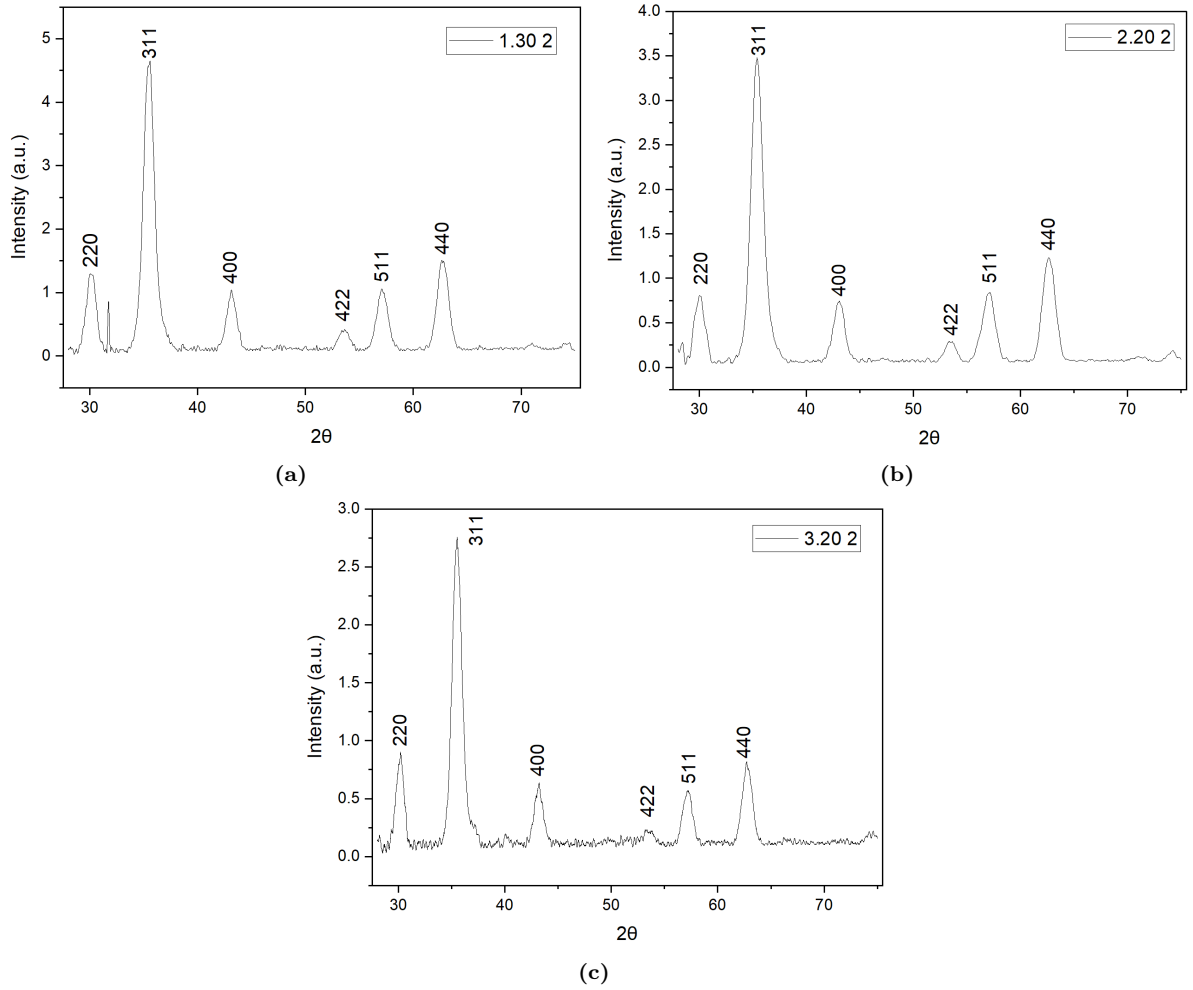

Figure 5.7: Powder x-ray diffraction patterns of batch 1.30 2 (a), batch 2.20 2 (b) and batch 3.20 2 (c).

The XRD peaks between the different batches was compared to see if there was any difference in crystallinity of the different batches of particles. The goal was also to confirm that magnetite and/or maghemite was present as these are the most magnetic iron oxide phases. Phases like hematite are not as magnetic as magnetite[70]. Maghemite is also slightly less magnetic than magnetite, but the problem is that the peaks of magnetite and maghemite are similar and hard to separate when reading the XRD-spectra[71]. Figure 5.16b proved to be quite similar to the Figure of Maity. D et al.2009[52] by having the same peaks with similar crystalline sharpness of the respective peaks. Some differences were observed for the three different batches. One of these differences were the crystalline

intensity of the batches which seems like they decreased by adding more iron precursor. The peaks both became smaller and the 422 plane of the 3.20 2 batch seems to be a lot more different than for the 1.30 2 and 2.20 2 batch. This may indicate that increasing the iron precursor in the experiment batches may have lead to a more amorphous batch of iron oxide nanospheres.

5.2.2 Hydrodynamic size of TREG optimization IONPs

The results of the spherical *TREG* particles and its respective standard deviation through the use of error bars are shown in Figure 5.8 .

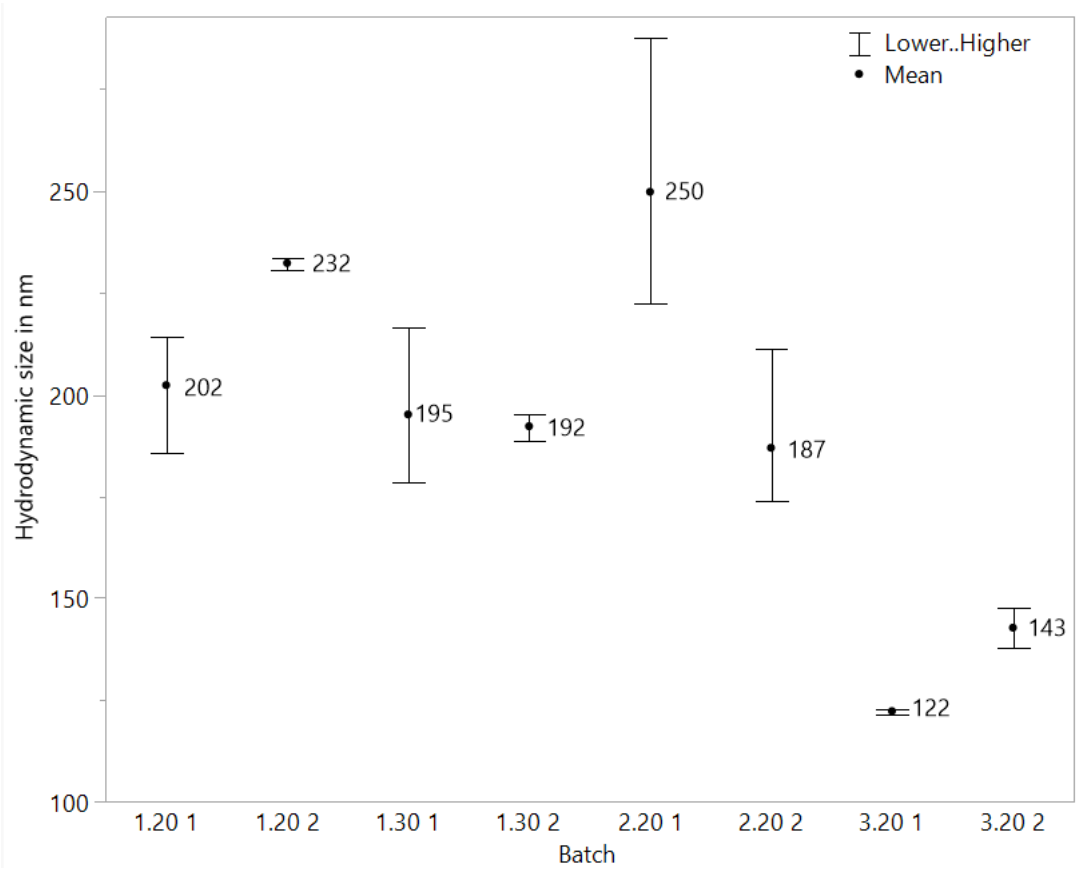

Figure 5.8: Hydrodynamic size of iron oxide nanospheres prepared in the TREG optimization.

The particles were also depicted in a graph showing hydrodynamic particle size distribution. The graph shows the different peaks of the intensity weighted hydrodynamic sizes of the TREG optimization particles in % in Figure 5.9 .

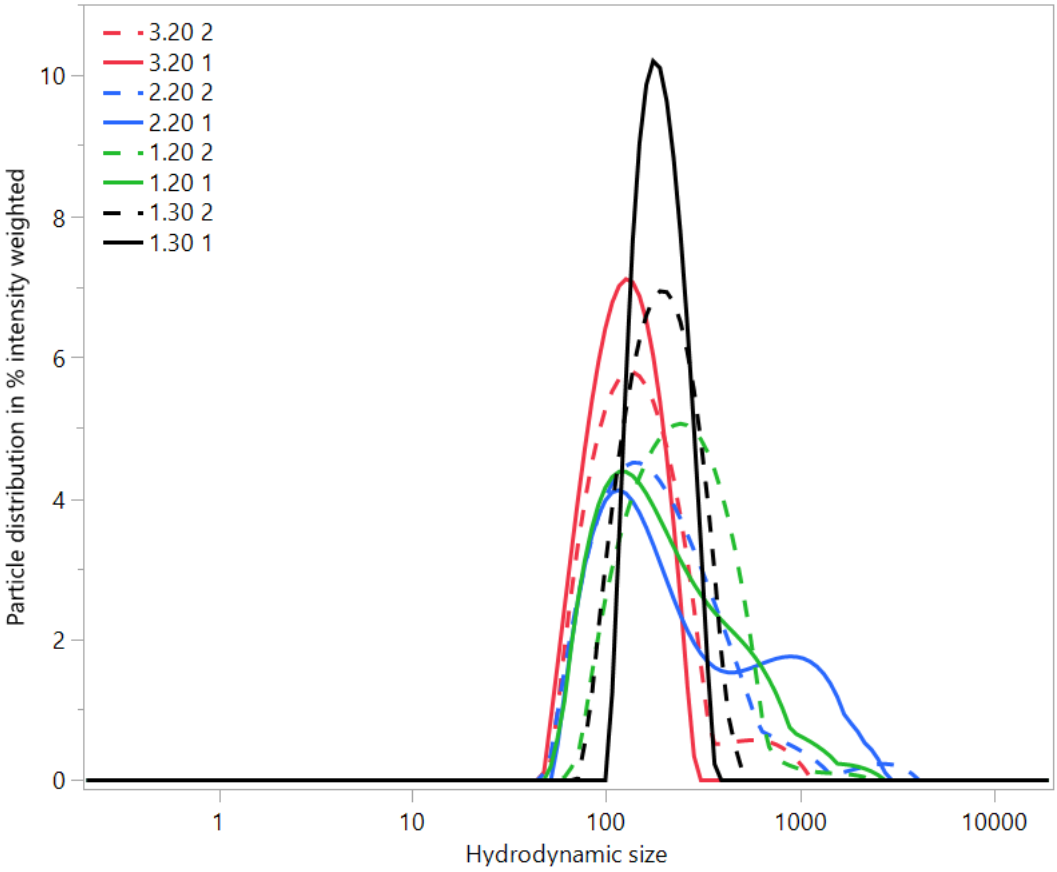

Figure 5.9: Hydrodynamic particle size distribution in % intensity weighted of iron oxide nanospheres prepared in the TREG optimization.

The results from the DLS measurements show that there were some differences in both particle sizes and poydispersity. No apparent trend was observed, but it seemed in general like the particles washed with twice the volume of *EtAc* became more monodisperse. This might not be the case if the particles with the wide peaks are only aggregated and therefore indicates higher degree of poydispersity. The batch with the second most monodisperse particles were the 3.20 1+2 batches. It could be observed both in Figure 5.8 where the standard deviation of the error bars are smaller for the more monodisperse batches and vice versa for the less monodisperse particles.

When compared to the literature, the peaks were compared to the study of Maity. D et al.2009[52] where hydrodynamic sizes of 13 nm were achieved. This was different from the measurements done in the TREG optimization. The particles in this thesis were measured using intensity weighted measurements. In the literature it did not state which measurement method was used, but it could be the same but with more particle preparation. It is stated that they used a Zetasizer instead of Anton Paar Litesizer 500 which was the case for this thesis work. Other differences from the study by Maity. D et al. was that some samples did not display uniform peaks which was reported. Again this is probably due to aggregation within the particles.

5.2.3 *S(T)EM* measurements of TREG optimization IONPs

The particles were imaged to see how they would look in the Hitachi SU9000 S(T)EM. 500 particles were then measured in ImageJ before retrieving data on each respective batch of particles. A picture of each TREG optimization batch is shown to display differences in the particles sizes and morphologies in Figure 5.10.

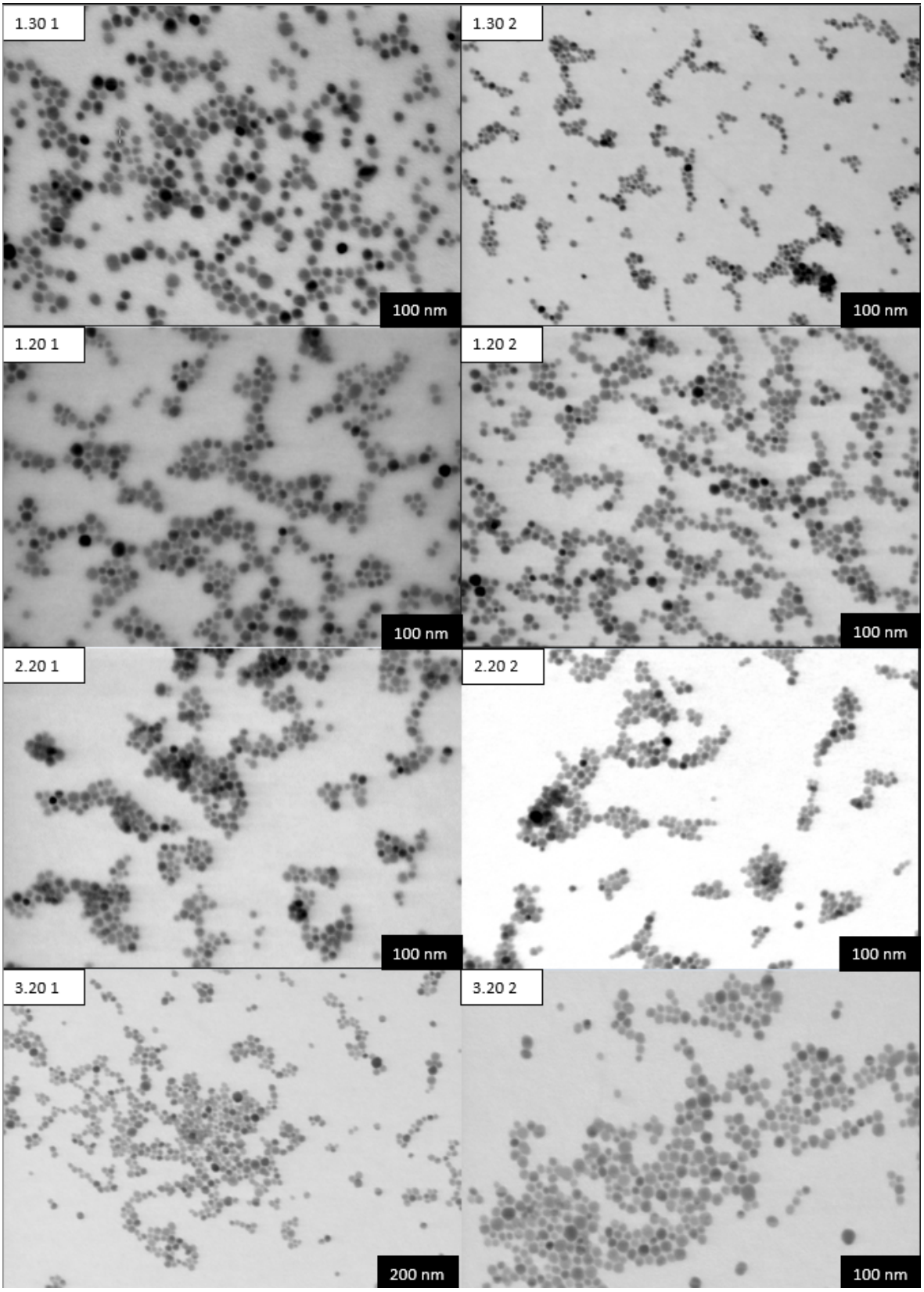

Figure 5.10: Images of all the different particles synthesized in the TREG optimization in scales of 100-200 nanometer.

The pictures of the nanoparticles indicated that there was little difference in the size range between the different batches and that all the particle batches seemed monodisperse. Observing an immediate difference between the particle batches is not possible, so ImageJ is a great tool to use and measure particles. No particles displayed any apparent difference in morphology despite the different chemical parameters used as well as washing volumes. Other than that, some batches looked more aggregated than others but is again hard to observe and has to be plotted into data. In terms of aggregation there were indications of differences in repulsion forces. It seemed like the batches that had been washed with 2:1 ratio of *EtAc*:ethanol were more distant and created smaller aggregates than that of the 1:1 ratio. The study done by Maity. D et al.2009[52] showed a similar of the particles at the scalebar of 100 nm.

The resulting data from ImageJ by pictures taken in scanning transmission electron microscopy are shown respectively for each batch of experiments with respective standard deviations in Table 5.7.

Table 5.7: Table showing sizes and poydispersity derived from S(T)EM for TREG optimization iron oxide nanospheres.

Batch	poydispersity in %	S(T)EM diameter in nm
1.20 1	6.3	5 ± 1
1.20 2	8.1	8 ± 2
2.20 1	2.5	8 ± 1
2.20 2	7.9	7 ± 2
3.20 1	3.2	6 ± 1
3.20 2	3.6	8 ± 2
1.30 1	5.6	8 ± 2
1.30 2	5.7	11 ± 3

The results of the particle sizes were also displayed in an image with standard deviations to see how close the particles would overlap and in that case possibly notice a trend. The image of particles with belonging standard deviations is shown in Figure 5.11.

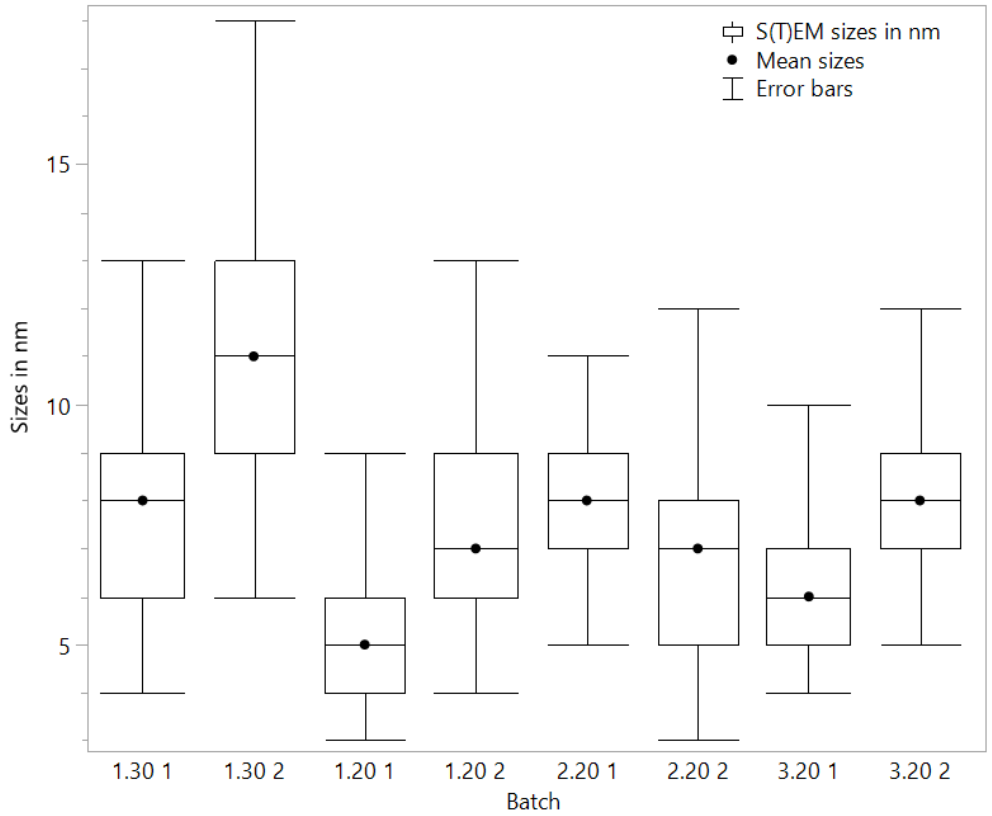

Figure 5.11: S(T)EM size comparisons of different nanospheres in TREG optimization batches with belonging standard deviation.

Figure 5.11 shows that all particles overlap with each other This means that there again was no apparent trend within the different batches synthesized. When compared to the literature, the particles again seemed to be smaller as the study of Maity. D et al.2009 [52] reported sizes of particles in S(T)EM at 11 nm. Only the particle batch of 1.30 2 lie within the same range as the particles in the study. No standard deviation nor poydispersity was mentioned in the study.

The particle size distributions of the S(T)EM measurements were also plotted to get an overview of the particle size peaks of each respective particle batch. This is shown in Figure 5.12.

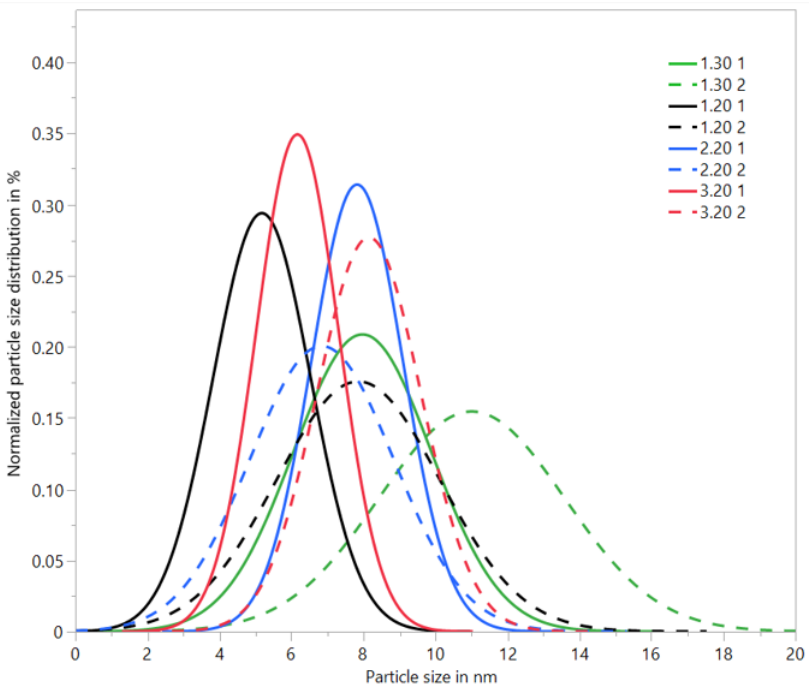

Figure 5.12: Particle size distribution of TREG optimization particles measured in % where 1.0 = 100% for each batch respectively

Figure 5.12 shows the different S(T)EM peaks of the respective batches in the TREG optimization. It seems that the particles with the highest degree of monodispersity was the 1:1 ratio washed particles. The peaks were wider for the particles washed with the 2:1 ratio of *EtAc*:ethanol. This also correlates in some extent to Table 5.7 where the standard deviation is the lowest for the 1:1 ratio of particles. The poydispersity is however different as the particles with the lowest calculated poydispersity seemed to be the 1.30 1 + 2 batches. When comparing this to theory it would make sense as the concentration of the iron precursor is lower compared to the reaction media of TREG. The particles would then have a more controlled growth due to less possible nuclei competing for the supersaturation. No peaks were presented by Maity. D et al.2009[52] for comparison with the work in the thesis.

5.2.4 Saturation magnetization of TREG optimization IONPs

The VSM measurements waere done in the Princeton Mag vibrating sample magnetometer. All measurements were done with a field strength of 10000 Oe. The resulting saturation magnetization and masses measured for the respective batch is shown in Table 5.8.

Table 5.8: Table showing mass of particles measured from respective batches and saturation magnetization retrieved from measurements done in the VSM for the TREG optimization.

Batch	Mass of particles in mg	Saturation magnetization M_s in emu/g
1.20 1	16.47	45
1.20 2	2.35	52
2.20 1	21.88	49
2.20 2	15.42	49
3.20 1	7.66	54
3.20 2	6.19	53
1.30 1	6.28	52
1.30 2	5.54	51

To get a better depiction of the superparamagnetism, Figure 5.13 shows the hysteresis loops for each respective batch of the TREG optimization.

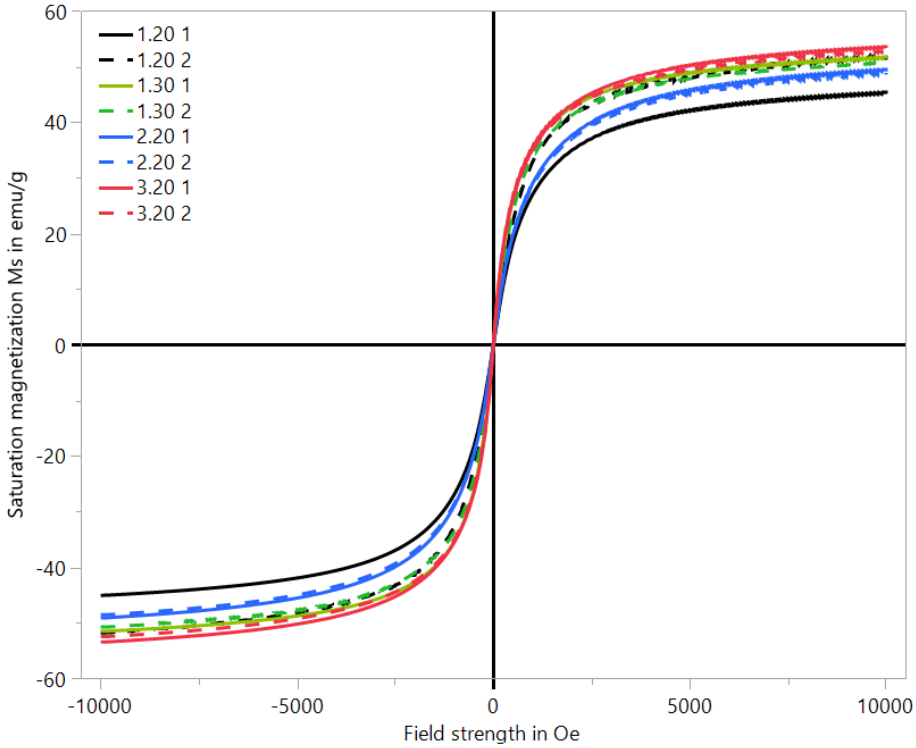

Figure 5.13: Hysteresis loops measured in VSM of iron oxide nanoparticles synthesized in the TREG optimization visualizing degree of superparamagnetism.

Table 5.8 shows the different masses measured and the resulting saturation magnetization. It could be observed that the saturation magnetization for every batch was close to each other. The emu/g values ranged from 45-54 and hence proved all the synthesized particles to be similar. The particles were however far from thee saturation magnetization of bulk magnetite which is 92 emu/g[71]. No apparent trend was observed except that the extreme batches of 1.30 1 + 2 and 3.20 1 + 2 seemed to possess a somewhat higher saturation magnetization. To prove this, more batches would have to be prepared in the extremes with the same synthesis protocol and measurement methods. In terms of the literature,

the extreme batches proved to possess closer values to 65 emu/g which was reported in the study by Maity. D et al.2009[52]. Figure 5.13 shows the hysteresis loops of the different batches. The particles of the TREG optimization displayed the same properties as in the separation optimization where there was zero coercivity and remanence in the particles as well as the saturation magnetization flawlessly crossing the point of zero. The particles as compared again to the particles in the study of Maity. D et al. therefore showed superparamagnetic behaviour.

5.2.5 Heating efficiency of TREG optimization iron oxide nanospheres in Magnetherm

All particles were measured in the magnetherm for 10 minutes at different field strengths and field frequencies. The particles was checked to see how efficient they would generate heat from produced energy by oscillation from the presence of an AMF. The SAR values were then derived from the instrument using the equation in the Theory section referred to as equation 2.15. The results from the TREG optimization respective batches is presented in Table 5.9.

Table 5.9: Table showing retrieved specific absorption rate with set concentration for all TREG optimization batches using an 18 coil, 88 nF capacitor and a field strength of 21 mT which correlates to 5 times Brezovich limit where the frequency is 154 kHz

Batch	mg/mL concentration of particles	SAR values in W/g
1.20 1	0.5	26.6
1.20 2	0.5	45.0
2.20 1	0.5	46.6
2.20 2	0.5	26.7
3.20 1	0.5	0
3.20 2	0.5	61.6
1.30 1	0.5	52.5
1.30 2	0.5	80

The reason for testing at these conditions was that a new limit equivalent to the Brezovich limit were proven to be applicable due to no proof of discomfort at these frequencies. The new limit is suggested to be 10 times the Brezovich limit as new research done by multiple researchers like for instance De La Parte. B.H et al.[72] that deems the new limit efficient for applications *in vivo*. These measurements were conducted using 5 times the frequency limit of the Brezovich. The temperature increase for the respective TREG optimization batches is shown in Figure 5.14.

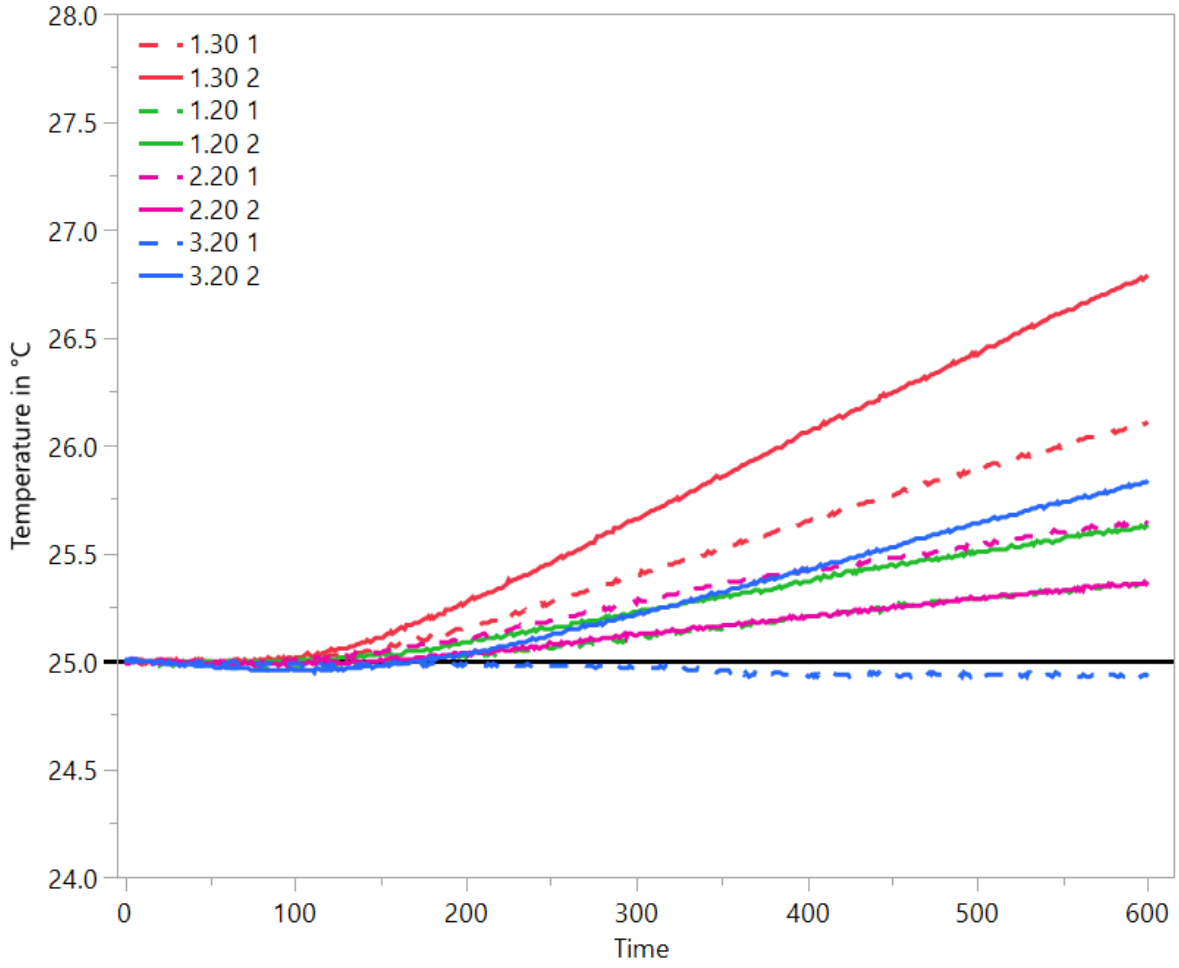

Figure 5.14: 5 times Brezovich limit measurements of TREG optmization particles abilities to generate heat in the presence of an AMF where heating rate is shown in ℃ per second.

What can immediately be observed in Figure 5.14 is that SAR values in the particles correlate directly to the slope of temperature change. In the Figure this is proven by the fact that batch 1.30 2 had the highest SAR value and the steepest slope of all the batches. It was also noticed that sample 3.20 2 had a higher SAR value than 1.30 1 even if it seems that the temperature change is faster in 1.30 1. If one looks closely, one can observe that the particles of 3.20 2 do not start to produce heat until after a while. This may be due to the instrument itself or the internal start temperature of the particle dispersion media. The slope is steeper for 3.20 2 than for 1.30 2, hence higher SAR. The temperature increase for all batches except 3.20 1 ranged from 0.036 ℃ to 0.179 ℃ per minute.

These values could possibly increase by varying the AMF settings. The parameters were therefore maxed out to see how effectively the particles potentially could produce heat. The instrument could reach a radiation equal to 18 times that of the Brezovich limit. One would therefore typically expect a higher rate of temperature increase for higher settings as well as SAR values. The two best particles from the last temperature increase measurement were therefore tested at the same settings, but now the same batches were also tested at the settings producing 18 times the Brezovich limit. The temperature increase rate is shown in Figure 5.15.

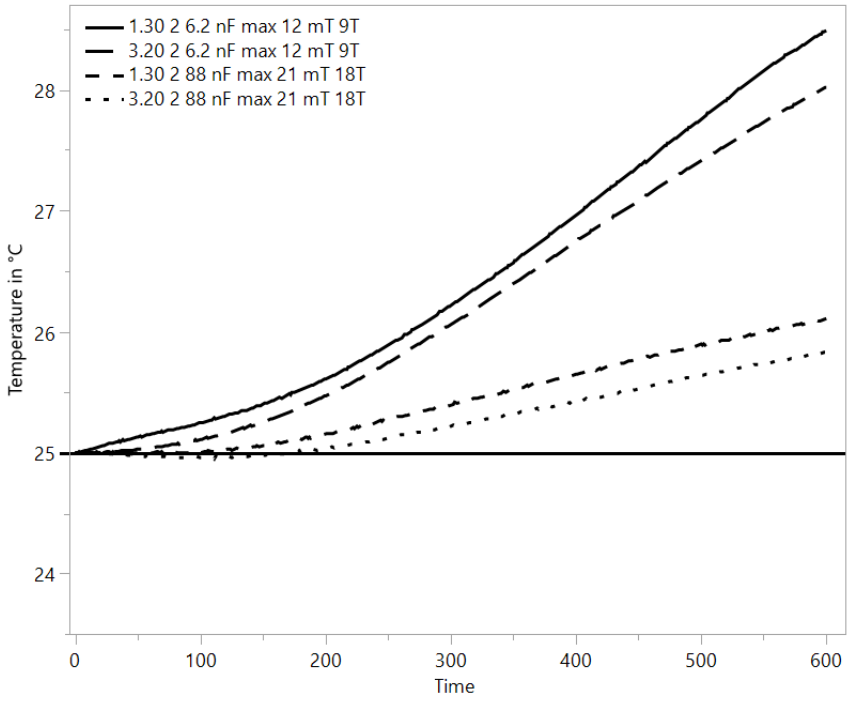

Figure 5.15: 5 times and 18 times the Brezovich limit measurements of TREG optmization particles abilities to generate heat in the presence of an AMF where heating rate is shown in ℃ per second.

As predicted, in Figure 5.15 the slopes of the 18 times Brezovich options were steeper than the measurements done at 5 times the Brezovich limit. The respective SAR-values also increased respectively for 1.30 2 from 80 to 253.8 and for 3.20 2 from 61.6 to 221.5. For *in vivo* applications this would not be allowed and one should therefore stay within the borders of the 10 times Brezovich limit. It was observed in the literature from the

study of Maity. D et al. 2009[52] that particles would reach up to 885 using a 20 MHz frequency which is about 20 times higher than what was used as the maximum limit in Figure 5.15 for the thesis work. Needless to say, the higher frequency would give higher SAR values and the particles in the thesis work could potentially reached around the same range if the instrument would allow the same settings.

This means that instead of changing the AMF settings, one could improve the particle properties by for instance changing morphology to try to achieve higher SAR values and temperature increase to achieve a more effective hyperthermia.

5.3 Summary of iron oxide nanospheres

Iron oxide nanospheres were synthesized as presented in the study of Maity. D et al.2009[52]. The chemical parameters and washing volumes were varied to optimize the nanospheres to their maximum magnetic properties in terms of saturation magnetization and specific absorption rate. Both size and SAR value are two important parameters which needs optimization to achieve the most efficient hyperthermia possible.

The hydrodynamic size measurements showed that the smallest particles were found at batches 3.20 1 + 2. This strengthens the hypothesis of smaller sizes at higher mass of iron precursor. It was also found a trend that indicated the monodispersity increased by the 2:1 washing volume ratio compared to 1:1. This trend switched in the S(T)EM "dry" sizes where the lower washing volume ratio indicated more monodisperse samples. This also proved the importance of measuring both sizes.

For the saturation magnetization, there was little to no difference in terms of the different particles except that it seemed like that the extreme batches of 1.30 1 + 2 and 3.20 1 + 2 gave a bit higher values. This could be due to the TREG interaction on top of the particles. Finally in the magnetherm it seemed like there was no apparent trend. 1.30 2 displayed the best heating properties, which could be explained either by being bigger particles or it would contradict the principles of Lahiri. B.B et al.[73] which states that the monodispersity is an important factor for the hyperthermia effect. The reason this would be out of the ordinary was that batch 1.30 2 displayed the least monodisperse "dry" sizes and hence it should not have given the best heating rate.

The frequency was attempted maxed out at the end to display what would not be within the new acceptable AMF range. It was proven that the heating efficiency increased a lot using non-applicable values at the instruments max capacity. To further improve the hyperthermia effect one would therefore have to stick with the same *in vivo* applicable frequencies, but change the particles morphology or size.

5.4 Iron oxide nanoclusters (IONCs) using TREG and TREA

Iron oxide nanoclusters were prepared as stated in the 4:1 TREA:TREG study conducted by Maity. D et al. 2011[26] to see if the magnetic properties and SAR-values would increase as a function of changing the morphology of the particles. The nanocluster synthesis parameters and batch names are displayed in Table 5.10.

Table 5.10: Table showing iron oxide nanoclusters being synthesized by a specific iron acetyl acetonate mass, Volume of the mix between TREG and TREA and ratio between respectively TREA and TREG.

Batch	Moles of iron precursor	Volume of Mix in mL	TREA to TREG
Nanoclusters 1	2 mmol	20	4:1
Nanoclusters 2	2 mmol	20	4:1
Nanoclusters 3	2 mmol	20	4:1
Nanoclusters 4	2 mmol	20	4:1
Nanoclusters 5	2 mmol	20	4:1

The particles were again washed with the same technique as stated in 4.3. The only difference for the clusters was that they were washed only with the 2:1 ratio. The yield was also better as the concentration ended up at around 3-5 mg/mL depending on the batch of particles. The clusters separated a lot faster than the former iron oxide nanospheres and the supernatant was always almost completely blank after separating with a magnet. The same problem of particles dispersing better in water also occurred for this process, but the particles were still easily observed retracting towards the magnet when applying it. The particles would also separate using a magnet after finally being dispersed in water and leaving a clear supernatant as opposed to the spheres. Another important occurrence was that the synthesis protocol of Nanoclusters 1 differed a bit from the rest as cooling temperature was decreased, balloon was removed and stirring rate was decreased for Nanoclusters 2-5 due to more satisfactory magnetic results. This could indicate some differences in the particles. There also were some challenges in the temperature fluctuation which was improved after changing the old synthesis. All following qualitative measurements were therefore done with Nanoclusters 2 and Nanoclusters 5 to display clusters with the actual properties.

5.4.1 *XRD* of IONCs

Nanoclusters were tested in XRD to see if the particles would give the same signals as the spheres in terms of crystalline and if the particles displayed the same plane signals. The XRD peaks of Nanoclusters are shown in Figure 5.16a together with the 2.20 2 batch Figure 5.16b of the spheres for comparison.

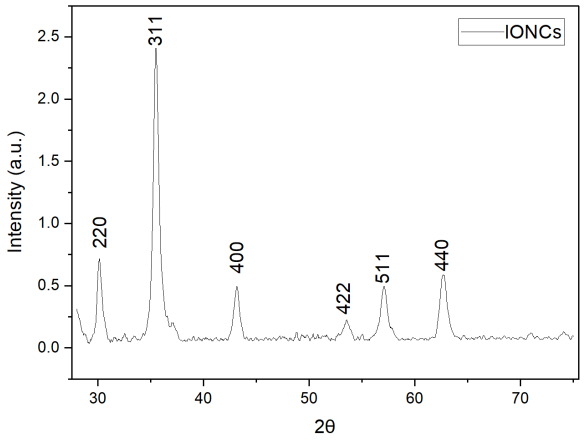

(a) Powder x-ray diffraction patterns of iron oxide nanoclusters (IONCs).

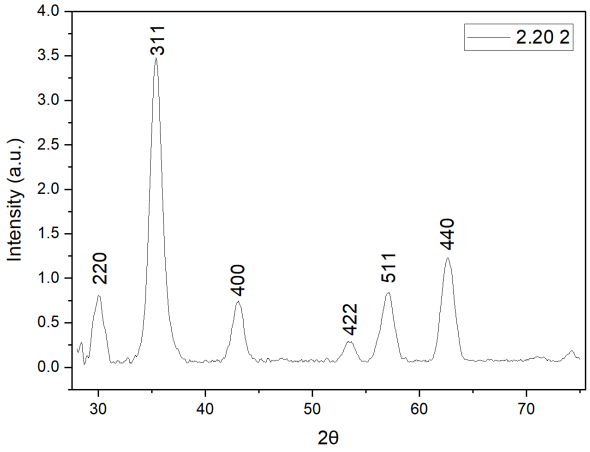

(b) Powder x-ray diffraction patterns of batch 2.20 2.

Figures 5.16a and 5.16b showed that the peaks of the nanoclusters were similar to the reference point of 2.20 2 and hence the spectra measured in the studies of Maity. D et al.2009[52]. One thing to remember is that the particles still could contain maghemite which also could impact the particles magnetic properties. The nanocluster peak also proved to be similar to the study done by Maity. D et al.2011[26]. The peaks seemed to be sharper than that of the nanospheres but also less intense. It would therefore be difficult to compare the crystalline properties between the different particles. This could be done with a proper software for analyzing the peaks. The last observation done was that the relative intensity between background and intensity peaks made it look like there was less organic substance surrounding the particles in batch 2.20 2 than for the nanoclusters.

5.4.2 *FTIR* of IONCs

Particles were measured in Fourier Transform Infrared to identify the organic groups as well as the iron oxide bond. The FTIR spectra is shown in Figure 5.17.

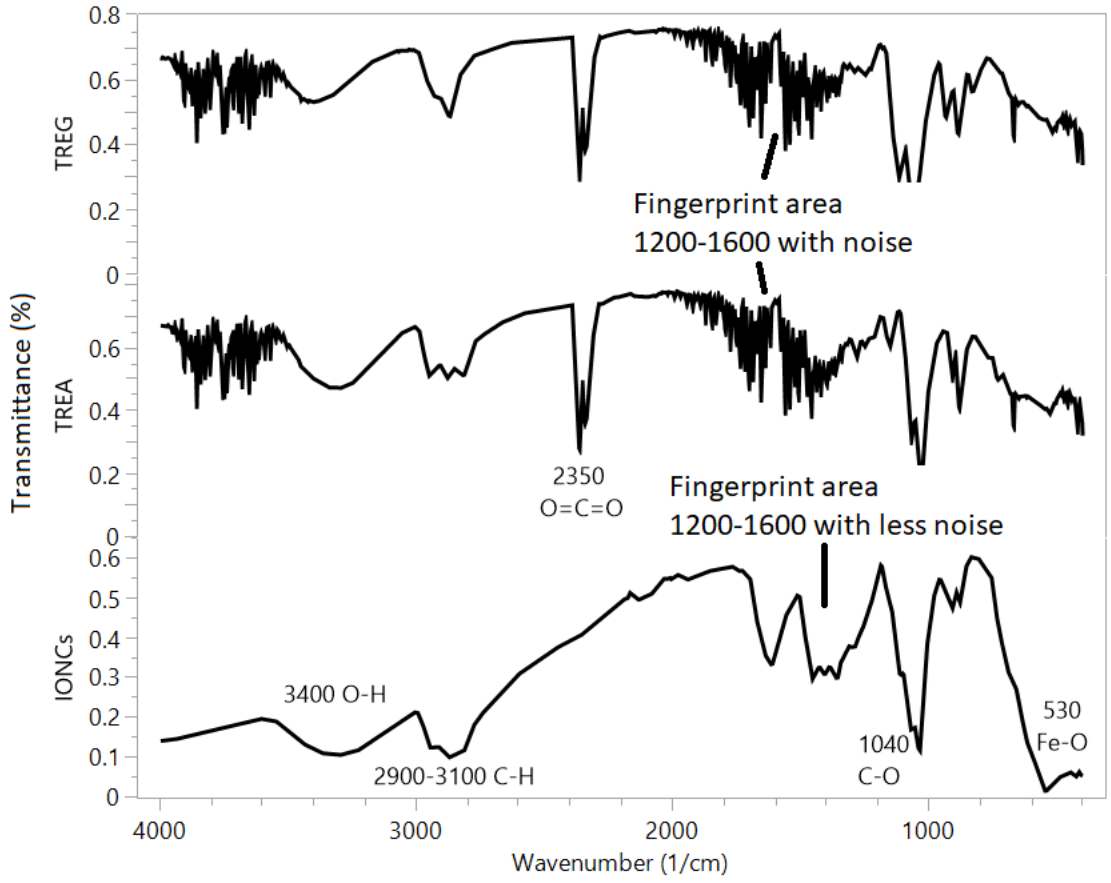

Figure 5.17: FTIR comparison of iron oxide nanoclusters to the solvents TREG and TREA.

Figure 5.17 shows that there are some correlations between the IONCs and the different synthesis solvents. What could be observed was that for both solvents done in normal conditions, the CO_2 peak came at 2350 cm^{-1} which is proof the measurements were not done in vacuum. The Fe-O peak also appeared at around 530 cm^{-1} for the IONCs which was expected. The C-O stretch at around 1040 cm^{-1} as shown in both TREG and TREA was also present in the IONCs. The signals looking like noise in the fingerprint region of 1200-1600 cm^{-1} did also appear, but as a more clear fingerprint with less noise attached in the IONCs. The most descriptive part towards identifying the reaction mechanism did however show at 2900-3100 cm $^{-1}$ where the typical C-H which are close to O-H stretches are shown. In the TREA, this peak is divided into three different C-H groups due to the structure of the molecule. For TREG this peak is divided into two, which makes sense as there are only two different C-H groups leading to TREGs hydroxyl groups. The final observation from the spectra would therefore be that the IONCs have the C-H group split into two which would indicate that the particles are surrounded by a TREG layer on the surface, which would also indicate that the TREA could be an internal stabilizing agent to decrease the surface energy of the iron oxide nanoparticles and hence form clusters. To prove this additional measurements techniques are required.

In terms of literature, the study of Maity. D et al.2009 [52] analyzed iron oxide nanospheres in the FTIR. The peaks from the thesis work are similar except in the fingerprint region, the C-H groups are different as the clusters have more peaks which could indicate the

peaks of TREA. The O-H at 3400 cm^{-1} and Fe-O at 540-580 cm^{-1} stretch in the thesis work is similar to stretches that was reported in the study of Maity. D et al. The most distinguishable difference is the peak difference close to the O-H at 3400 cm^{-1} where the clusters gave 2 peaks with a smaller third peak instead of two which was observable in the study. This could prove a proper TREA presence in the particles and that the reaction could be better understood.

5.4.3 Possible reaction mechanism

To derive a proper reaction mechanism for the nanoclusters, the TREA had to be researched. A study on silver-oxide nanoparticles done by Jia et al.[74] suggested that the hydroxyl groups played an important role when synthesizing silver nitrate with TREA in terms of reduction potential of the TREA. The TREA is also known to act as a chelating agent[75] and can therefore form clusters which will be shown in the suggested reaction mechanism of the iron oxide nanoclusters. The mechanism suggestion is shown in Figure 5.18.

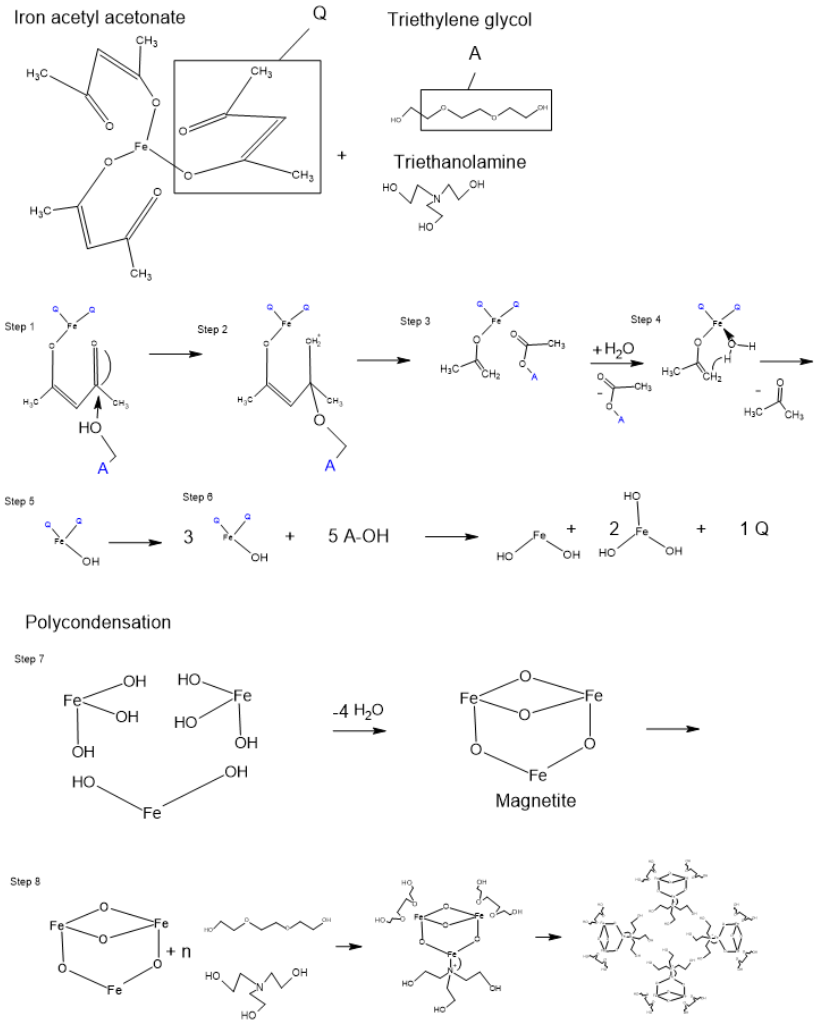

Figure 5.18: Possible reaction mechanism of iron oxide nanoclusters using TREG and TREA as reaction solvents.

Figure 5.18 shows there possibly could be some dipole powers from the hydroxyl groups that create the chelating effect and hence the clusters after the tertiary amine has conducted a nucleophilic attack under more basic conditions or is in general more drawn to the iron. In a study done by Ramirez. C et al.[76] it was suggested that TREA is able to share lone pair of electrons with electrodes like copper which is not to far from iron in alkaline solution, which is why the interaction between TREA and magnetite was suggested when producing the clusters. As opposed to the normal TREG particles which are without nitrogen, the alcoholamines could promote dipole interactions due to the molecule being more polar. This could be a possible reaction mechanism, but needs to be proved through for instance bond strength using RAMAN spectroscopy. The study of Maity. D et al. 2011[26] also suggested that particles aggregate faster under basic conditions when forming nuclei and that the lesser presence of TREG compared to TREA reduces the stabilization from the TREG.

5.4.4 Hydrodynamic size and zeta potential of IONCs

Two different batches of iron oxide nanoclusters were measured by their hydrodynamic size, poydispersity and zeta potential. The results are shown in Table 5.11.

Table 5.11: Table showing hydrodynamic size, zeta potential and poydispersity for Nanoclusters 1 and nanoclusters 5.

[htp]

Batch	poydispersity in %	Hydrodynamic size in nm	Zeta potential in mV
Nanoclusters 1	23 ± 1	120 ± 1	39 ± 1
Nanoclusters 5	18 ± 2	124 ± 3	42 ± 1

The same two particles peaks were displayed to compare hydrodynamic size and peak width for poydispersity. Figure 5.19 shows the peaks of Nanoclusters 1 and Nanoclusters 5.

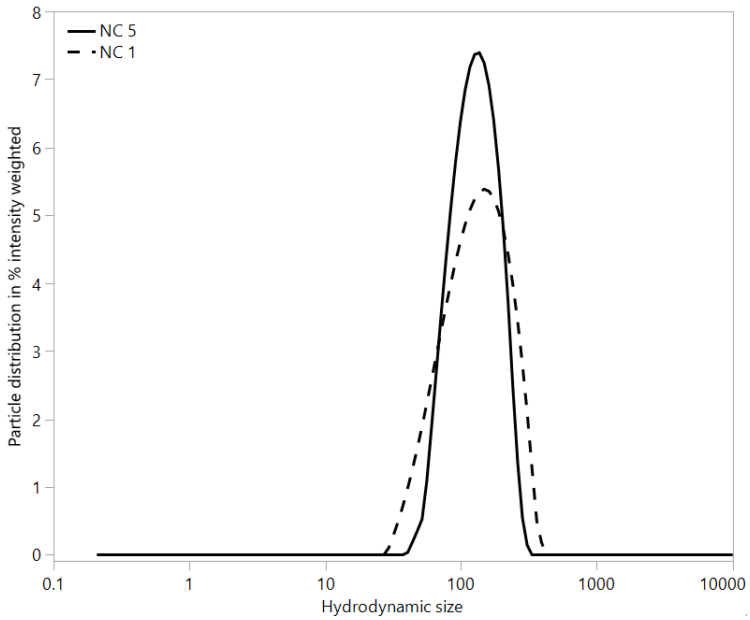

Figure 5.19: Particle size distribution in % intensity weighted of Nanoclusters 1 and Nanoclusters 5.

Figure 5.19 shows the two peaks of the different iron oxide nanoclusters. It was observed that the peaks were a bit different in terms of poydispersity. The sizes did remain almost the same with a minor difference. The nanoclusters did however in general seem to possess a higher degree of monodispersity when measured in the Litesizer. The typical poydispersity of the nanospheres would range from 25-30%, while the clusters would typically range from 18-25%. The sizes were also proven to be smaller than the spheres. The zeta potential was found to be around +40 mV for most of the batches of clusters. In terms of the literature, the study of Maity. D et al.2011 [26] reported sizes of 187 nm which was higher than what was found in the thesis work.

5.4.5 Stability test of IONCs

Iron oxide nanoclusters were tested for their stability as this is an important factor when using the particles for hyperthermia and drug delivery. The curve created after measuring zeta potentials at different pH‘s is depicted in Figure 5.20.

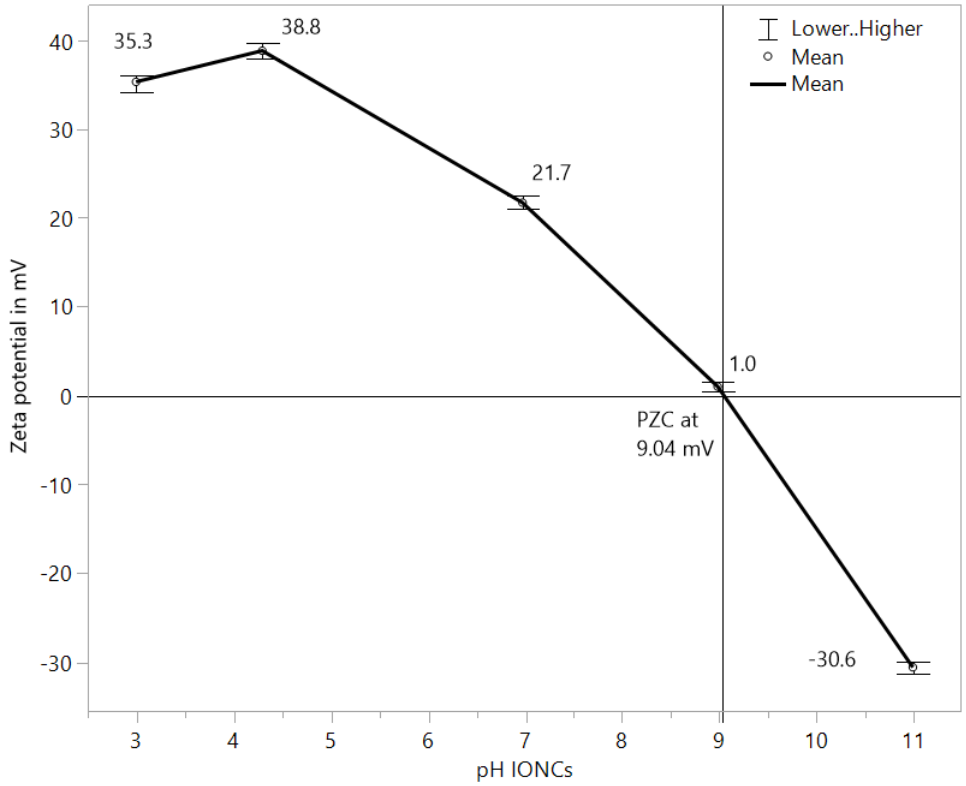

Figure 5.20: Stability test for IONCs by measuring zeta potentials of different pH to creating a zeta curve.

The stability of the particles shows that most particles would stay positively charged until the point of zero charge at 9.04 where most particles do not possess a charge or that the amount of particles with positive and negative charges exist equally. It was observed that from pH 9 to pH 11 the zeta potential dropped at a higher rate than before and that this sudden drop may indicate that the outer surface layer of the particles became rapidly negative from the former pH range. A study by Singh. N et al.[54] showed similar results by creating a zeta curve with iron oxide nanospheres. The PZC was there found at 8.2 whereas the clusters PZC was found at 9.04. the study also showed a rapid decrease from PZC to the zeta potential at the highest measured pH which correlates well with the zeta curve in the thesis.

5.4.6 *S(T)EM* measurements of IONCs

Iron oxide nanoclusters were imaged to find the "dry size" of the particle and if it would be applicable for *in vivo* studies. It is important for the particles to lie within the superparamagnetic range as well as having a satisfactory monodispersity[72]. Two batches of nanoclusters are depicted in Figure 5.21 to see the difference between the particle formations and their sizes.

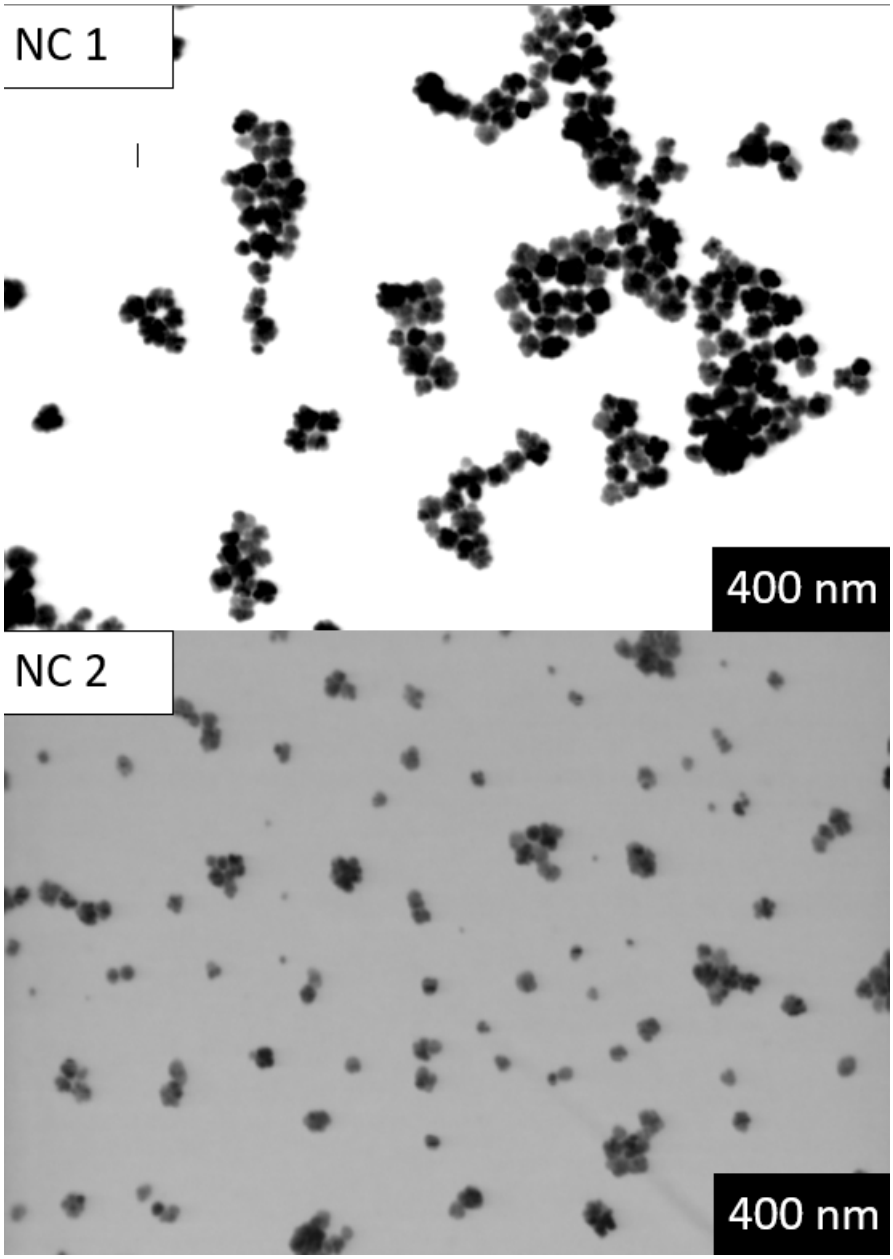

Figure 5.21: S(T)EM images from Nanoclusters 1 and Nanoclusters 2.

Figure 5.21 shows Nanoclusters 1 and Nanoclusters 2. What could be observed in the pictures were that the particles seemed to lie around the same sizes, where Nanoclusters 1 seems to have a bit bigger particles. It was also observed that the particles were more aggregated in the Nanoclusters 1 batch than for Nanoclusters 2. This could be due to better formation of the TREG that stabilizes each particle or cluster. The picture in the study of Maity. D et al.2011 [26] looked similar to the particles from the thesis which proves that the formation of clusters were successful. Maity. D et al. reported sizes of around 44 nm where the method of measurement was not mentioned. In the thesis work, the clusters synthesized was proven to have an average size of around 19 nm. This could also prove different measuring methods of particles as the pictures of the study by Maity. D et al. compared to the sizes in the thesis seem to display the same sizes.

The average size of the clusters was measured as stated in Figure 5.22 .

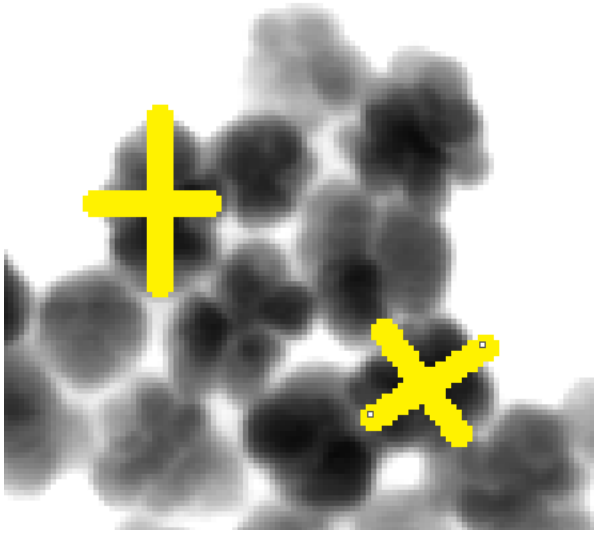

Figure 5.22: Method for measuring sizes in S(T)EM for iron oxide nanoclusters.

Figure 5.22 shows that the clusters were measured using a cross-sectional measuring method. The goal of this was to ensure the best measurement possible in terms of average diameter of the particle. The particles were therefore measured in the most narrow and widest sections to use the average radius of the two sections to determine the final particle diameter. The resulting size after measuring 500 IONCs was found to be 19 ± 7 nm. The reason for this is probably that there are differences in the number of spheres gathering to form one cluster. This means that the monodispersity will be affected. The particle size distribution in numbers is shown in Figure 5.23.

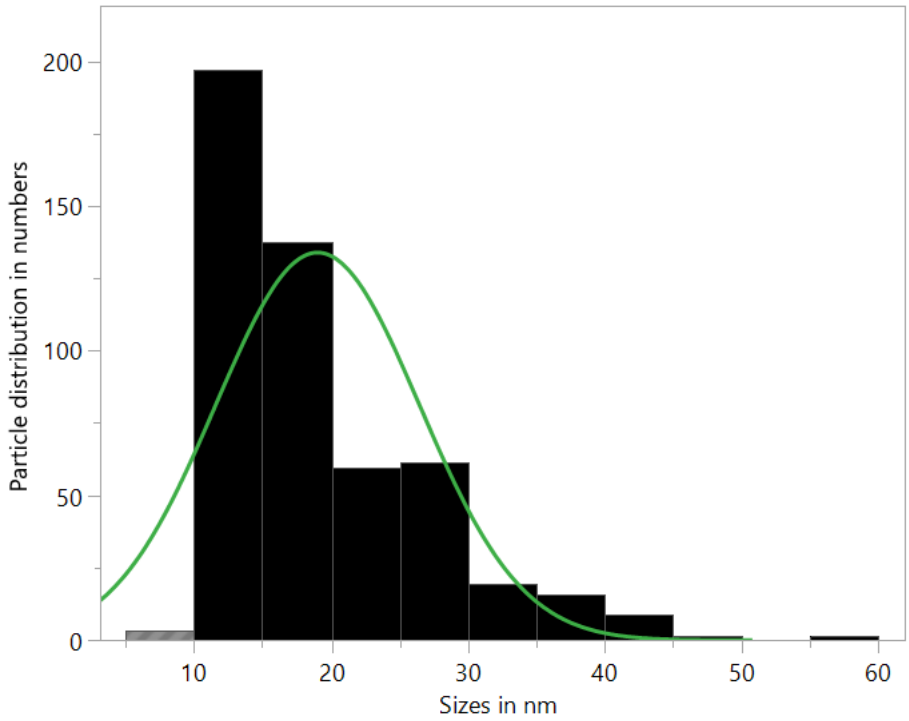

Figure 5.23: Normalized particle size distribution of Nanoclusters 2 in numbers, measured in S(T)EM.

The Figure shows a wide size distribution of IONCs. Most of the particles seemed to lie within 10-20 nm. The particles were measured through cross-section measurements and can therefore be affected by particles with high aspect ratios. The reason for different sizes in S(T)EM might be due to the role the TREA plays in the synthesis of the clusters. If what was suggested by Maity. D et al. 2011 [26] is proven to be true, the clustering of the particles would already have occurred in the basic environment of the nuclei formation and hence create the different clusters with different aspect ratios.

5.4.7 Saturation magnetization of IONCs

Iron oxide nanoclusters were measured at the same settings as the TREG and separation optimization batches to see if the saturation magnetization could be improved from the starting point of the spheres. Saturation magnetization and the respective masses are presented in Table 5.12.

Table 5.12: Table showing mass of nanoclusters measured from respective batches and saturation magnetization retrieved from measurements done in the VSM.

Design of experiment	Mass of particles in mg	Saturation magnetization M_s in emu/g
Nanoclusters 1	24.5	62
Nanoclusters 2	11.5	72
Nanoclusters 5	9.0	71

Table 5.12 shows the differences in the saturation magnetization between the iron oxide nanoclusters. Nanoclusters 1 showed a lower saturation magnetization. This could be due

to the first settings that were changed when synthesizing Nanoclusters 2-5. The earlier temperature fluctuations might have affected the nucleation and growth stage which could impact the saturation magnetization of the particles. Compared to the study from Maity. D et al. 2011[26], the particles saturation magnetization was almost equal as the study reported 75 emu/g.

The hysteresis loops for the clusters compared to the TREG batch with the highest saturation magnetization are shown in Figure 5.24.

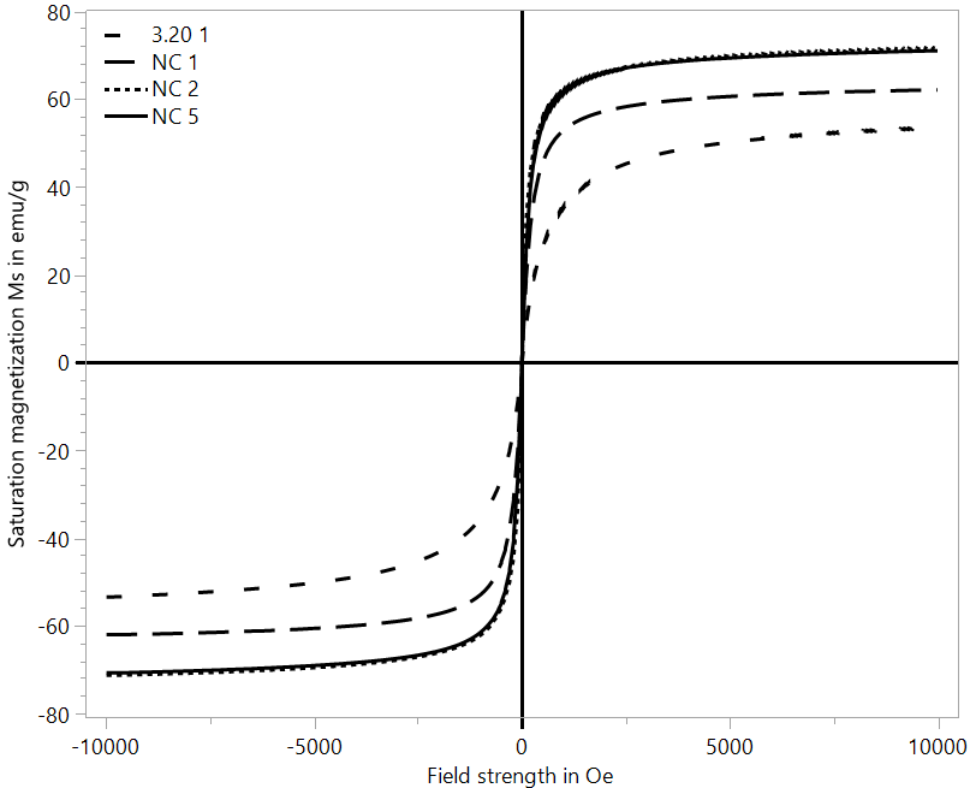

Figure 5.24: Hysteresis loops for iron oxide nanoclusters compared to particle from the TREG optimization with the highest saturation magnetization.

Figure 5.24 showed the different hysteresis loops between the Nanoclusters and the best TREG optimization particle. It was observed that the nanoclusters had a higher saturation magnetization than the best TREG optimization particle and that the clusters still remained superparamagnetic with zero coercivity and remanence. This was also proven in the literature from the study of Maity. D et al.2011[26] where the particles were tested both in 10 kelvin and 300 kelvin. It was proven that one could increase the saturation magnetization of the clusters by applying a higher temperature. In the study, the saturation magnetization increased from 80-90 emu/g. This particular study was however not pursued in the thesis work. In general it seemed like the saturation magnetization of the nanoclusters in the thesis were not too far from the bulk magnetite which has a saturation magnetization of 92 emu/g[71].

5.4.8 Heating efficiency of iron oxide nanoclusters in Magnetherm

Iron oxide nanoclusters were compared to the best batches of TREG optimization iron oxide nanospheres to compare the differences in heating efficiencies. The TREG optimization nanospheres with the highest heating efficiency were therefore compared to Nanoclusters 2 at 5 times the Brezovich limit. The Batches were compared with a concentration of 0.5 mg/mL which was the same for all the former batches. The settings were also again set to 5 times the Brezovich limit. The heating efficiency for the comparison of the iron oxide nanoclusters and the best TREG optimization iron oxide nanospheres is shown in Figure 5.25.

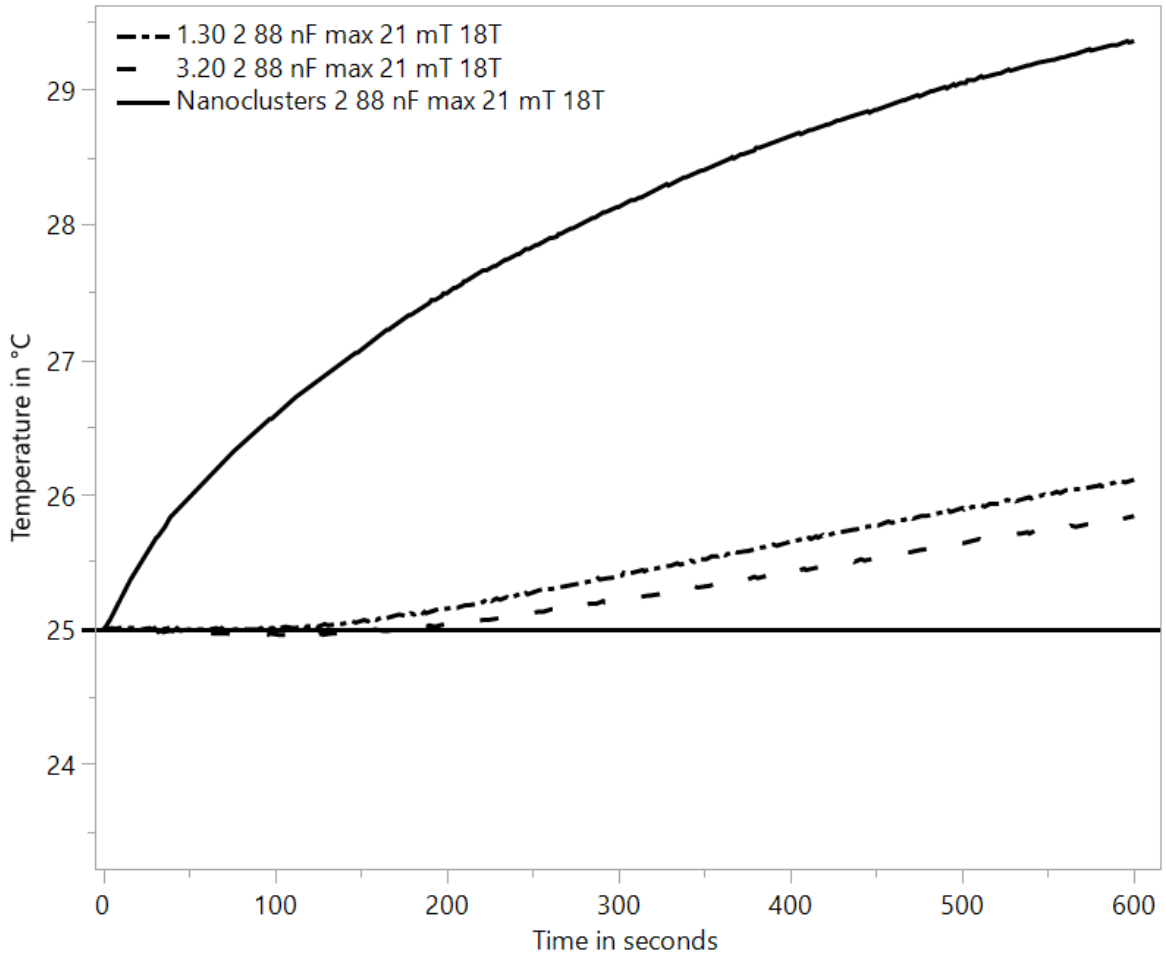

Figure 5.25: 5 times Brezovich limit measurements of nanoclusters vs the best TREG optimization particles in terms of ability to generate heat in the presence of an AMF. Heating rate is shown in ℃ per second.

Figure 5.25 shows the different heating efficeincies of the iron oxide nanoclusters and the best TREG optimization particle batch. It was observed that the iron oxide nanoclusters temperature increased a lot faster than the temperature increase rate of the spheres when being exposed to an electromagnetic field frequency of 153 kHz. Size degree of monodispersity and magnetic properties are the most important factors to increase the heating efficiency of the particles. The hyperthermia efficiency is also directly correlated to the particles ability to efficiently produce heat.

Specific absorption rate, temperature increase rate and concentration is shown in Table 5.13.

Table 5.13: Table showing SAR values and heating rate per minute for the two most heating efficient TREG optimization particles and Nanoclusters 2.

Batch	Concentration (mg/mL)	SAR (w/g)	℃ increase per minute
1.30 2	0.5	80	0.111
3.20 2	0.5	62	0.08
Nanoclusters 2	0.5	303	0.44

The data presented in Table 5.13 shows that the clusters had a higher SAR. The SAR values were almost 4 times higher than that of the best sphere batch. The temperature increase from Figure 5.25 also shows that the temperature increase were far higher than that of the best sphere batch.

After 10 minutes, the temperature increase ΔT per minute for the nanoclusters were 0.436 ℃ vs 0.111 ℃ for the best nanospheres. The measurements were done in "*in vivo* friendly" frequency settings as proposed to the new AMF limit. It therefore makes the nanoclusters an efficient applicable particle in future hyperthermia applications due to it‘s heating properties. The study done by Maity. D et al.2011 [26] showed that SAR values of the clusters was found at 500 w/g. The frequency settings were again a bit higher in the study than in the thesis which could explain the difference in SAR of 200 w/g. The difference in SAR could also to some extent be the difference in monodispersity as it was found to be 12.7% in the study. The monodispersity of the particles are important as it increases the hyperthermia effect which is stated in the Theory chapter from a study done by Parte. B et al. [72].

5.4.9 Summary of iron oxide nanoclusters

It was found that the IONCs possessed better hyperthermia properties than the spheres. It was proven that the clusters had both higher SAR values and a higher saturation magnetization. The hydrodynamic size of the clusters appeared more uniform and reliable than for the spheres as the hydrodynamic particle size distribution peaks were more narrow. The clusters proved to be a bit bigger than the spheres, but still in the superparamagnetic range. The clusters (IONCs) were therefore utilized for further studies in particle coating.

5.5 Polydopamine coated iron oxide nanoclusters(PDCIONCs)

Polydopamine is a commonly used coating technique in biomedical research and is showing promising results in coating for drug delivery[77], intermediate coating techniques[43] and as individual non-coating nanoparticles for other biomedical applications.

For this section, the main focus will be on the intermediate coating technique for further polymerization. This will be important for the final hyperthermia effect by creating more biocompatible nanoparticles that can reach the target site with minimal biological impact.

The particles were polymerized through oxidative polymerization as stated in the Materials section in Figure 4.5 and the parameters for the synthesis is shown in Table 5.14.

Table 5.14: Table showing oxidative polymerization parameters for polymerizing polydopamine on top of iron oxide nanoclusters.

Batch	Mass of IONCs in mg	Mass of DHCl mL	Retraction time in hours
2 H PDCIONCs	6	6	2
4 H PDCIONCs	6	6	4
8 H PDCIONCs	6	6	8
24 H PDCIONCs	6	6	24

Some difficulties were met in this section in the beginning of the study as the tris-buffer was created the wrong way. Some experiments conducted with what was assumed to be polydopamine coating is shown in the appendix and referred to as "assumed dopamine coated IONCs".

5.5.1 *DLS* and zeta potential of PDCIONCs

Iron oxide nanoclusters produced by TREG and TREA were coated with polydopamine through oxidative polymerization at pH 8.5 with a controlled 10 mm tris-buffer as stated by Mrówczyński, R et al.[43]. The particles were retracted at different time-points to see the differences in coating for the respective particle. This procedure was also performed by Lin, LS et al.[50]. The hydrodynamic size as well as zeta potential of the coated nanoclusters are displayed in Figure 5.26a and Figure 5.26b. Nanoclusters 5 was used in the study.

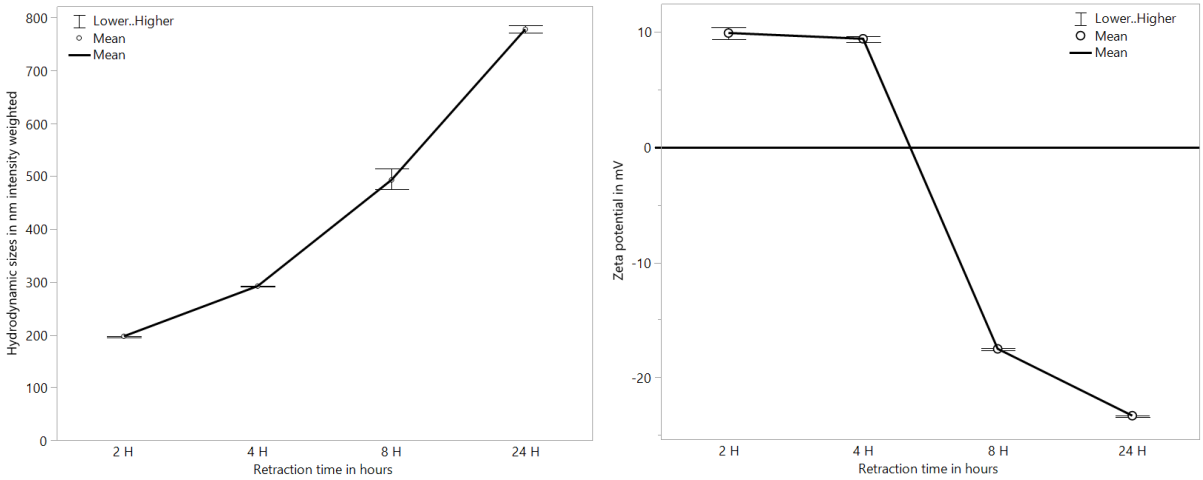

(a) Hydrodynamic size of PDCIONCs after retracting particles at different time points of oxidative polymerization.

(b) Zeta potential of PDCIONCs after retracting particles at different time points of oxidative polymerization.

Figures 5.26a and 5.26b showed that there was a correlation between hydrodynamic size and zeta potential of the polydopamine coated iron oxide nanoclusters. While the hydrodynamic size increased, the zeta potential decreased. The reason for this might be the coating thickness of the polydopamine layer that is increasing by size, but also introduces more negatively charged polydopamine. The reaction was done in a controlled Tris-buffer with a pH of 8.5, so the pH should not have changed too much which indicates that the zeta potential change mainly comes from the Polydopamine. It was also observed that the hydrodynamic size increased respectively while the zeta potential decreased through an increasing amount of time under oxidative polymerization. The hydrodynamic size growth was calculated. The resulting average coating rate of polydopamine was found to be 27 nano meters per hour(nm/h). This kinetic study was conducted from the inspiration of Lin, LS. H et al.[50] who tried the kinetics of growing the polydopamine coating layer. Hemmatpour, H et al.[78] tried adsorbing polydopamine on halloysite nanotubes(HINTS) and did a similar study, but with pure PDNPs. Table 5.15 shows the different growth times at respective time retractions.

Table 5.15: Growth rate per hour of polydopamine shell on IONCs after each retraction time point of PDCIONCs.

Retraction times in hours	Growth rate in nm/h
0-2 H	37
2-4 H	47
4-8 H	50
8-24 H	18

Table 5.15 shows that the coating occurred at a faster rate in the beginning of the oxidative polymerization than at later hours. It seemed like the coating thickness of the PD rose until finally stagnating after 8 hours of polymerization. This may prove that the attractive forces towards pulling the PD species decrease after having a certain layer of polydopamine put on top of the bare IONCs. Compared to the study done by Cheng. C et al.[55] where measurements were done in FE-SEM, it seems like the thickness grows

at a faster rate on the clusters than on the PES surface. When looking at the AFM size measurements done in the same study, it does however seem like the polydopamine has grown at almost the same rate as the AFM sizes were measured at 20-500 nm.

5.5.2 Stability test of PDCIONCs

A stability test was conducted for the polydopamine coated iron oxide nanoclusters to see a possible change for respective pH after coating the IONCs. The batch used for the zeta potential measurements at different pH was the 8 H PDCIONCs. The zeta curve of the polydopamine coated iron oxide nanoclusters in comparison to the zeta curve of the bare IONCs is shown in Figure 5.27.

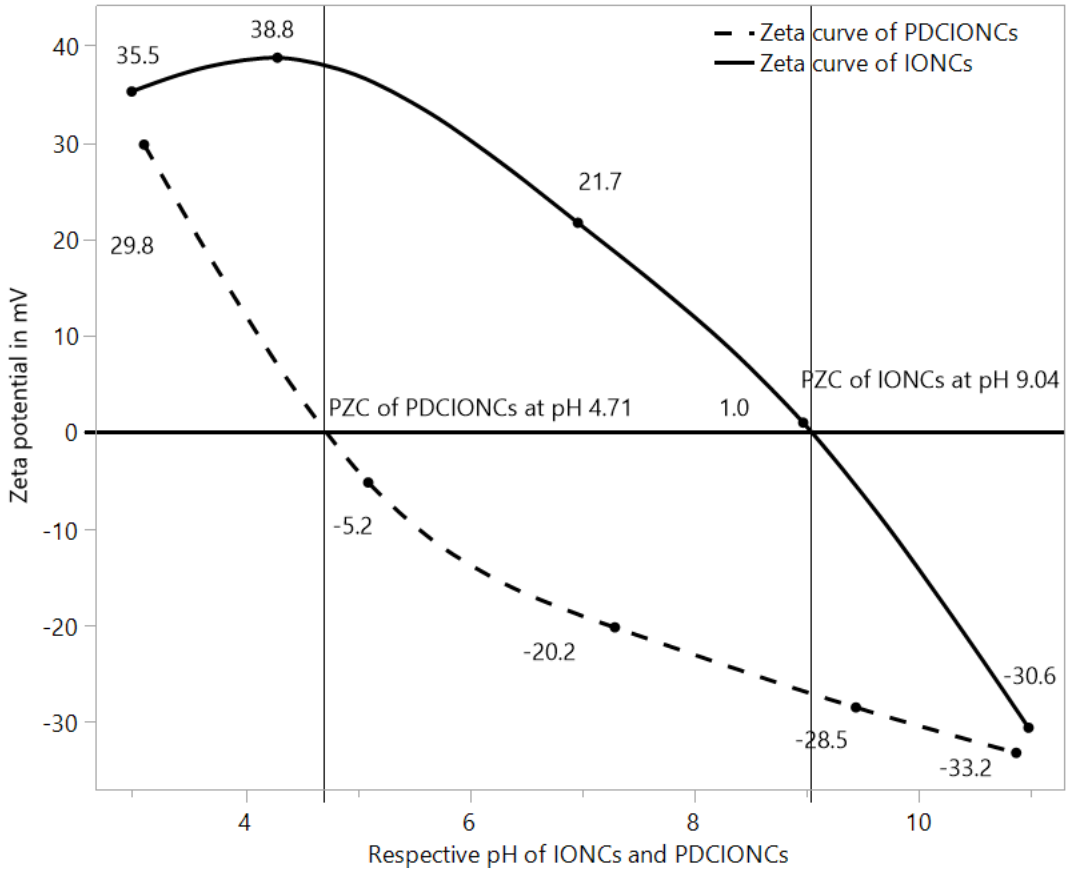

Figure 5.27: Stability test for PDCIONCs with IONCs as reference by measuring zeta potentials of different pH to create a zeta curve.

Figure 5.27 shows that the particles remained stable from pH 3 to about 3.5 and from about pH 7 and up to 11. The reference used for this was zeta potentials of +20 and -20 mV as suggested in the study by Sing. N et al.[54]. The zeta potential for the respective polydopamine coated iron oxide nanocluster also followed a similar curve to the study of Singh et al. where the PZC was given at 4.7. In the thesis the PZC was found to be 4.71 and this correlates really well to the study by Singh. N et al. The last observation made in Figure 5.27 was that there was a major difference in the curve between bare and coated iron oxide nanoclusters, which gave a good indication that the coating of polydopamine on top of IONCs were successful.

5.5.3 *XRD* of PDCIONCs

PDCIONCs were measured in powder x-ray diffraction to see differences in peaks after coating the IONCs with polydopamine. The following XRD peaks of polydopamine coated iron oxide nanoclusters are shown in comparison to the IONCs in Figure 5.28a and Figure 5.28b .

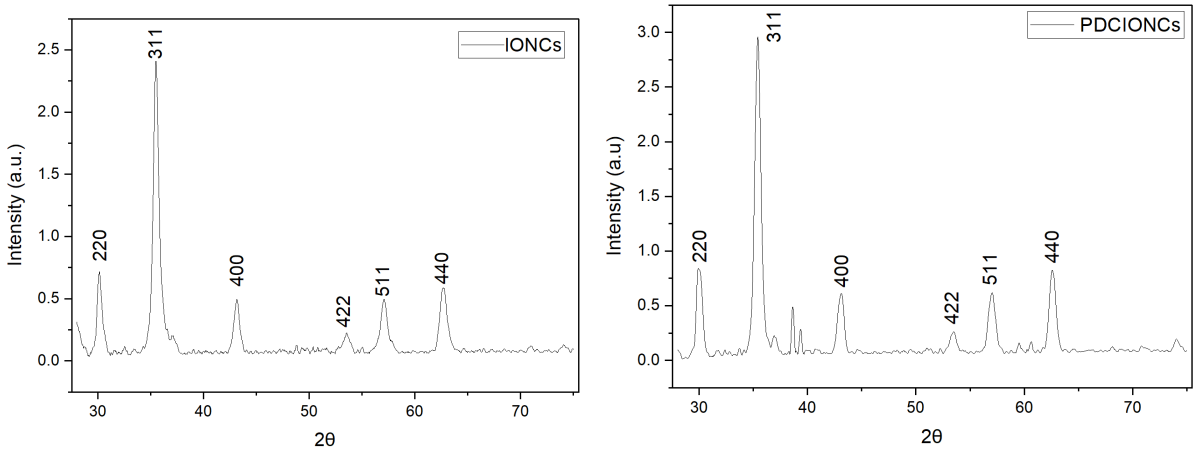

(a) Powder x-ray diffraction patterns of iron oxide nanoclusters (IONCs).

(b) Powder x-ray diffraction patterns of polydopamine coated iron oxide nanoclusters (PDCIONCs).

Figures 5.28a and 5.28b show the x-ray diffraction patterns of of IONCs and PDCIONCs. It seems like after the coating process off polydopamine, the IONCs became more crystalline. This could mean that the dopamine hydrochloride have interacted with the TREG and TREA, or that the excess washing steps with MQ-water after coating might have removed some of the amorphous compounds formerly surrounding the clusters.

The PDCIONCs did display some unfamiliar peaks which had not occurred earlier. This could be noise from the instrument or some impurity in the sample, but it could also be the polydopamine interacting with the particles creating some new peak by impacting the formation of the clusters. The peaks were still proven to show magnetite and/or maghemite presence. The same peaks remained at the same angles after the coating as well. In the study of Singh. N et al.[54] the polydopamine coated iron oxide was also analyzed in powder x-ray diffraction. The patterns looked very similar to what was done in the thesis work. The difference being what seems like sharper peaks in the thesis work, but at a lower intensity. This could also be due to differences in preparation methods between the study and the thesis work.

5.5.4 *FTIR* of PDCIONCs

Polydopamine coated iron oxide nanoclusters were analyzed in the FTIR to see if signals of the polydopamine would differ between the different retraction times. Figures 5.29a, 5.29b and 5.29c show a the local areas of the patterns as well as a full depiction of all the respective polydopamine coated nanoparticles.

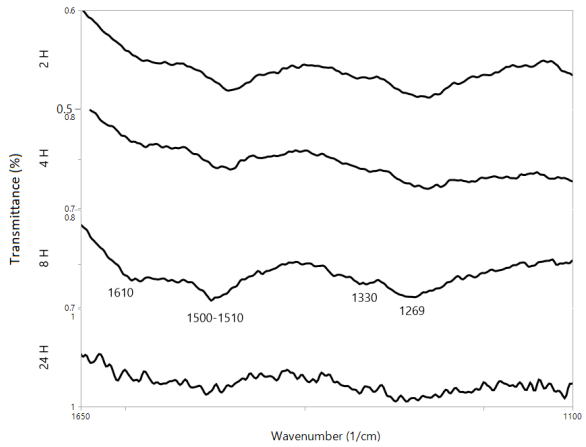

(a) FTIR of fingerprint area of polydopamine coated iron oxide nanoclusters (PDCIONCs) of different retraction times.

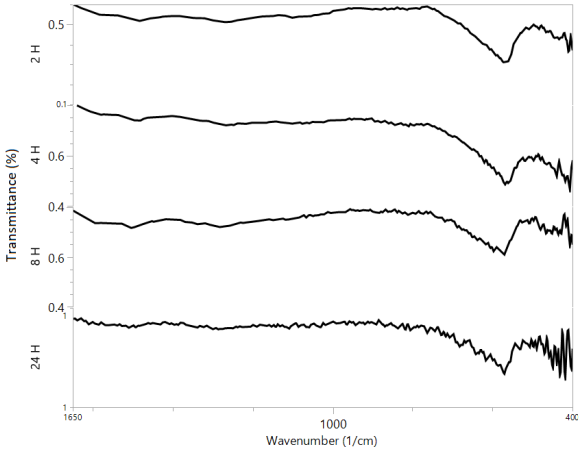

(b) FTIR of iron oxide peaks with smaller scale fingerprint region of polydopamine coated iron oxide nanoclusters (PDCIONCs) at different retraction times.

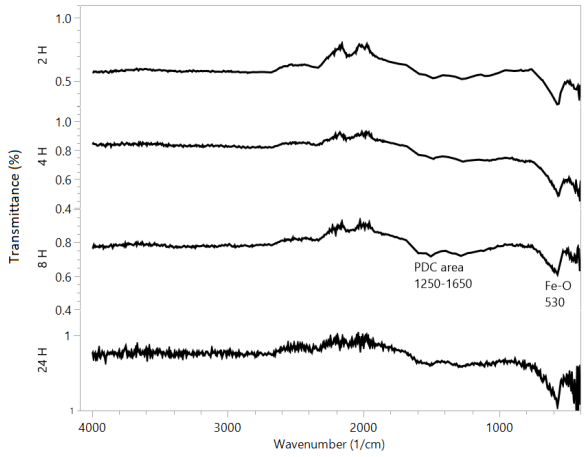

(c) Full FTIR spectra of polydopamine coated iron oxide nanoclusters (PDCIONCs) at different retraction times.

Figure 5.29c shows the full FTIR analysis pattern for polydopamine coated iron oxide nanoclusters at different retraction times. The first observation was that the intensities of the peaks decreased with longer polymerization exposure time.

Figure 5.29a shows that the fingerprint region of 1250-1650 cm^{-1} became more clear through longer polymerization exposure time. This trend was shown for batches from 2-8 hours. For the 24 H, the measurements became more noisy than for the polymerization duration of 2-8 hours , which could indicate that the coating became more disorganised or that the particles started to aggregate more, and hence create more noise and weaker signals.

An observation done in Figure 5.29b was that the Fe-O stretch at 530 cm^{-1} became less and less visible when extending the polymerization exposure time. The combination of less signal in the Fe-O region and the increase of visibility in the fingerprint region of polydopamine also indicates a successful coating of the polydopamine on top of the iron oxide nanoclusters. In the study of Singh et al. 2019 [54] polydopamine coated iron oxide nanospheres were analyzed in the FTIR. The patterns were similar to the thesis work by having the Fe-O bond at 580 cm^{-1} and the fingerprint with the same peaks as displayed

in the thesis at 1200-1650 cm^{-1}. The C-H peak at 2900 cm^{-1} was not visible in the thesis work, which could be due to the different formations of polydopamine on clusters instead of spheres.

5.5.5 *UV-vis* of PDCIONCs

Polydopamine coated iron oxide nanoclusters and bare IONCs were analyzed in the Uv-vis to see if any differences were present in the light absorption of the particles at different wavelengths. Figure 5.30 displays the UV-vis spectra between PDCIONCs and IONCs.

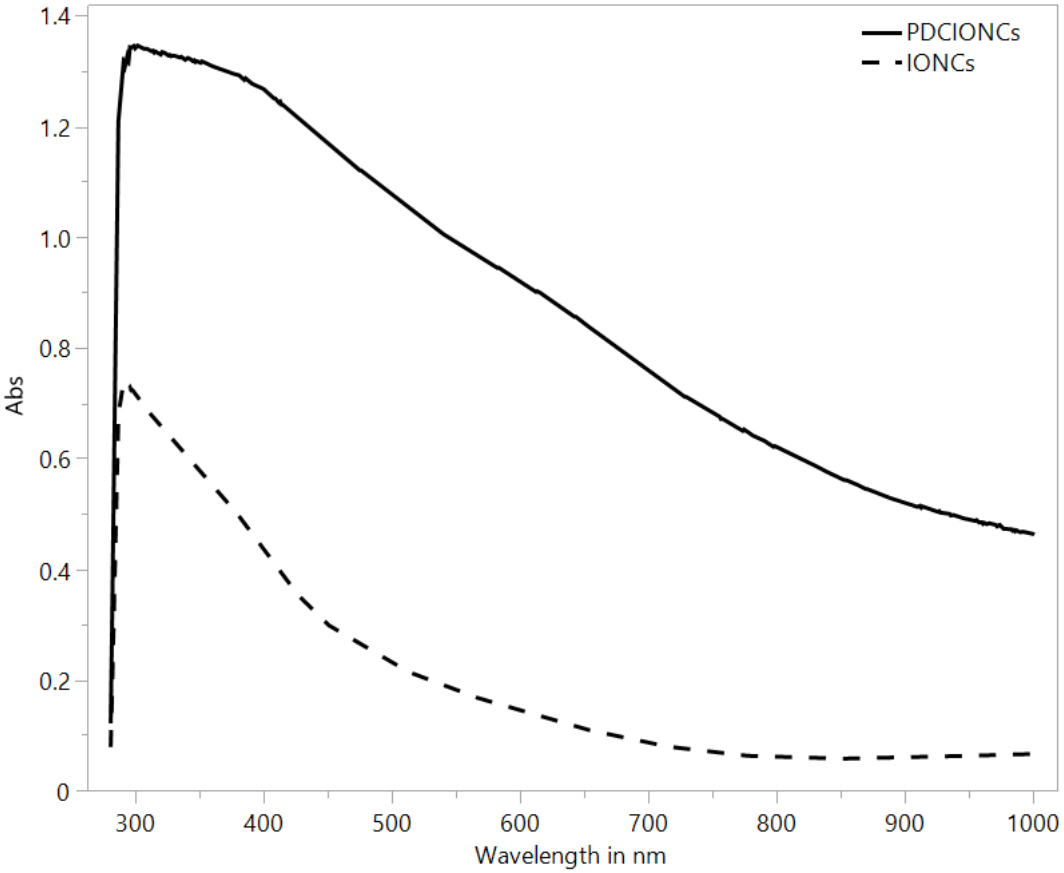

Figure 5.30: UV-vis absorption peaks between (IONCs) and (PDCIONCs.)

Figure 5.30 shows the different peaks of polydopamine coated iron oxide nanoclusters and bare iron oxide nanoclusters. It was observed that there was a reasonable difference between the absorption of the polydopamine coated iron oxide nanoclusters and the bare nanoclusters. The solution was also visibly darker before the measurements and after preparation of the particles, which means that the peak differences between the particles were as predicted. Since both batches were measured at the same concentration, this is a good indication of polydopamine presence on the iron oxide nanoclusters. The peak differences were also shown by Singh, N et al.[54] where it was observed that the peak of the polydopamine coated iron oxide nanospheres were a lot higher at the same concentration for the respective particles.

5.5.6 Summary of polydopamine intermediate coating

Polydopamine was polymerized on top of the iron oxide nanoclusters with the use of oxidative polymerization at pH 8.5. It was proven that the coating thickness could to some extent be controlled depending on the time of retraction from the polymerization as stated in Lin, LS et al.[50]. It was also proven that the rate of coating thickness was more effective in the beginning hours of the oxidative polymerization than later in the process which indicates varying growth kinetics. The analysis done in the FTIR was also confirming differences in coating thickness by having more distinct peaks at higher retraction hours of the particles. The difference in PZC also showed that the particles became different after the polymerization process and therefore most likely successfully coated. UV-vis also proved a formidable change in the absorption between the bare and coated iron oxide nanocluster. For the PLGA work in the thesis, all the different batches were used to see if there would be any difference in size and magnetic properties that could be proven to enhance the hyperthermia effect.

5.6 Poly-lactic-co-glycolic acid coated PDCIONCs (PLGA@PDCIONCs)

PLGA is known to be biocompatible and biodegradable and controllable to some extent in terms of kinetics in drug delivery application. This depends on the formation of the polymer which controls the degradation kinetics[79].PLGA was therefore pursued as a final coating of the PDCIONCs. Due to the penetration properties, PLGA particles can travel to the target site without leaving behind harmful particles in undesired areas in the body as proven in the nanotoxicology field[80] and hence improve selectivity when an AMF is applied.

Poly-lactic-co-glycolic acid was therefore attempted polymerized on top of the PDCIONCs by the method presented by Mohammad. A et al.[60]. The polymerization had to be scaled down from the study done in the literature, due to extensive masses of what would represent the particles in this case. The polymerization of PLGA on top of PDCIONCs was therefore conducted as stated in the Methods section. The different batches polymerized is shown in Table 5.16.

Table 5.16: Table showing different batches from the retraction time study of polydopamine used for polymerizing PLGA on top of (PDCIONCs).

Batch
2 H PLGA@PDCIONCs
4 H PLGA@PDCIONCs
8 H PLGA@PDCIONCs
24 H PLGA@PDCIONCs

The chemical parameters of monomers and initiator used when polymerizing PLGA on top of all batches of PDCIONCs is shown in Table 5.17.

Table 5.17: Chemical parameters for polymerizing PLGA on top of the different batches of (PDCIONCs).

Mass of L-glycolide in mg	Mass of RON-lactide in mg	Volume of stannous octoate in µl
450	900	6

All the polymerized particle batches were retracted after 3 hours of PLGA coating as stated in Mohammad. A et al.[60].

5.6.1 *DLS* and zeta potential of PLGA@PDCIONCs

The PLGA coated PDCIONCs (PLGA@PDCIONCs) were measured to see how big the particles would look in terms of hydrodynamic size between the different batches. The particles hydrodynamic sizes were difficult to measure using light scattering due to the particles not dispersing well in water. The particles were left to precipitate for 10 minutes as a natural filtration process before transferring the supernatant and measuring the sizes of the particles in the supernatant. Some unfiltered samples can be found in the appendix to give an overview of why the particles were hard to measure. The resulting sizes of the

filtered PLGA@PDCIONCs are shown in Table 5.18 with respective poydispersity and zeta potential.

Table 5.18: Different sizes, poydispersity and zeta potential of PLGA coated PDCIONCs (PLGA@PDCIONCs), where 2 H euqals 2 H PLGA@PDCIONCs and 4 H equals 4 H PLGA@PDCIONCs etc.

Batch	Hydrodynamic size (nm)	poydispersity (%)	Zeta potential (mV)
2 H	1622 ± 657	34 ± 7	12 ± 4
4 H	991 ± 330	25 ± 3	-7 ± 1
8 H	848 ± 27	35 ± 18	0 ± 2
24 H	2373 ± 1746	27 ± 2	-12 ± 1

The particle size distribution from the table is shown in Figure 5.31.

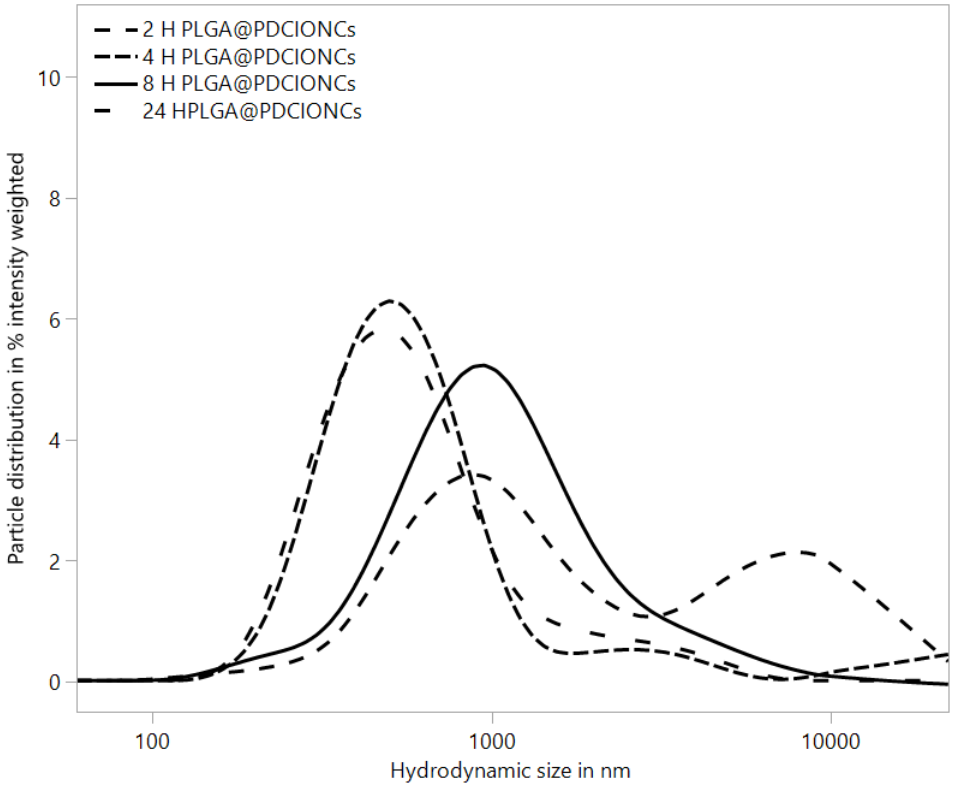

Figure 5.31: Hydrodynamic particle size distribution in % intensity weighted of all (PLGA@PDCIONCs) batches.

Figure 5.31 shows all the batches polymerized of PLGA@PDCIONCs. It was observed that there was no apparent trend in the sizes of the polymerized PLGA on top of the PDCIONCs. It was also seen that the 2 H PLGA@PDCIONCs seemed to have two populations of particles. This could be due to the polydopamine not polymmerizing properly in 2 hours which means that some surfaces could still be dominated by hydroxyls and hence create a different population of particles. The other particle population peak closer to 10000 could also be a proof of aggregation within the particles due to less stability between the surfaces of the potentially less polydopamine coated IONCs.

The three other samples did also prove to have some minor size differences within the samples that could prove multiple populations, but not to the same extent as the 2 H batch where it seemed like the bigger particle sizes consisted of half the total population. A general observable trend was that all the different batches were poly-disperse after the PLGA coating step. The particle size distribution is quite wide and one could find a lot of different sizes within the respective particle batches of coated particles. This could indicate that the polymerization of the particles was not done through grafting, but as bulk polymerization. Zhang. X et al.[57] reported sizes of 300 nm for PLGA coated iron oxide nanoparticles. A possible reason for the particles in the thesis being bigger is that the polymerization was done solvent free and that the clusters could have interacted differently with the polymerization. The different interaction could have been due to the presence of TREA and polydopamine, which is not present in that study.

5.6.2 Stability studies of PLGA@PDCIONCs

A stability test was conducted for the PLGA@PDCIONCs and compared to the PDCIONCs. The zeta potentials were measured and a zeta curve was again created to see if the different particles displayed different behaviours within a pH range of 3-11. Figure 5.32 shows the PLGA@PDCIONCs curve vs the PDCIONCs curve.

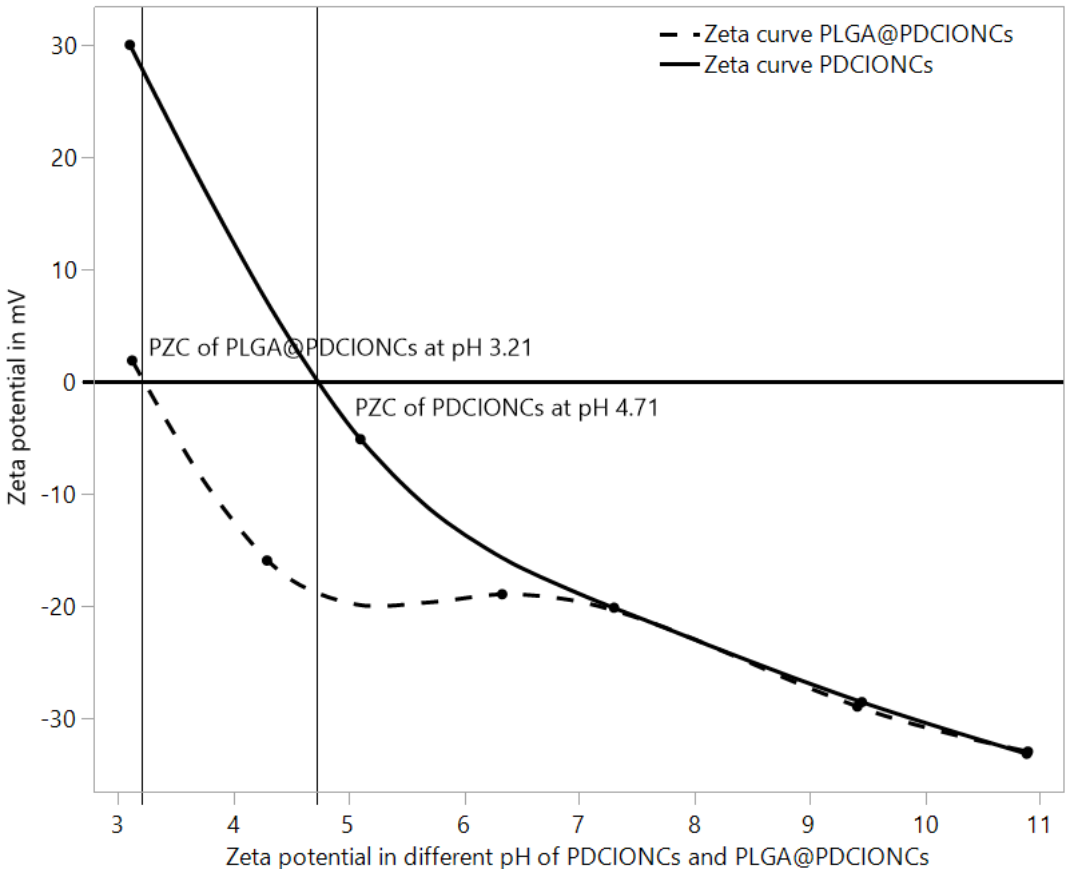

Figure 5.32: Stability test for PLGA@PDCIONCs with PDCIONCs as reference by measuring zeta potentials of different pH to create a zeta curve.

Figure 5.32 shows that the particles displayed different properties than that of the PD-

CIONCs where the PZC had further decreased to pH 3.21. It was also observed that the particles were within the -20/+20 mV zeta potential stable threshold at a wider pH range. This could prove useful in drug delivery as one would want the particles to release a drug and hence less stable particles are required. The last observation was that the PLGA@PDCIONCs were close in terms of zeta potential to the PDCIONCs after reaching a pH of 7.5. In the literature, a PZC of around 3 was reported by Okassa. L et al.[58]. The curve of the PLGA@PDCIONCs in the thesis was also well correlated to the curve in the study by Okassa. L et al.

5.6.3 Powder x-ray diffraction of PLGA@PDCIONCs

The PLGA@PDCIONCs were analyzed against the PDCIONCs to look for differences in the powder x-ray diffraction patterns of the different coated particles. The results are shown in Figure 5.33a and Figure 5.33b.

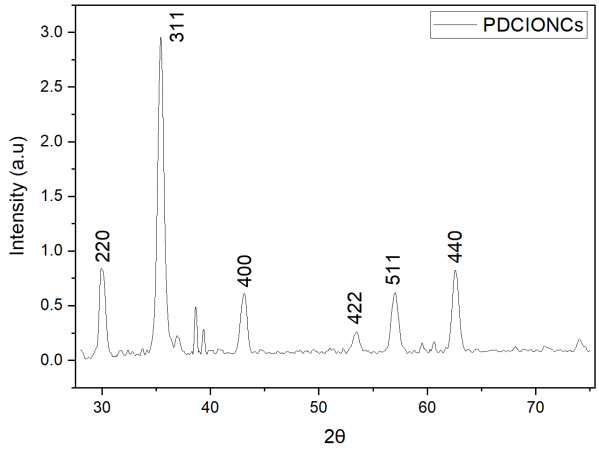

(a) XRD peaks of polydopamine coated iron oxide nanoclusters (PDCIONCs)

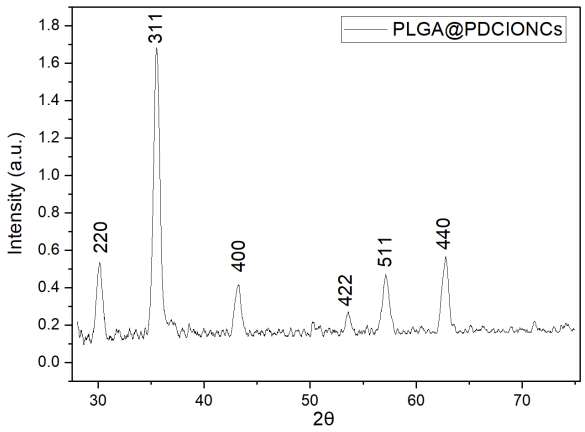

(b) XRD peaks of PLGA at polydopamine coated iron oxide nanoclusters (PLGA@PDCIONCs).

Figures 5.33a and 5.33b shows the different coated particles x-ray diffraction patterns. The first thing that was observed from the XRD peaks was that the intensity of the peaks in the pattern as well as noise to peak ratio had changed a lot from the coated PDCIONCs. This might indicate that the particles became less crystalline and more amorphous after the coating procedure of PLGA. That would be a good indication of the PLGA polymerization being successful. Most measurements done in the literature are limited to purely crystalline samples. The reason for measuring these particles in the powder x-ray diffraction was mainly to see how the peaks relative to the noise would change. Since both spectra were prepared and analyzed the exact same way, it indicates that there is a difference between the PLGA@PDCIONCs and PDCIONCs.

5.6.4 *FTIR* of PLGA@PDCIONCs

8 H PLGA@PDCIONCs were analyzed in FTIR together with the 8 H PDCIONCs batch. This was done to see any potential changes in the fingerprint region of 1200-1650 cm^{-1} and in the area of the Fe-O at 530 cm^{-1}. The resulting spectra is shown in Figure 5.34

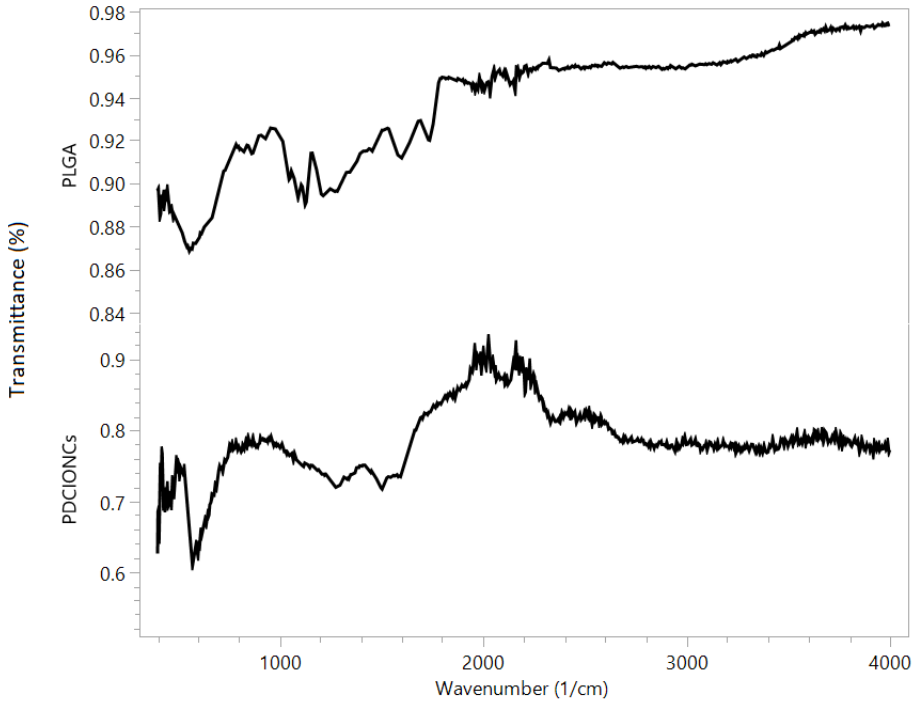

Figure 5.34: FTIR analysis of PLGA@PDCIONCs with PDCIONCs as reference.

Figure 5.34 shows the PLGA@PDCIONCs and the PDCIONCs FTIR spectra. It was observed that the noise was higher for the 8 H PDCIONCs than for the 8 H PLGA@PDCIONCs, but the general signal was also weaker for the 8 H PLGA@PDCIONCs. The peak at 2000 is a noise occurring from the instrument which was also observed in the different PDCIONCs batches. It could also be observed that the Fe-O bond at around 530 was still there after coating the particles with the PLGA, but giving a weaker signal. The fingerprint area of the polydopamine at about 1200-1650 did also change where the peaks at about 1300 cm^{-1} and 1500 cm^{-1} changed into what possibly could be a C=O bond at around 1740 cm^{-1}.

The graph looks similar to what was reported by Yang. Q et al. [81] where they polymerized PLGA on iron oxide. The main difference is that there is no visible O-H spread in the area of 3400. The PLGA@PDCIONCs did not seem to show neither O-H or N-H stretch at 3400. The wider N-H stretch would potentially be from the polydopamine. It could be the case that the N-H spread is present, but at a very broad and weak stretch. This would also prove the sudden rise in the 3600 area of the PLGA as the increase in transmittance may be from the N-H stretch.

An FTIR analysis was also done to the PLGA@PDCIONCs together with pure glycolide and pure lactide to see any pattern of how the monomers would form on the 8 H PLGA@PDCIONCs. The FTIR pattern is shown in Figure 5.35.

It was observed that the C=O bond from the GA and LA was also found in the PLGA@PDCIONCs, which is a good indication that there actually is PLGA grafted or in bulk on top of the PDCIONCs. When coating other particles with PLGA, the signal of the C=O tend to decrease which is also shown by Yang. Q et al. [81]. The fingerprint region of 1200-1600

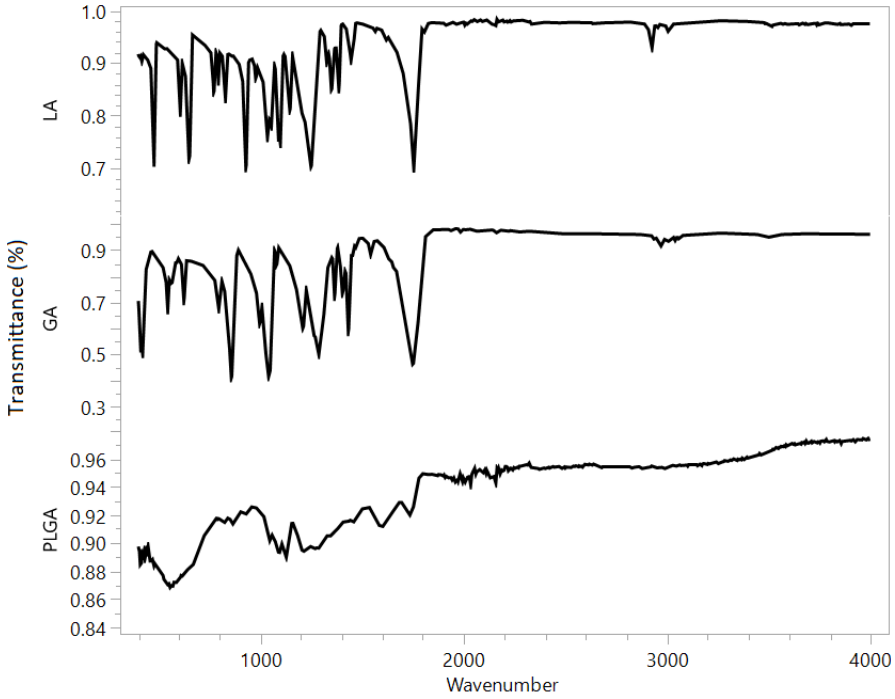

Figure 5.35: FTIR comparison of PLGA@PDCIONCs with the monomers glycolide and lactide.

cm^{-1} would prove hard to discuss between LA and GA to compare, as the signals between the monomers are hard to distinguish after coating the particle. It does however seem like the fingerprint changed from the PDCIONCs as shown in Figure 5.34, which means that most likely the monomers have been polymerized into PLGA before being grafted or most likely bulked on top of the PDCIONCs.

5.6.5 *S(T)EM* of PLGA@PDCIONCs

All PLGA@PDCIONCs batches were imaged in S(T)EM to see how the PLGA layer would form around the respective PLGA@PDCIONCs. The S(T)EM images of all the PLGA@PDCIONCs batches are shown in Figure 5.36.

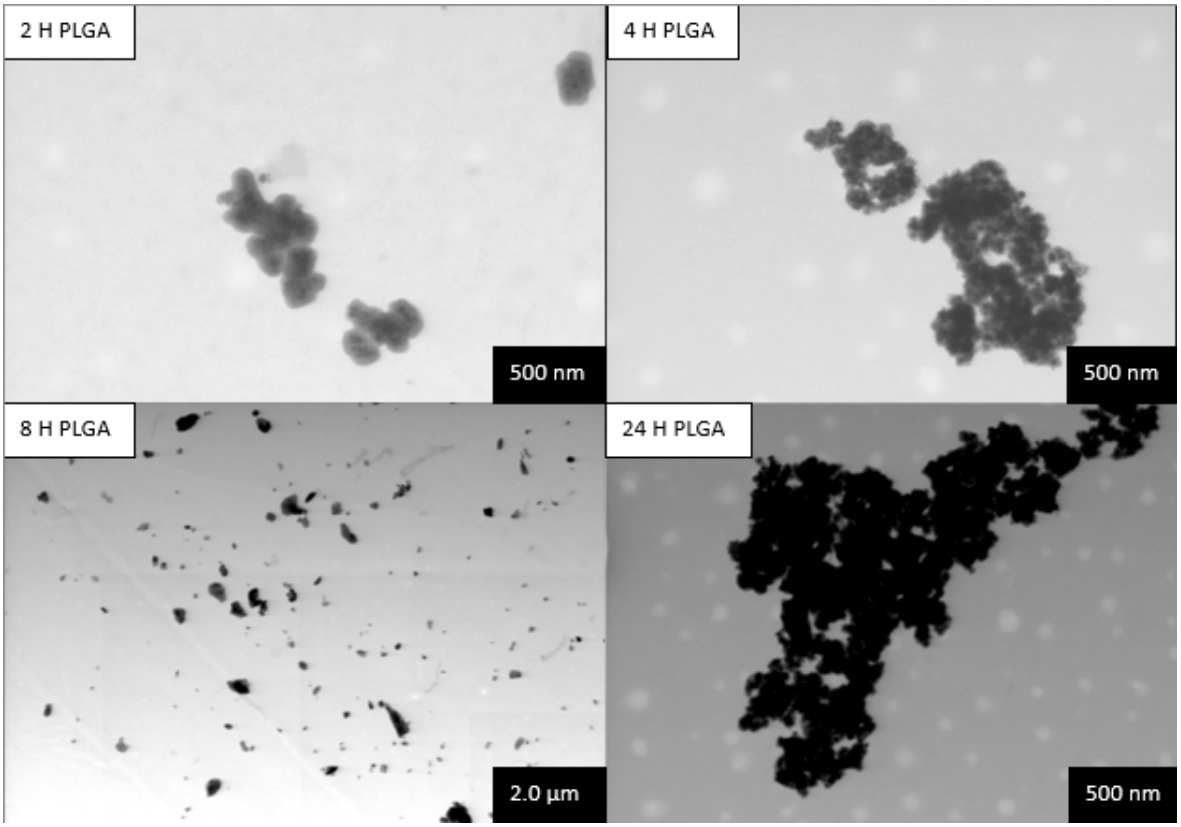

Figure 5.36: Images captured in S(T)EM of different batches of PLGA@PCIONCs.

Figure 5.36 shows images of the respective batches of PLGA@PDCIONCs. It was firstly observed that there were coated particles with mostly spheres and some clusters inside them. This could indicate that inside one of the processes of polymerization, the TREA reacted with something or the environment changed. The chelating properties of the TREA disappeared for most of the clusters. It could also be the neutralization of the basic environment when introducing the PLGA which is acidic that made the clusters split.

The sizes of the filtered particles were ranging from 300-900 nm. The particles shown in the Figure are coated and as observed they also tend to aggregate. The reason for this could be that the polymerization process ended up becoming bulk and not grafted which makes the particles harder to separate. It could also be that the particle charges are kept inside the layers and that they aggregate naturally through charge, but less likely as bulk PLGA is a thick coating. Either way, the big PLGA coated particles were not spherical and ended up with varying morphologies. The different PLGA@PDCIONCs were also proven to have different coating thickness which can be observed in the figure.

The typical trend observed was that the coating thickness increased at higher retraction times of the PDCIONCs conducted in the intermediate coating. To explain this, what would typically happen in the polydopamine coating would be that more polydopamine would set on top of the IONCs and creating more potential binding sites for the PLGA coating through longer exposure of oxidative polymerization. This means that the PLGA shell size would typically increase at longer polymerized PDCIONCs as it has more reac-

tive sites. This was not observed in the DLS for instance where the sizes of the particles are similar regardless of the batch, except for the 2 H batch.

Some particles were also above the micron size, but there was few after the filtration process. Before filtering the particles, one could expect particle sizes of several microns in S(T)EM stat were severely aggregated. To achieve nanometer size of the coated particles it would therefore be necessary to conduct a filtration process in order to stay at nano size which is desired for the hyperthermia application *in vivo*. In the study of Okassa. L et al.[58] the particles were also imaged. The particles produced in the thesis work was similar, but the sizes were found around 300 nm while in the thesis the sizes were ranging from 300-900. Another difference is that in the study by Okassa. L et al. they also stained the particles to see more easily where the coating of the PLGA was present.

There are still much work within this method to improve size control and reaction kinetics. One of the smaller studies to attempt reducing the particle size is found in the appendix.

5.6.6 Magnetherm of PLGA@PDCIONCs

8 H PLGA@PDCIONCs were tested and compared to the bare IONCs to see the heating efficiency of the PLGA@PDCIONCs after the coatings were polymerized on top of the bare IONCs. The heating efficiency graph in Figure 5.37 shows the temperature increase curves for the bare and coated IONCs.

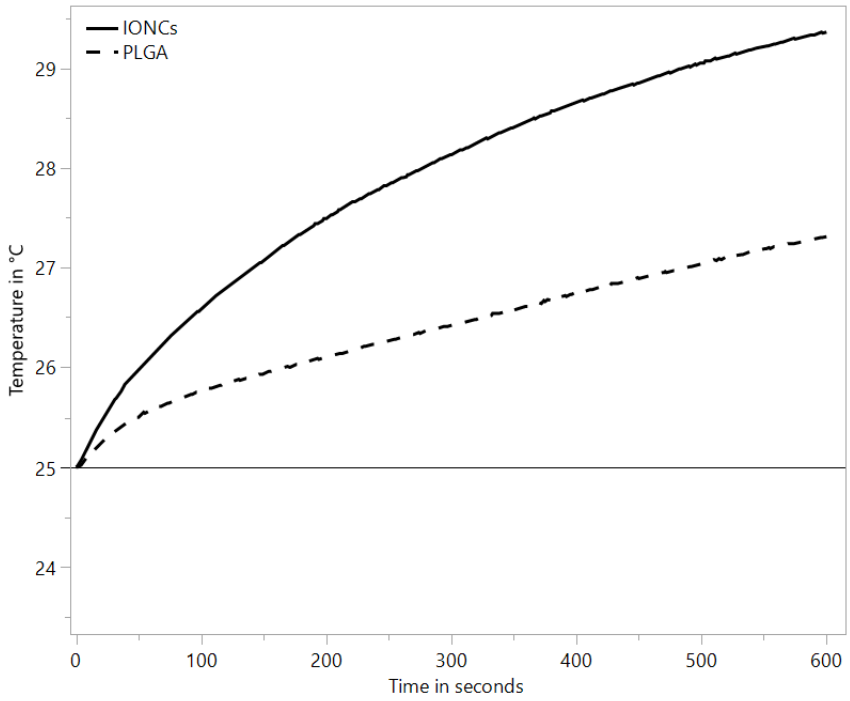

Figure 5.37: 5 times Brezovich limit measurements of PLGA@PDCIONCs vs IONCs in terms of ability to generate heat in the presence of an AMF. Heating rate is shown in ℃ per second.

Figure 5.37 shows the PLGA@PDCIONCs compared to the bare IONCs heating curves. It was observed that the heating efficiency of the coated particles decreased compared to the IONCs when being exposed to the AMF. This was expected as the coating layer typically

decreases the magnetic property due to blockage from the coating of the magnetic poles within the particles. The results in heating rate per minute and SAR also displayed a difference from the bare iron oxide nanoclusters. A study done by Khan. A et al.[82] showed that the particles saturation magnetization decreased though extensive coating of silica on top of a magnetic nanoparticle. Since the saturation magnetization is directly correlated to the SAR, this would explain the decreasing rate of temperature increase compared to the bare IONCs.

The temperature change rate and the SAR values are shown in Table 5.19.

Table 5.19: Table showing SAR values and heating rate per minute for PLGA@PDCIONCs and Nanoclusters 2.

Batch	Concentration (mg/mL)	SAR (w/g)	℃ increase per minute
8 H PLGA@PDCIONCs	0.5	165	0.23
Nanoclusters 2	0.5	303	0.44

Table 5.19 shows the SAR values and heating rates per minute of the 8 H PLGA@PDCIONCs together with bare IONCs. It was observed that the SAR values dropped a significant amount compared to before the particle was coated. The SAR and temperature increase rate however still remained higher than the most efficient bare nanosphere batch. The magnetic properties were not too much decreased from the bare particle as more than half of the SAR and temperature increase properties remained after coating the particle. The magnetic properties after coating could probably be optimized further by reducing the thickness of PLGA on the particles as well as optimizing the repulsion forces that reduces the degree of monodispersity for the coated particles.

Sufficient temperature increase, high SAR and not to much magnetic loss after coating indicates that the coated clusters can be well suited towards the hyperthermia application *in vivo*.

5.7 Drug loading and release studies

5.7.1 Drug loading of Salisylic Acid (SA) to PLGA@PDCIONCs

Salisylic acid has over the years proven to be effective as an anti-cancer drug. The drug has been proven to work especially well in Melanoma treatment through inducing stress to the cells by a nitric oxide cell apoptosis process as shown in Ausina. P et al.[8] where salisylic acid as well as acetyl-salisylic acid were tested towards Melanoma. There are however many other areas of usage when it comes to terminate cancers using salisylic acid. Salisylic acid was therefore attempted loaded into or onto PLGA@PDCIONCs.

Salisylic acid solutions at respectively pH 4, 7 and 10 were prepared and the particles were introduced to the salisylic acid solution. The particles were measured in UV-vis and the results for the respective pH's are shown in Figure 5.38a and Figure 5.38b

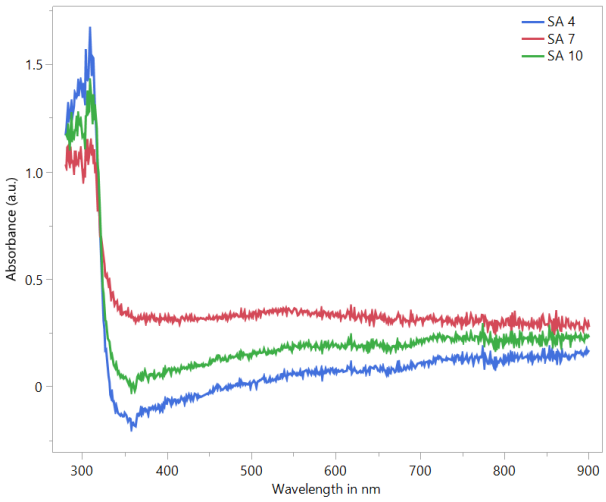

(a) UV-vis peaks of Pure salisylic acid solutions with respective pH of 4, 7 and 10.

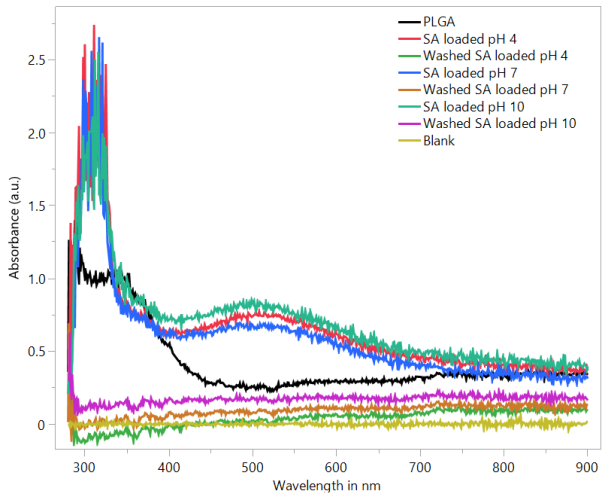

(b) UV-vis peaks of Washed and unwashed SA-loaded PLGA@PDCIONCs with unloaded PLGA@PDCIONCs as reference.

Figure 5.38a shows that the different pH of the solution affetced the absorbance of salisylic acid. The solution of pH 4 gave the most intensive peak, the solution of pH 10 gave the

second most intense peak and the neutral pH of 7 gave the least intense peak. This may prove that when introducing extensive pH, the salisylic acid may exhibit different properties as it absorbs more light when introducing the molecule to extensive pH of both basic and acidic environment. When looking at Figure 5.38b it shows the loaded particles with PLGA@PDCIONCs as reference point. The first observation of the Figure is that something has happened when loading the drug at the PLGA@PDCIONCs. It seems as the loading did work for all the different pHs, but at different intensities. It still seems that pH 4 gives the most intense absorbance peak, but now it is harder to differ between pH 7 and 10. The next observation done is that the washed particles give little to no peaks. This could also be due to the fact that when washing the particles, most of the particles would remain in the supernatant and hence very few were left in the re-dispersed solution. This could also be an indication to the SA adsorbing on top of the PLGA instead of internally, which would make it more prone to react with water. The water would disperse all the particles well and one would not be able to retrieve particles even with strong magnets. The adsorption theory was therefore tested by measuring the hydrodynamic size of the assumed loaded particles. The resulting hydrodynamic sizes for the respective pH and PLGA@PDCIONCs as reference point are shown in Figure 5.39

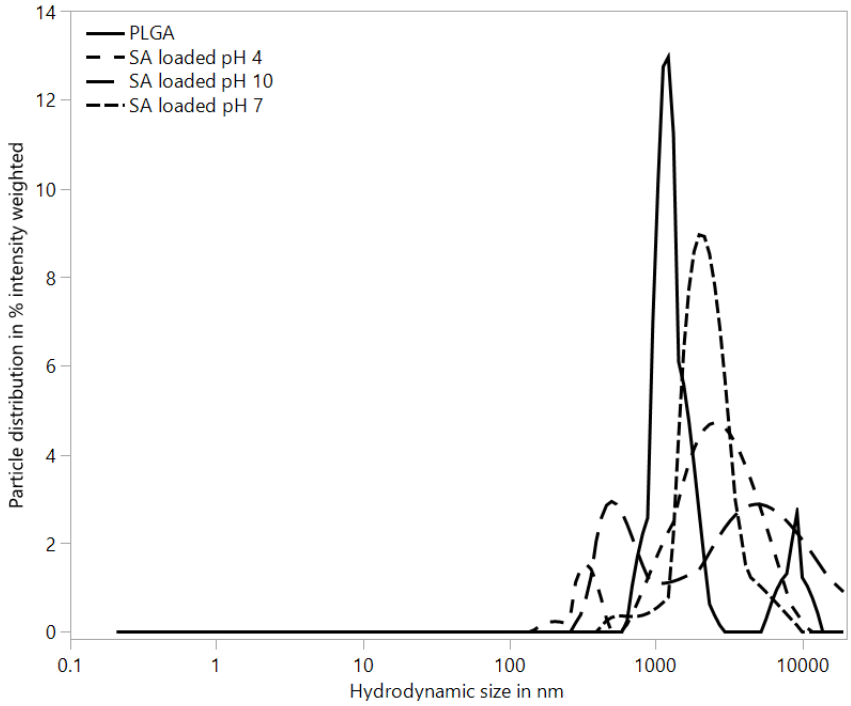

Figure 5.39: Hydrodynamic sizes of PLGA and SA loaded PLGA@PDCIONCs with respective pH of 4, 7 and 10.

From the Figure it seemed like the salisylic acid loading made a small impact on the particle sizes of the PLGA. It seems like the particles gained a bit of size which is not clearly visible as the graph shows the logarithmic scale and hence the particle size differences would be harder to observe. To see more clear difference of the hydrodynamic sizes, a depiction from a linear point of view is also presented in Figure 5.40.

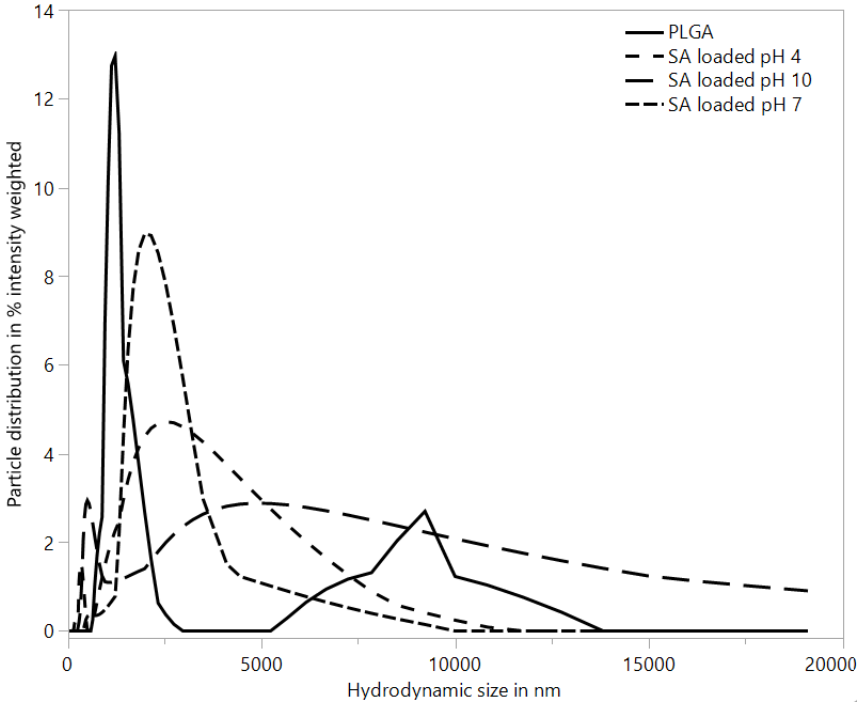

Figure 5.40: Hydrodynamic sizes of PLGA and SA loaded PLGA@PDCIONCs at pH of 4, 7 and 10 from a linear point of view.

Figure 5.40 shows the different hydrodynamic sizes of the drug loaded particles for the respective pH's. It was observed that the particles seem to increase a bit in size for all three different environments. It also seems like the particles in the extensive environments of pH 4 and 10 have a more potent increase in their hydrodynamic size. This could come from uncontrolled adsorption of the salisylic acid from protonated and deprotonated molecules creating hydrogen bonding. The particles in pH 7 does however seem to have some sort of controlled adsorption of salisylic acid. The reason adsorption could be the possible molecular interaction comes from the UV-vis measurements. If the particles absorbed the salisylic acid, the particle sizes should not have changed as well as the particles should still be separated properly using a magnet as they did not. This indicates that the molecules of salisylic acid could be adsorbed to the surface of the PLGA@PDCIONCs and hence would disperse better in water. To prove the direct adsorption of the salisylic acid onto the PLGA@PDCIONCs it should be conducted more characterizations like for instance RAMAN spectroscopy, pure PLGA with salisylic acid in proton NMR and TGA to see if the particles would decompose faster or slower after being loaded with the SA. If the adsorption is proven to be real and not just an indication as shown in this brief UV-vis/DLS combo measurement, it means the particles could become viable *in vivo* as anticancer nanoparticles. They would also be well directed as by using an AMF one could direct the particles into the target cancer-cell area and perform a combo of drug delivery together with hyperthermia.

6 Conclusion and suggested future work

6.1 Conclusion

Iron oxide nanospheres where synthesized using a thermal decomposition method known as the TREG synthesis where iron acetyl acetonate reacts with triethylene glycol (TREG) at 280 ℃ to create iron oxide nanospheres. The separation method of the iron oxide nanospheres was attempted optimized by using either centrifugation separation or magnetic separation in the separation optimization study. A anti-solvent study was also conducted together with separation to see if the volume of the anti-solvent *EtAc* in a ratio of 1:1 or 1:2 with ethanol would impact the particles. After characterizing the particles, it was found that there were few differences in the particles when using different separation methods, other than a possible indication of lower hydrodynamic sizes due to centrifugal forces removing the TREG better than the magnet. The magnetic separation method was therefore pursued for the rest of the thesis work.

The next step was the TREG optmization study. Mass of iron acetyl acetonate and volume of TREG was varied together with different volumes of the anti-solvent *EtAc* as the washing optimization was carried on from the separation optimization study. After characterizing the different iron oxide nanoparticles, it was found that all particles retained the same morphology and signals proving magnetite/maghemite in powder x-ray diffraction. The hydrodynamic sizes in the DLS was found at around 190-200 nm for all batches except 3.20 1 + 2 which showed lower sizes. It also seemed like the higher ratio of *EtAc* showed smaller hydrodynamic sizes of the particles. This was turned around in the S(T)EM sizes where the smallest particles seemed to be the particles with the lower washing ratio. The typical S(T)EM size was found to be 9 ± 2 nm. In general it seemed like there was no apparent trend in the sizes by varying the chemical parameters. It was later found that there was no trend in terms of magnetic properties between the particles. The only noticeable difference was found in the hyperthermia studies where the extremes of 3.20 1 + 2 and 1.30 1 + 2 increased temperatures faster. It was then decided to move on to try a different morphology, as changing the magnetic field strength would not be possible.

Iron oxide nanoclusters were then synthesized with thermal decomposition of iron acetyl acetonate together with TREG and triethanolamine (TREA). The particles were only washed in a 2:1 ratio of *EtAc*:ethanol. The hydrodynamic sizes were found to be smaller than that of the spheres and also more monodisperse. The S(T)EM sizes showed that the clusters were a bit bigger than the spheres at 19 nm. The clusters were way better in terms of magnetic properties, where the clusters saturation magnetization was proven to be 72 emu/g. This was a lot compared to the spheres at 49-54 emu/g. The hyperthermia efficiency was also raised 4 times in terms of both temperature increase and SAR values by moving from the spheres to the clusters. The clusters were therefore further utilized in the research.

Polydopamine coating was prepared through oxidative polymerization on top of iron oxide nanoclusters at room temperature and particles were retracted at 2, 4, 8 and 24 hours. These particles were named PDCIONCs. It was found that one could to some extent control the coating thickness by retracting the particles at different times. This

also changed the zeta potential of the particles by them decreasing through longer polymerization exposure time. It was found that the signals of polydopamine increased when increasing the polymerization exposure for up to 8 hours. The particles did also display different colors, which was proven by absorption in the UV-vis spectra.

Poly-lactic-co-glycoic acid was polymerized on top of PDCIONCs by melting monomers and conducting a solvent free polymerization with the initiator stannous octoate and named PLGA@PDCIONCs. It was found that the sizes were hard to measure in the DLS. The particles were filtered and measured in the DLS and also measured in S(T)EM where the sizes of the particles ranged from 300-900 nm. The particles fingerprint area in FTIR changed after comparing with the PDCIONCs. The particles were also compared to the monomers where there was found peak matches from both monomers.

In the drug loading section where salisylic acid at pH 4, 7 and 10 were loaded into/onto PLGA@PDCIONCs it was found that the drug possibly became adsorbed and not absorbed and that the interaction of the drug induced bigger sizes of the PLGA@PDCIONCs in the DLS measurements. The drug loading mechanism would therefore need more work and characterization to prove the possible interactions.

Due to the PLGA@PDCIONCs magnetic properties, heating capabilities and its function as a potential drug loading particle, the PLGA@PDCIONCs can be good candidate for hyperthermia and drug delivery *in vivo* in the future.

6.2 Suggested future work

There could potentially be a lot of other particles with different aspect ratios and morphologies that could work well in the hyperthermia application. One could also possibly manipulate synthesis methods to improve the TREG/TREA synthesis to create more magnetic nanoparticles through optimization work inside the synthesis. This could potentially create better particles than what was presented in the thesis. To further understand how this works, one could go more into the reaction mechanisms and understand what is happening on a molecular level inside the thermal decomposition method. One could also conduct a lot of other characterization techniques towards all of the potential iron oxide nanoparticles to understand how to properly manipulate and engineer the desired optimal particle. When it comes to the coating, polydopamine is quite researched already, but one still needs to understand how the polydopamine behaves and its kinetics and etc. before one could be sure that everything works the way one assumes. For the PLGA one must research the sizes and grafting techniques of the particles to try and avoid the large aggregates which makes up most of the polymerized particles. The filtering process could be avoided in the future by properly investigating the polymerization and how it works on top of the amine surface. Finally, the drug loading should also be investigated further by conducting several other characterization techniques on the assumed loaded particles. This is, to be sure how the loading mechanism works and that it could be viable *in vivo*. It is therefore a lot of optimization work that still can be done on the thermal decomposition methods, the TREG synthesis, understanding amine surfaces, PLGA coating and drug loading.

References

[1] World Health Organization International Agency for Research on Cancer with data from GLOBOCAN. Cancer today. 2020.

[2] National Cancer Institute. Cancer statistics. 2020.

[3] Eric J. Jacobs S. Jane Henley Carmen Rodriguez-Eugenia E. Calle Ann Chao, Michael J. Thun. Cigarette smoking and colorectal cancer mortality in the cancer prevention study ii. 2000. doi: 10.1093/jnci/92.23.1888.

[4] Kinam Park Yeon Hee Yun, Byung Kook Lee. Controlled drug delivery: Historical perspective for the next generation. *Journal of Controlled Release*, 219:2–7, 2015. doi: 10.1016/j.jconrel.2015.10.0058.

[5] National Cancer Institute. Hyperthermia to treat cancer. 2021.

[6] Javier B Mamani Suzana MF Malheiros Luciana Malavolta Lorena F Pavon Tatiana T Sibov Edson Amaro Jr Alberto Tannús-Edson LG Vidoto Mateus J Martins Ricardo S Santos André C Silva, Tiago R Oliveira and Lionel F Gamarra. Application of hyperthermia induced by superparamagnetic iron oxide nanoparticles in glioma treatment. *International Journal of Nanomedicine*, 6:591–603, 2011. doi: 10.2147/IJN.S14737.

[7] Hongwei Liao Zeyu Liang Fangyuan Li Jie Tian Qiyue Wang, Xibo Ma and Daishun Ling. Artificially engineered cubic iron oxide nanoparticle as a high-performance magnetic particle imaging tracer for stem cell tracking. *ACS Nano*, 14:2053–2062, 2020. doi: 10.1021/acsnano.9b08660.

[8] Thainá M. Demaria Amanda M. Esteves João Gabriel B. Leandro Alan C. Ochioni Ana Paula M. Mendonça Fernando L. Palhano-Marcus F. Oliveira Wassim Abou-Kheir Mauro Sola-Penna Priscila Ausina, Jessica R. Branco and Patricia Zancan. Acetylsalicylic acid and salicylic acid present anticancer properties against melanoma by promoting nitric oxide-dependent endoplasmic reticulum stress and apoptosis. *Sci Rep*, 10:19617, 2020. doi: 10.1038/s41598-020-76824-6.

[9] Bandyopadhyay. S. *Fabrication and application of nanomaterials*. McGrawHill, 2019.

[10] Mohd Afnan Ahmad Wan Nur Athirah Mazli and Shafirah Samsuri. *Nucleation*. Intechopen, 2019. doi: 10.5772/intechopen.90164.

[11] J.H. Harker J.F. Richardson and J.R. Backhurst. *Crystallisation*, volume 2. Butterworth Heinemann, 2002.

[12] N. Maclean Nguyen T. K. Thanh and S. Mahiddine. *Mechanisms of Nucleation and Growth of Nanoparticles in Solution*, volume 115. American Chemical Society, 2014. doi: 10.1021/cr400544s.

[13] G Cao and Y. Wang. *Nanomaterials 2nd edition*. World scientific publishing, 2011.

[14] Chen-Yan Zhang Ren-Bin Zhou, Hui-Ling Cao and Da-Chuan Yin ORCID. A review on recent advances for nucleants and nucleation in protein crystallization. *CrystEngComm*, 19:1143–1155, 2017. doi: 10.1039/C6CE02562E.

[15] Xiaoyu Chuai Shijie Xu, Zhongbi Hou and Yanfei Wang. Overview of secondary nucleation: From fundamentals to application. 41:18335–18356, 2020. doi: 10.1021/acs.iecr.0c03304.

[16] Sania Naz Samson O. Aisida Noor ul Ain Qiang Ao Rabia Javed, Muhammad Zia. Role of capping agents in the application of nanoparticles in biomedicine and environmental remediation recent trends and future prospects. *Journal of Nanobiotechnology*, 18:172, 2020. doi: 10.1186/s12951-020-00704-4.

[17] Şerzat Safaltın and Sebahattin Gürmen. Computational materials science. *Computional Materials Science*, 183:109842, 2020.

[18] Stephen G Hickey Lydia Bahrig and Alexander Eychmüller. Mesocrystalline materials and the involvement of oriented attachment. *CrystEngComm*, 16:9408–9424, 2014. doi: 10.1039/C4CE00882K.

[19] Vahak Marghussian. *Nano-Glass Ceramics*. Elsevier, 2015.

[20] Vahak Marghussian. 4 - magnetic properties of nano-glass ceramics. *Nano-Glass Ceramics Processing, Properties and Applications*, pages 181–223, 2015. doi: 10.1016/B978-0-323-35386-1.00004-9.

[21] Ahmed Salih Mohammed Nzar Shakr Piro, Samir Mustafa Hamad and Azeez Abdullah Barzinjy. Green synthesis magnetite (feo) nanoparticles from rhus coriaria extract: A characteristic comparison with a conventional chemical method. *IEEE Transactions on NanoBioscience*, 22:308–317, 2023. doi: 0.1109/TNB.2022.3187344.

[22] Chak-Tong Au Xuemin He1, Wei Zhong and Youwei Du. Size dependence of the magnetic properties of ni nanoparticles prepared by thermal decomposition method. *Nanoscale Research Letters*, 8, 2013. doi: 10.1186/1556-276X-8-446.

[23] Andreina Chiu-Lam Daniel W. Hensley Rohan Dhavalikar Xinyi Y. Zhou Elaine Y. Yu Patrick W. Goodwill Bo Zheng Carlos Rinaldi Zhi Wei Tay, Prashant Chandrasekharan and Steven M. Conolly. Magnetic particle imaging-guided heating in vivo using gradient fields for arbitrary localization of magnetic hyperthermia therapy. *ACS NANO*, 12, 2018. doi: 10.1021/acsnano.8b00893.

[24] Kannan M. Krishnan Amit P. Khandhar, R. Matthew Ferguson. Monodispersed magnetite nanoparticles optimized for magnetic fluid hyperthermia: Implications in biological systems. *Journal of Applied Physics*, 109, 2011. doi: 10.1063/1.3556948.

[25] R. Matthew Ferguson Marcela Gonzales Eric Teeman Lucien N. Brush Nigel D. Browning Ryan Hufschmid, Hamed Arami and Kannan M. Krishnan. Synthesis of phase-pure and monodisperse iron oxide nanoparticles by thermal decomposition. *Nanoscale*, pages 11142–11154, 2015. doi: 10.1039/C5NR01651G.

[26] Pallab Pradhan Kai-Hsiang Chuang Jun-Min Xue Si-Shen Feng Dipak Maity, Prashant Chandrasekharan and Jun Ding. Novel synthesis of superparamagnetic magnetite nanoclusters for biomedical applications. *Journal of Materials Chemistry*, 21:14717–14724, 2011. doi: 10.1039/C1JM11982F.

[27] Ayodele Temidayo Odularu. Metal nanoparticles: Thermal decomposition, biomedicinal applications to cancer treatment, and future perspectives. 2018. doi: 10.1155/2018/9354708.

[28] Gianna Labiento Elijah Cook and Bhanu P. S. Chauhan. Fundamental methods for the phase transfer of nanoparticles. *molecules*, 26:6170, 2021. doi: 10.3390/molecules26206170.

[29] R. Matthew Ferguson-Marcela Gonzales Eric Teeman Lucien N. Brush Nigel D. Browning Ryan Hufschmid, Hamed Arami and Kannan M. Krishnana. Synthesis of phase-pure and monodisperse iron oxide nanoparticles by thermal decomposition. 7:11142–11154, 2015. doi: 10.1039/c5nr01651g.

[30] D. Couri and M Milks. Toxicity and metabolism of the neurotoxic hexacarbons n-hexane, 2-hexanone, and 2,5-hexanedione. *Annual Review of Pharmacology and Toxicology*, 22:145–166, 1982. doi: 10.1146/annurev.pa.22.040182.001045.

[31] Luanne Hall-Stoodley Iolanda Francolini and Paul Stoodley. *Biofilms, Biomaterials, and Device-Related Infections*. ACADEMIC PRESS, 2020. doi: 10.1016/B978-0-12-816137-1.00054-4.

[32] Harvey B. Simon. Hyperthermia. *N Engl J Med 1993*, 329:483–487, 1993. doi: 10.1056/NEJM199308123290708.

[33] Zhengqiang Yang Xuman Wang, Hongchen Gu. The heating effect of magnetic fluids in an alternating magnetic field. *Journal of Magnetism and Magnetic Materials*, 293: 334–340, 2005. doi: 10.1016/j.jmmm.2005.02.028.

[34] Khurram Shahzad and Wael Mati. Advances in magnetic resonance imaging (mri). pages 121–142, 2020. doi: 10.1016/B978-0-12-819712-7.00009-7.

[35] R. Meyers K. Kekalo, I. Baker and J. Shyong. Magnetic nanoparticles with high specific absorption rate at low alternating magnetic field. *Nano LIfe*, 5, 2015. doi: 10.1142/S1793984415500026.

[36] Okan Icten. Functional nanocomposites: promising candidates for cancer diagnosis and treatment. pages 279–340, 2021. doi: 10.1016/B978-0-12-818429-5.00008-9.

[37] Robert Stigliano Alicia Petryk P. Jack Hoopes Fridon Shubitidze, Katsiaryna Kekalo and Ian Baker. Magnetic nanoparticles with high specific absorption rate of electromagnetic energy at low field strength for hyperthermia therapy. *Journal of applied physics*, 117, 2015. doi: 10.1063/1.4907915.

[38] D.J. Dunlop and Ö. Özdemir. Magnetizations in rocks and minerals. *Journal of applied physics*, 5:277–336, 2007. doi: 10.1016/B978-044452748-6.00093-6.

[39] Yasuhito Takahashi Takuya Shibataki and Koji Fujiwara. Investigation of measurement method of saturation magnetization of iron core material using electromagnet. *AIP advances 23rd Soft Magnetic Materials Conference*, 8, 2018. doi: 10.1063/1.4993998.

[40] Ehsan Nazarzadeh Zare Franklin R. Tay Chen-yu Wang, Pooyan Makvandi and

Li na Niu. Advances in antimicrobial organic and inorganic nanocompounds in biomedicine. *Advanced Therapeutics*, 3, 2020. doi: 10.1002/adtp.202000024.

[41] Stefan Ursache Mioara Drobota and Magdalena Aflori. Surface functionalities of polymers for biomaterial applications. *Polymers(Basel)*, 12:2307, 2022. doi: 10.3390/polym14122307.

[42] Arnout Imhof Christina Graf, Dirk L. J. Vossen and Alfons van Blaaderen. A general method to coat colloidal particles with silica. *Langmuir*, 19:6693–6700, 2003. doi: 10.1021/la0347859.

[43] Rodica Turcu Joachim Leistner Jürgen Liebscher Radosław Mrówczyński, Alexandrina Nan. Polydopamine – a versatile coating for surface-initiated ring-opening polymerization of lactide to polylactide. *Macromolecular Chemistry and Physics*, 216:211–217, 2014. doi: 10.1002/macp.201400380.

[44] Daniel E. Heath and Stuart L. Cooper. Polymers: Basic principles. pages 64–79, 2013. doi: 10.1016/B978-0-08-087780-8.00008-5.

[45] Shuai Chen Erik Jan Cornel, Jinhui Jiang and Jianzhong Du. Principles and characteristics of polymerization-induced self-assembly with various polymerization techniques. *CCS Chemistry*, 3:2104–2125, 2021. doi: 10.31635/ccschem.020.202000470.

[46] Coleman. M. *Fundamentals of polymer science*. TaylorFrancis group, 2019.

[47] Wan Hanisah B. Wan Ibrahim and Iqbal M. Mujtaba. Dynamic optimization of solution polymerization process of methyl methacrylate in batch reactors. *Computer Aided Chemical Engineering*, 31:1326–1330, 2012. doi: 10.1016/B978-0-444-59506-5.50096-1.

[48] Daniel J. Hines and David L. Kaplan. Poly (lactic-co-glycolic acid) controlled release systems: experimental and modeling insights. *Critical Reviews™ in Therapeutic Drug Carrier Systems*, 30:257–276, 2014. doi: 10.1615/critrevtherdrugcarriersyst.2013006475.

[49] Kevin Ka Leung Cheuk Yunzi Hu, Walid A. Daoud and Carol Sze Ki Lin. Newly developed techniques on polycondensation, ring-opening polymerization and polymer modification: Focus on poly(lactic acid). *Materials*, 9, 2016. doi: 10.3390/ma9030133.

[50] Jian-Bo Cao Kai-Mei Ke Qiao-Li Peng Jinhao Gao Huang-Hao Yang Gang Liu Li-Sen Lin, Zhong-Xiao Cong and Xiaoyuan Chen. Multifunctional fe3o4@polydopamine core–shell nanocomposites for intracellular mrna detection and imaging-guided photothermal therapy. 2014. doi: 10.1021/nn500722y.

[51] Cafer T. Yavuz William W. Yu, Joshua C. Falkner and Vicki L. Colvin. Synthesis of monodisperse iron oxide nanocrystals by thermaldecomposition of iron carboxylate salts. *Chemical communications*, pages 2306–2307, 2004. doi: 10.1039/B409601K.

[52] Ruchika Kaul-Ghanekar Jun-Min Xue-Jun Ding Dipak Maity, S.N. Kale. Studies of magnetite nanoparticles synthesized by thermal decomposition of iron (iii) acety-

lacetonate in tri(ethylene glycol). *Journal of Magnetism and Magnetic Materials*, 321:3093–3098, 2009. doi: 10.1016/j.jmmm.2009.05.020.

[53] Feng Si-Shen Jun-Min Xue Dipak Maity, Prashant Chandrasekharan and Jun Ding. Polyol-based synthesis of hydrophilic magnetite nanoparticles. *Journal of Applied Physics*, 107, 2010. doi: DOI:10.1063/1.3355898.

[54] Celine Mirjolet-Thomas Nury-Suban Kumar Sahoo Nadine Millot Nimisha Singh, Fadoua Sallem and Rajender Kumar. Polydopamine modified superparamagnetic iron oxide nanoparticles as multifunctional nanocarrier for targeted prostate cancer treatment. 2019. doi: 10.3390/nano9020138.

[55] Weifeng Zhao-Qiang Wei-Shengqiang Nie Shudong Sun Chong Cheng, Shuang Li and Changsheng Zhao. The hydrodynamic permeability and surface property of polyethersulfone ultrafiltration membranes with mussel-inspired polydopamine coatings. *Journal of Membrane Science*, 417-418:228–236, 2012. doi: 10.1016/j.memsci.2012.06.045.

[56] Robert Cavanagh Amjad Abouselo Edward A. Apebende Amir Ghaemmaghami Dong-Hyun Kim Jonathan W. Aylott Vincenzo Taresco Veeren M. Chauhan Mohamed D. Yousif, Mohammad A. Al-Natour and Cameron Alexander. Facile dye-initiated polymerization of lactideglycolide generates highly fluorescent poly(lactic-co-glycolic acid) for enhanced characterization of cellular delivery. *ACS Macro Letters*, 11:1224, 2022. doi: 10.1021/acsmacrolett.2c00570.

[57] Xin Liang-Jinxie Zhang Wei Tao Xianbing Zhu Danfeng Chang Xiaowei Zeng Gan Liu Xudong Zhang, Hongqiu Zhang and Lin Mei. Iron oxide nanoparticles induce autophagosome accumulation through multiple mechanisms: Lysosome impairment, mitochondrial damage, and er stress. *Molecular pharmaceutics*, 13:2578–2587, 2016. doi: 10.1021/acs.molpharmaceut.6b00405.

[58] Laurence Douziech-Eyrolles Katel Hervé Simone Cohen-Jonathan Emilie Munnier Martin Soucé Claude Linassier Pierre Dubois Lazare Ngaboni Okassa, Hervé Marchais and Igor Chourpa. Optimization of iron oxide nanoparticles encapsulation within poly(d,l-lactide-co-glycolide) sub-micron particles. *European Journal of Pharmaceutics and Biopharmaceutics*, 67:31–38, 2007. doi: 10.1016/j.ejpb.2006.12.020.

[59] Shakkthivel Piraman Sasikala Sundar, Ramalakshmi Mariappan. Synthesis and characterization of amine modified magnetite nanoparticles as carriers of curcumin-anticancer drug. *Powder Technology*, 266:321–328, 2014. doi: 10.1016/j.powtec.2014.06.033.

[60] Robert Cavanagh Amjad Abouselo Edward A. Apebende Amir Ghaemmaghami Dong-Hyun Kim Jonathan W. Aylott Vincenzo Taresco Veeren M. Chauhan Mohammad A. Al-Natour, Mohamed D. Yousif and Cameron Alexander. Facile dye-initiated polymerization of lactideglycolide generateshighly fluorescent poly(lactic-co-glycolic acid) for enhancedcharacterization of cellular delivery. *ACS Macro Letters*, 9:431–437, 2020. doi: 10.1021/acsmacrolett.9b01014.

[61] Anton Paar GmbH. The principles of dynamic light scattering. 2022.

[62] Dnyaneshwar Kalyane Susanne R. Youngren-Ortiz Mahavir B. Chougule Rakesh K. Tekade Nidhi Raval, Rahul Maheshwari. *Importance of Physicochemical Characterization of Nanoparticles in Pharmaceutical Product Development*. Academic Press, 2019. doi: 10.1016/B978-0-12-817909-3.00010-8.

[63] Pontus Lurcock. Notes on producing day plots from micromag vsm data. 2018. doi: 10.5281/zenodo.1244231.

[64] A.O. Adeyeye and G. Shimon. Magnetism of surfaces, interfaces, and nanoscale materials. *Handbook of Surface Science*, 5:1–41, 2015. doi: doi.org/10.1016/B978-0-444-62634-9.00001-1.

[65] J Vinila, V.S Isac. *Chapter 14 - Synthesis and structural studies of superconducting perovskite GdBa2Ca3Cu4O10.5+ nanosystems*. Elsevier, 2022. doi: 10.1016/B978-0-12-820558-7.00022-4.

[66] Sarah D. Rafiee Jules L. Hammond, Nikhil Bhalla and Pedro Estrela. Localized surface plasmon resonance as a biosensing platform for developing countries. *Biosensors (Basel)*, 2:172–188, 2014. doi: 10.3390/bios4020172.

[67] Dr. Susanne Pahlow Dr. Thomas G. Mayerhöfer and Prof. Dr. Jürgen Popp. The bouguer-beer-lambert law: Shining light on the obscure. *ChemPhysChem*, 21:2029–2046, 2020. doi: 10.1002/cphc.202000464.

[68] Zorica Crnjak Orel Gabriela Ambrozic and Majda Zigon. Microwave-assisted non-aqueous synthesis of zno nanoparticles. *Materials and Technologies*, 45:173–177, 2011. doi: 10.1063/1.4993998.

[69] A. Baykal H. Sözeri M. Günay, H. Erdemi and M.S. Toprak. Triethylene glycol stabilized mnfe2o4 nanoparticle: Synthesis, magnetic and electrical characterization. *Materials Research Bulletin*, 48:1057–1064, 2013. doi: 10.1016/j.materresbull.2012.11.097.

[70] V.P. Ponomar. Synthesis and magnetic properties of magnetite prepared by chemical reduction from hematite of various particle sizes. *Journal of Alloys and Compounds*, 741:28–34, 2018. doi: 10.1016/j.jallcom.2018.01.023.

[71] Hiroyuki Itoh and Tadao Sugimoto. Systematic control of size, shape, structure, and magnetic properties of uniform magnetite and maghemite particles. *Journal of Colloid and Interface Science*, 265:283–295, 2003. doi: 10.1016/S0021-9797(03)00511-3.

[72] Jon Gutiérrez-Basoa Sira Iturrizaga Correcher Carmen Mar Medina Jose Javier Echevarría-Uraga Jose Angel Garcia Fernando Plazaola Borja Herrero de la Parte, Irati Rodrigo and Ignacio García-Alonso1. Proposal of new safety limits for in vivo experiments of magnetic hyperthermia antitumor therapy. *Cancers (Basel)*, 13:3084, 2022. doi: 10.3390/cancers14133084.

[73] A.W. Zaibudeen John Philip B.B. Lahiri, Surojit Ranoo. Magnetic hyperthermia in magnetic nanoemulsions: Effects of polydispersity, particle concentration and

medium viscosity. *Journal of Magnetism and Magnetic Materials*, 441:310–327, 2017. doi: 10.1016/j.jmmm.2017.05.076.

[74] Huijie Sun Zhiqian Jia and Qingyang Gu. Preparation of ag nanoparticles with triethanolamine as reducing agent and their antibacterial property. *Colloids and Surfaces A: Physicochemical and Engineering Aspects*, 419:174–179, 2013. doi: 10.1016/j.colsurfa.2012.12.003.

[75] Ronald S Sapieszko and Egon Matijević. Preparation of well-defined colloidal particles by thermal decomposition of metal chelates. i. iron oxides. *Journal of Colloid and Interface Science*, 74:405–422, 1980. doi: 10.1016/0021-9797(80)90210-6.

[76] Jorge A. Calderón Carolina Ramírez, Benedetto Bozzini. Electrodeposition of copper from triethanolamine as a complexing agent in alkaline solution. *Electrochimica Acta*, 425:140654, 2022. doi: 10.1016/j.electacta.2022.140654.

[77] Kaili Lin Anting Jin, Yitong Wang and Lingyong Jiang. Nanoparticles modified by polydopamine: Working as "drug" carriers. *Bioactive Materials*, 5:522–541, 2020. doi: 10.1016/j.bioactmat.2020.04.003.

[78] Dominic Crestani Marc C. A. Stuart Alessia Lasorsa Patrick C. A. van der Wel-Katja Loos Theodosis Giousis Vahid Haddadi-Asl Petra Rudolf Hamoon Hemmatpour, Oreste De Luca. New insights in polydopamine formation via surface adsorption. 2021. doi: 10.1038/s41467-023-36303-8.

[79] Joop G.C. Wolke John A. Jansen Jan C.M. van Hest Rosa P. Félix Lanao, Anika M. Jonker and Sander C.G. Leeuwenburgh. Physicochemical properties and applications of poly(lactic-co-glycolic acid) for use in bone regeneration. *Tissue Eng Part B Rev*, 4:380–390, 2013. doi: 10.1089/ten.teb.2012.0443.

[80] Jaison Jeevanandam Shahira M. Ezzat Kingsley C. Patrick-Iwuanyanwu Charles Oluwaseun Adetunji Johra Khan-Eugene N. Onyeike Chukwuemelie Zedech Uche-Muhammad Akram Mervat S. Ibrahim-Nihal M. El Mahdy Chinaza Godswill Awuchi Kaliyaperumal Saravanan Habibu Tijjani Uchenna Estella Odoh Mohammed Messaoudi Jonathan C. Ifemeje Michael C. Olisah Nebechi Jane Ezeofor Chukwudi Jude Chikwendu Chukwuebuka Egbuna, Vijaykumar K. Parmar and Chinwe Gloria Ibeabuchi. Toxicity of nanoparticles in biomedical application: Nanotoxicology. *Journal of toxicology*, 2021:1–21, 2021. doi: 10.1155/2021/9954443.

[81] Fang Lan Shaohua Ma Liqin Xie Bin He Qi Yang, Yao Wu and Zhongwei Gu. Nanotechnologynanotechnology 25 (2014) 085702 (8pp) doi:hollow superparamagnetic plga/fe3o4composite microspheres for lysozymeadsorptions. *Nanotechnology*, 25, 2014. doi: 10.1088/0957-4484/25/8/085702.

[82] Muhammad Farooq Nasir Afsheen Sultana Khan and Asif Humayun. Magnetic and heating properties of $la_{1-x}sr_{1-x}mno_3$ (x = 0.27 0.33) mediators coated by sodium oleate for magnetic fluid hyperthermia applications. *Physica B: Condensed Matter*, 550:1–8, 2018. doi: 10.1016/j.physb.2018.08.003.

7 Appendix

This section is dedicated to show the work which was done, but not included into the thesis. The reason for this could be that the results were not satisfactory, errors were discovered throughout the process or that something was tested to see if it would prove useful for the main objective of the thesis.

7.1 Separation optimization study

When looking at the separation optimization, there was a synthesis conducted where a group of particles were attempted washed with the ratio of 3:1 EtAc:ethanol. The resulting particles were measured in the DLS and was found to have a hydrodynamic size of around 274 nm. What could be observed from this is that the excess EtAc used might have had some interactions with the TREG layer, due to sizes being almost twice as big as the other magnetically separated particles. The S(T)EM sizes were found at 9 ± 2 nm which is within the range together with most of the other particles. The particles saturation magnetization was found to be 51 emu/g and hence not too different from other particles measured in both the separation optimization and the TREG optimization.

7.2 Optimization of assumed dopamine coating on IONCs (DCIONCs)

Before knowing the importance of the tris-buffer in polymerizing the PD on top of the IONCs the polymerization was attempted with both an uncontrolled assumed buffer solution as well as without the presence of tris-buffer. The reason for trying the polydopamine synthesis without the presence of tris-buffer was that it was observed that sizes in the DLS measurements were way above nanoscale and hence could not be considered as a nano method to use in the application of hyperthermia. To prove the size differences, the results of the sizes which was measured in DLS is shown below in Table 7.1.

Table 7.1: Hydrodynamic sizes of IONCs and DCIONCs with and without presence of tris-buffer.

Type of particle	Hydrodynamic size in nm	Hydrodynamic size with tris in nm
Bare nanoclusters	120 ± 0.5	605± 22
Coated nanoclusters	1100 ± 100	4000 ± 500

From the table it can be observed that the sizes increase when the particles are in contact with the tris-buffer. The tris- buffer was therefore later not used in the attempt to optimize the coating process before knowing that for the formation of polydopamine to occur on the surface of the IONCs, the pH must be 8.5. The buffer also had to be solid to avoid being impacted by the dopamine hydrochloride. What was therefore assumed is that another dopamine formation than polydopamine might have occurred on top of the IONCs. Due to lack of knowledge, a couple experiments and measurements were spent on trying to optimize what was assumed to be the polydopamine formation.

7.2.1 Optimization of DCIONCs without TRIS

Coated nanoclusters were prepared as shown in figure 4.5 in materials and methods, but without the presence of tris-buffer. The polymerization was therefore done in 30 ml MQ-water. The polymerization was conducted with different parameters where mass of nanoclusters and mass of dopamine hydrochloride were varied in different ratios. The different batches produced are shown in Table 7.2.

Table 7.2: Table showing different batches of polydopamine coated nanoclusters.

Batch	Mass of IONCs in mg	Mass of DHCl in mg
DCIONCs 1:4	5	20
DCIONCs 1:2	5	10
DCIONCs 1:1	5	5
DCIONCs 2:1	10	5
DCIONCs 4:1	20	5

The reason for trying these different batches was to see if varying the ratio of IONCs to DHCl would give different particle properties. This could be everything from different zeta potential to different hydrodynamic size and stability within the particles that would prove and extensive added amount of either DHCl or IONCs could control the size and zeta potential.

7.2.2 DLS studies of sizes and zeta potentials of tris-less DCIONCs

All the different batches introduced were measured both in hydrodynamic size and their respective zeta potentials to see which particles would be the most suited for a potential PLGA coating. The hydrodynamic sizes, poydispersity and zeta potentials of the respective particles are shown in Table 7.3.

Table 7.3: Table showing assumed dopamine coated IONCs respectively measured in terms of hydrodynamic size, poydispersity index and zeta potential.

Batch	Hydrodynamic size (nm)	poydispersity index (%)	Zeta potential (mV)
1:4 DCIONCs	1110 ± 112	27 ± 7	-9 ± 1
1:2 DCIONCs	789 ± 70	15 ± 8	-7 ± 1
1:1 DCIONCs	849 ± 82	33 ± 4	-9 ± 1
1:2 DCIONCs	400 ± 50	26 ± 4	12 ± 1
1:4 DCIONCs	291 ± 2	26 ± 1	19 ± 1

Table 7.3 showed that there is a trend in the ratio of DHCl:IONCs when it comes to both size and zeta potential. To easier see the trend the sizes and zeta potential was made into curves. This is shown in Figures 7.1a and 7.1b

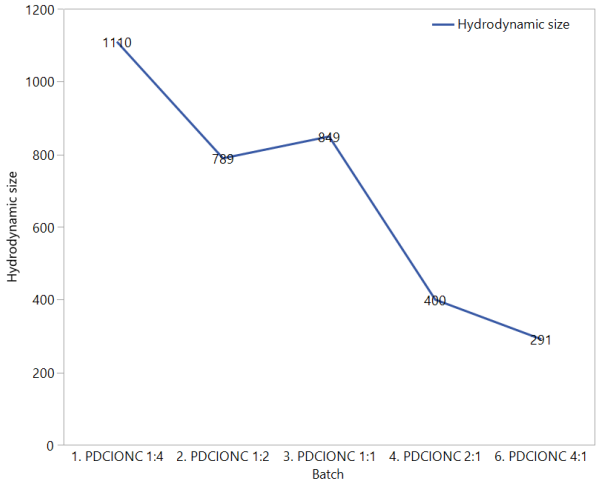

(a) Hydrodynamic size of DCIONCs with different mass ratios of DHCl:IONCs.

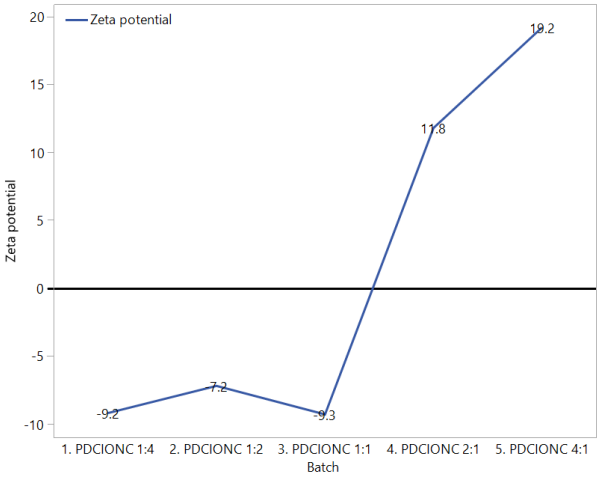

(b) Zeta potential of DCIONCs with different mass ratios of DHCl:IONCs.

Figure 7.1a and 7.1b shows the different sizes when introducing different ratios of DHCl:IONCs. It was observed that by inserting more DHCl the zeta potential seemed to decrease and the hydrodynamic size increased. This was also vice versa by inserting more IONCs, the Zeta potential increased while the hydrodynamic size increased. This could be due to less aggregation due to less alkaline environment by higher ratio of IONCs to DHCl, and hence smaller sizes. The increase in DHCl could make the particles aggregate, but the hydrodynamic size also increased as there was a formation of dopamine on top of the IONCs which was not polydopamine as it requires a stable pH of 8.5. It was therefore assumed to be a dopamine layer with unknown type of coating. The last interesting observation was that the 1:1 ratio seemed to not follow the trend, which could mean that the 1:1 is the optimal addition of DHCl to IONCs as the coating of the dopamine seemed to be more efficient and that most of the possible reaction sites on the surface was utilized.

7.2.3 Stability studies of assumed dopamine coating

A stability test was conducted to observe the possible impact of the difference in masses of DHCl and IONCs at different pH. The resulting zeta curves are shown below in figure 7.2

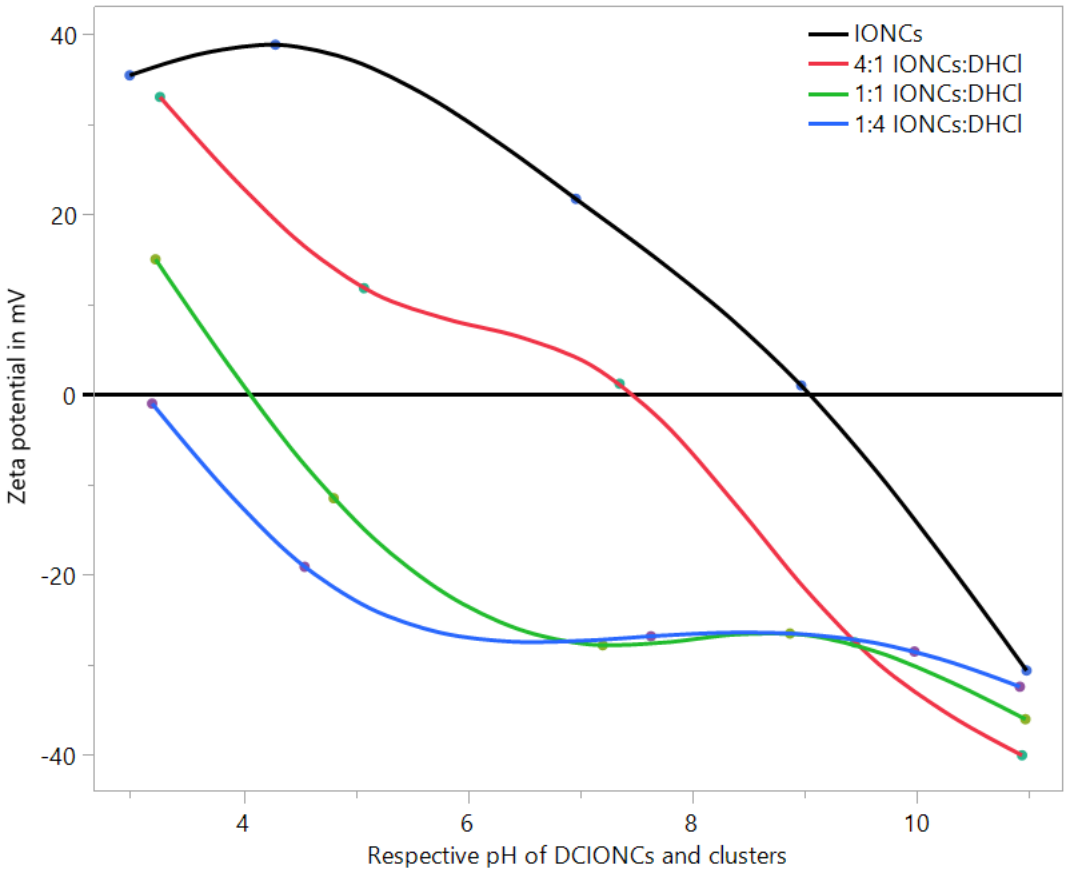

Figure 7.2: Zeta curve at different pH of different batches varying mass of DHCl and IONCs.

The data is also presented in Table 7.4 to show the respective pH and its belonging zeta potential for each of the batches.

Table 7.4: Table showing measured zeta potentials by different ratios of DHCl to IONCs batches in different pH.

pH and Zeta potential	IONCs	DCIONCs 4:1	DCIONCs 1:1	DCIONCs 1:4
pH	3.0	3.3	3.2	3.2
Zeta potential	35.4	33.0	15.0	-1.0
pH	4.3	5.1	4.8	4.6
Zeta potential	38.8	11.8	-11.5	-19.1
pH	7.0	7.4	7.2	7.6
Zeta potential	21.7	1.2	-27.8	-26.8
pH	9.0	9.5	8.9	10.0
Zeta potential	1.0	-27.5	-26.5	-28.5
pH	11.0	11.0	11.0	10.9
Zeta potential	-30.6	-40.0	-36.0	-32.4

Figure 7.2 and Table 7.4 shows that the ratio between affected the zeta potential of the different batches with different ratios of DHCl and IONCs and bare IONCs as a reference point. It seems that the particle coverage was higher for the higher ratio of DHCl:IONCs. The point of zero charge seemed to have moved when using the different ratios of DHCl:IONCs. This also correlated well with the actual polydopamine coating data compared to the IONCs in the results and discussion chapter where it was proven that the point of zero charge changed and moved towards lower pH after coating the particles.

7.3 PLA coating on PDCIONCs

PLA was attempted coated on top of proper PDCIONCs after satisfactory PDCIONCs were made and optimized. The method was not pursued as satisfactory particles in terms of size was able to be retracted from the PLGA polymerization of the PLGA@PDCIONCs. Some useful data was retrieved from the PLA polymerization and is shown below in the following section.

7.3.1 Stability study of poly-lactic acid (PLA)

A stability test in form of a zeta curve was analyzed for PLA and compared to PLGA and IONCs to see how the coating would behave at different pH. The resulting curve is shown below in Figure 7.3.

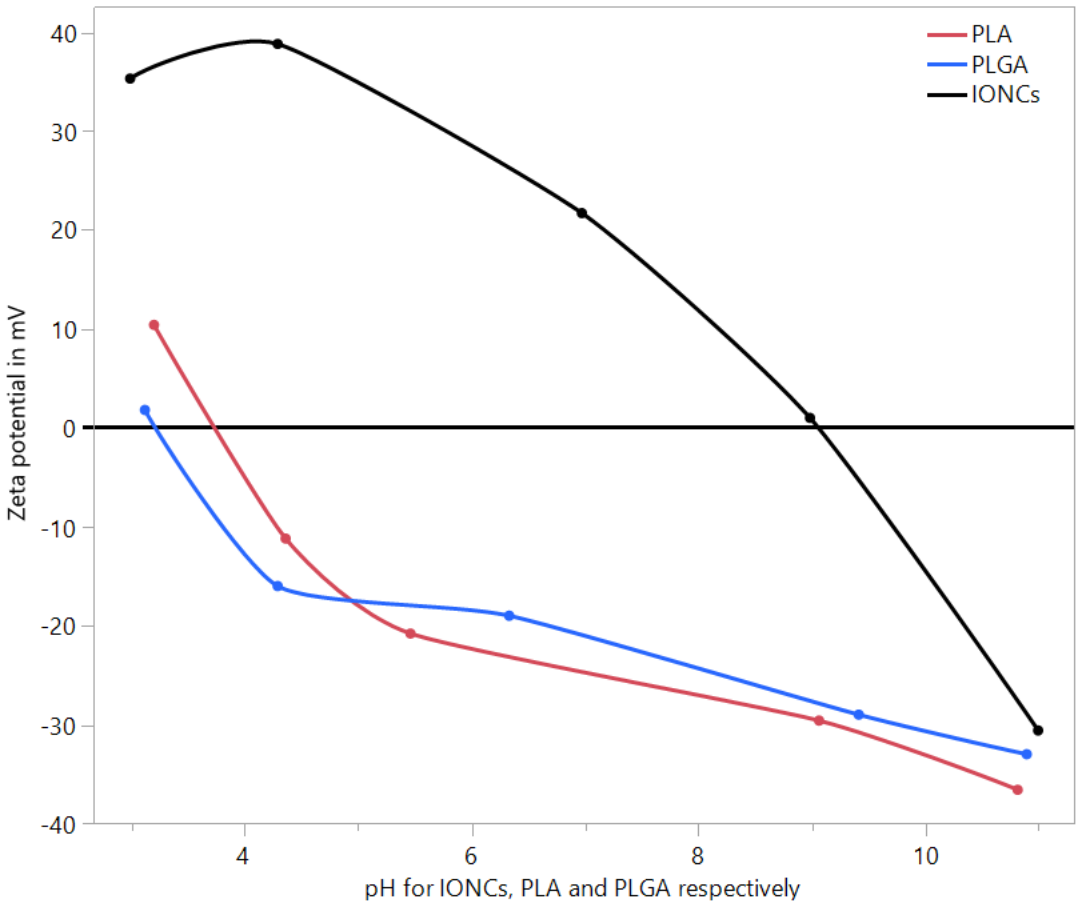

Figure 7.3: Zeta curve at different respective pH of IONCs, PLGA and PLA.

A table was also inserted to show the respective zeta potentials for each pH of each sample. The data is shown in Table 7.5.

Table 7.5: Table showing measured zeta potentials for respective pH of IONCs, PLGA and PLA.

pH and Zeta potential	IONCs	PLGA	PLA
pH	3.0	3.1	3.2
Zeta potential	35.4	1.8	10.4
pH	4.3	4.3	4.4
Zeta potential	38.8	-16.0	-11.2
pH	7.0	6.3	5.5
Zeta potential	21.7	-19.0	-20.8
pH	9.0	9.4	9.1
Zeta potential	1.0	-29.0	-29.6
pH	11.0	10.9	10.8
Zeta potential	-30.6	-33.0	-36.6

It was observed that the PLA showed slightly different trends in zeta potentials than that of the PLGA. It was also seen that both the PLGA and PLA differed a lot from the reference point of the IONCs. This indicates that both of these coatings seemed to occur when polymerizing the two polymers on top of the PDCIONCs.

7.3.2 S(T)EM images of PLA coated PDCIONCs

The particles coated with PLA was depicted in S(T)EM to see how the coating of the particles occurred and to see the differences in the coating between PLGA and PLA. The pictures are shown below in figure 7.4.

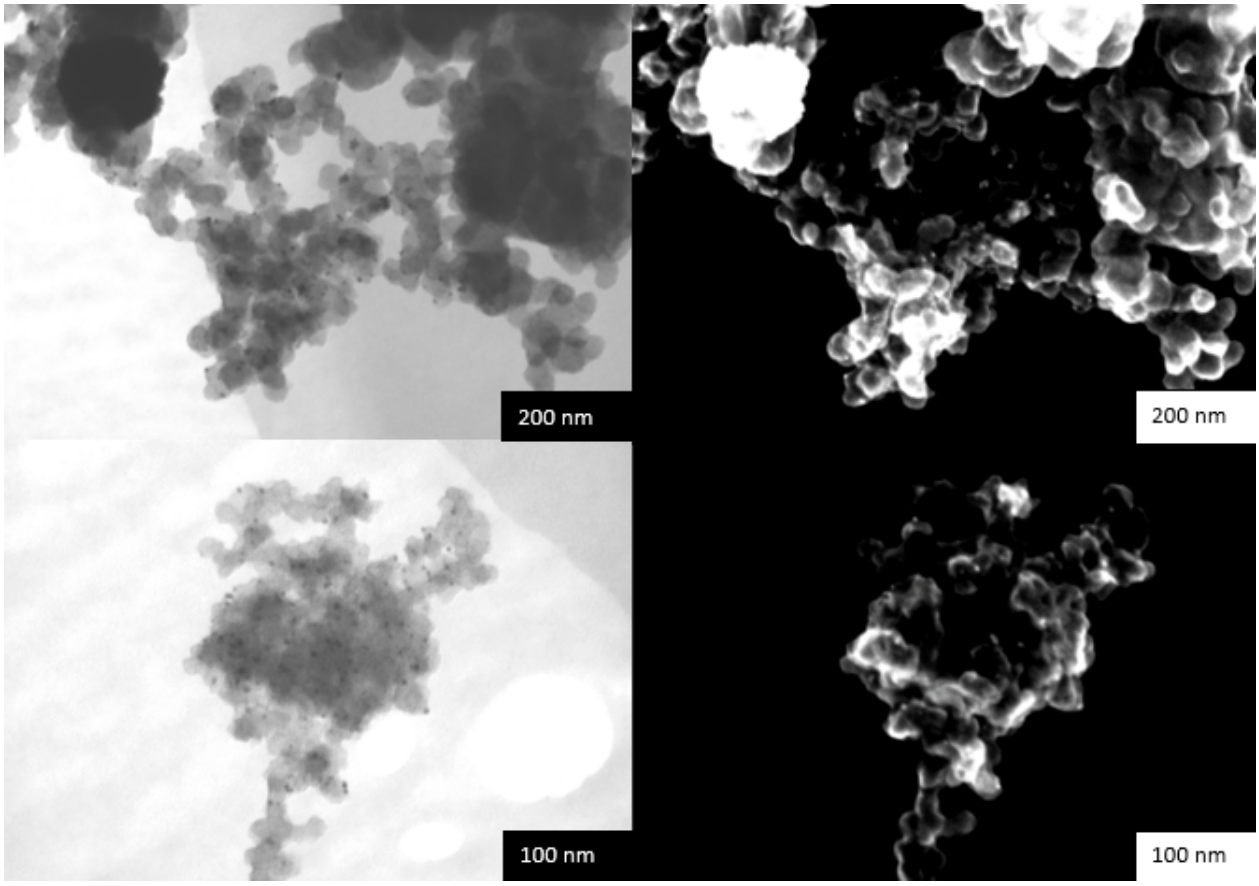

Figure 7.4: Images taken in S(T)EM of poly lactic acid coated PDCIONCs.

Figure 7.4 shows the PLA coated PDCIONCs imaged in S(T)EM. It was observed that the PDCIONCs seemed to accumulate either in the middle of the coating or around the edges. PLA is also a coating which could be viable in terms of drug delivery and hyperthermia. It seemed as if the sizes were also smaller for the PLA coating than for the PLGA. It was however still moved on with PLGA to try to optimize that process due to its faster degradation kinetics.

7.4 Some attempted PLGA optimization experiments through parameter variations

Both polydopamine coated IONCs and assumed dopamine coated IONCs were attempted polymerized with PLGA using different parameters. This was done to see if any differences were present in the PLGA coating to try to decrease the sizes of the particles post-coating. The different batches produced and their parameters are presented in Table 7.6.

Table 7.6: Table showing different batches PLGA coated PDCIONCs and DCIONCs

Batch	Mass of dry particles (mg)	Polymerization time
PLGA@DCIONCs tris	5	3 Hours
PLGA@DCIONCs tris-less	5	3 Hours
PLGA@PDCIONCs 15 mg	15	3 Hours
PLGA@PDCIONCs 20 min	6	20 minutes

Where the utilized monomer masses and initiator volume is shown in Table 7.7 which was used for all the polymerization batches.

Table 7.7: Chemical parameters for polymerizing PLGA on top of the different batches of (PDCIONCs).

Mass of L-glycolide in mg	Mass of RON-lactide in mg	Volume of stannous octoate in µl
450	900	6

7.4.1 Hydrodynamic sizes and zeta potentials from DLS

The particles were measured in terms of hydrodynamic size and zeta potential without including the poydispersity due to some unreal measurements in the instrument claiming PDI of up to 700%. The particle size and zeta potential are shown in Table 7.8.

Table 7.8: Table showing assumed dopamine coated IONCs respectively measured in terms of hydrodynamic size and zeta potential.

Batch	Hydrodynamic size (nm)	Zeta potential (mV)
PLGA@DCIONCs tris	6406 ± 842	-20 ± 1
PLGA@DCIONCs tris-less	2653 ± 1602	-21 ± 2
PLGA@PDCIONCs 15 mg	911 ± 127	-17 ± 1
PLGA@PDCIONCs 20 min	847 ± 64	-1 ± 1

7.4.2 S(T)EM images of different attempted PLGA coating techniques

The respective particle batches were imaged in S(T)EM to see if there was any significant difference between them. The images are shown in Figure 7.5.

Figure 7.5 shows the different batches attempted of polymerizing PLGA on top of DCIONCs and PDCIONCs. It could be observed that the particles had a different formation. It

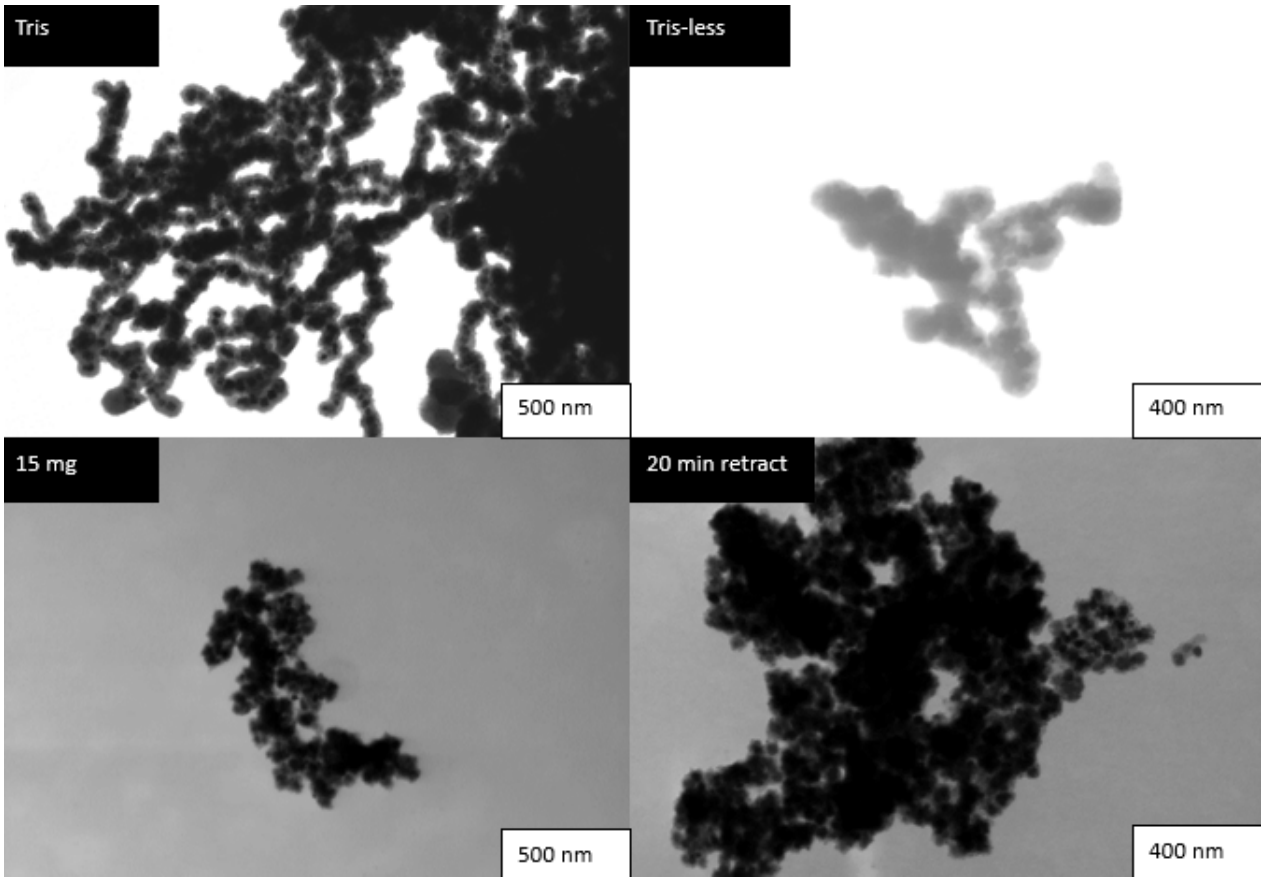

Figure 7.5: Images taken in S(T)EM of PLGA coated DCIONCs and PDCIONCs batches.

seems as if the DCIONCs that were coated started to form a sort of network of PLGA with the particles inside, while the PDCIONCS that were coated were surrounded without any directed structure. This could be due to the different formation of the particles as the tris-buffer in the DCIONCs were not properly made and hence polydopamine was probably not the surface modification. This means that the assumed dopamine surface functionalization seemed to create a network of the PLGA looking like a worm structure. The sizes were also different as the PLGA coated PDCIONCs had a proper threshold around the bigger particles, while most of the PLGA coated DCIONCs were usually a part of a very big aggregate. This means that whatever dopamine species is on top of the DCIONCs in the first two pictures can build into worms. It would need further work to find the exact formation mechanism for the PLGA and the surface coating from the DHCl to understand the mechanism properly.

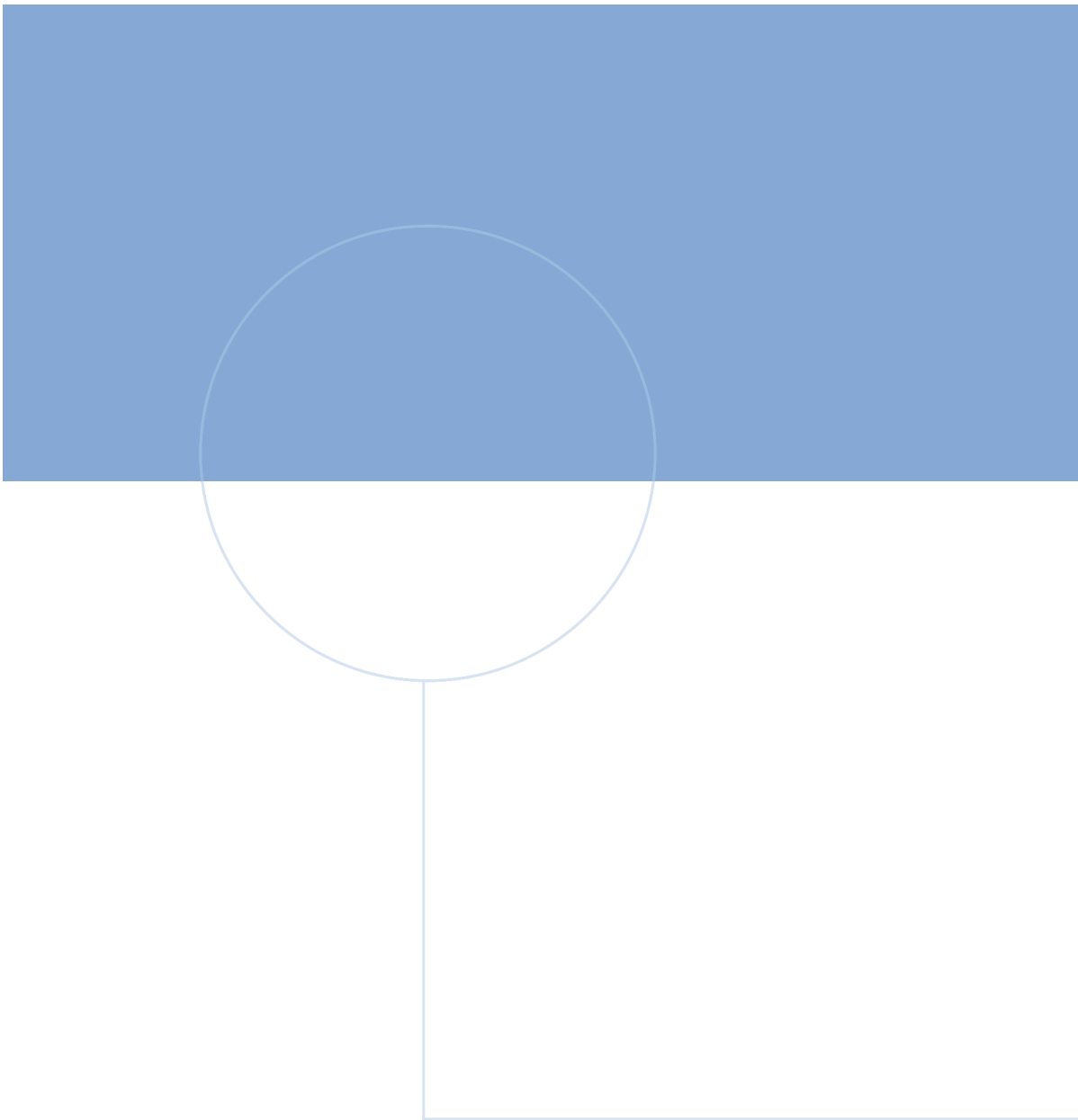

NTNU

Norwegian University of
Science and Technology